ALIGNMENT, VIBRATIONAL, AND STERIC EFFECTS IN UNIMOLECULAR AND BIMOLECULAR SYSTEMS:
TOWARDS AN UNDERSTANDING OF CHEMICAL REACTIONS IN QUANTUM-STATE DETAIL

by

Joanna R. Fair

B.A., Rice University, 1995

A thesis submitted to the Faculty of the
Graduate School
of the University of Colorado
in partial fulfillment of the requirements for the degree of
Doctor of Philosophy
Chemical Physics
2000

Fair, Joanna R. (Ph.D., Chemical Physics)

Alignment, Vibrational, and Steric Effects in Unimolecular and Bimolecular Systems:
Towards an Understanding of Chemical Reactions in Quantum-State Detail

Thesis directed by Adjoint Professor David J. Nesbitt

This thesis describes a series of experimental and theoretical projects designed to explore the dynamics of molecules and molecular collision systems in quantum-state resolved detail. First, the unimolecular dynamics of HOD are explored via photoacoustic spectroscopy of the $3\nu_{OH}$ and $4\nu_{OH}$ overtone bands. Analysis of the overtone series provides the vibrational dependence of rotational constants as well as evidence that the transition dipole moment vector tilts away from the OH bond with increasing excitation, inconsistent with simple local-mode, bond-dipole model predictions but in excellent agreement with full 3D quantum variational calculations. Second, the generation of radical clusters from the photolysis of Ar-H_2S and Ar_2-H_2S is investigated via quasiclassical trajectory calculations, providing a comparison with earlier experiments in supersonic jet expansions. The calculations confirm the overall efficiency of radical cluster formation as well as significant intracluster excitation; clusters with excess rotational energy above the dissociation limit are found to be trapped by an angular momentum barrier that prevents dissociation. Third, quasiclassical trajectory calculations on experimentally determined intermolecular potentials for He-O_2, He-CO, and He-CO_2 simulate the collisional formation of rotationally aligned molecular distributions in a supersonic expansion. These calculations verify a preference for **j** perpendicular to the expansion axis, with

asymptotic alignment increasing monotonically with j. This alignment reflects comparable contributions from elastic and inelastic collisions; in addition, molecules with **j** aligned parallel to the expansion axis have faster average velocities than molecules with **j** perpendicular. Fourth, the role of intramolecular vibrational redistribution on the timescale of a reactive encounter is explored with a reduced-dimensionality model of $Cl + H_2O \rightarrow HCl + OH$, with isotopic variations. The vibrational eigenstates of H_2O/HOD/D_2O are calculated versus Cl-water separation, generating adiabatic potential energy curves and nonadiabatic coupling terms for time-dependent dynamics calculations. For the vibrational eigenstates, the near-resonance of the H_2O symmetric and asymmetric stretches rotates the symmetric/asymmetric stretch towards/away from the Cl atom as it approaches in the vibrationally adiabatic limit. For Cl+HOD, vibrational excitation in the OH mode enhances HCl + OD reaction probability by more than an order of magnitude more than excitation in OD.

To my parents, Frank and Janet, and my brother, Ken,

and

in memory of my grandparents

ACKNOWLEDGEMENTS

While heading down the winding road leading from Huntsville, TX, to a doctorate in chemical physics, I have had the fortune of crossing paths with many great teachers over the years. Before coming to graduate school, I was inspired by Pat Nash, Pat Williams, Robert Jones, and especially John Hutchinson, my mentor and friend. Since my arrival in Boulder, my advisor David Nesbitt has challenged me and encouraged my development as a scientist—not always a painless process, but one that I now truly value.

During my graduate career, I was privileged to work and commiserate with the members of the Nesbitt group, including my labmates Ondrej Votava, Stuart Mackenzie, and Tanya Myers, as well as Bill Chapman, Brad Blackmon, Scott Davis, David Anderson, Dairene Uy, Michal Farnik, Miles Weida, Ken Kuno, David Fromm, Sergey Nizkorodov, and Hendrick Hamann. I am also thankful to all the folks in the JILA Instrument Shop, Electronics Shop, Computing, SRO, Reception, and Supply Office for skillful and friendly support, especially Hans Green for help with the Blackbody Radiation Pump and Chela Kunasz for rescuing me from numerous computer glitches.

Finally, I would like to thank my officemates, who kept me sane and accompanied me to Dairy Queen during thesis-writing stress: Hilary Eaton, Sebastian Heinz, Elizabeth Mirowski, Amy Van Engen, and especially my honorary officemate Anthony Lupinetti, without whom this thesis would not have been possible.

CONTENTS

CHAPTER

TABLES

CHAPTER 2

CHAPTER 3

CHAPTER 4

CHAPTER 5

FIGURES

CHAPTER 2

CHAPTER 3

CHAPTER 4

CHAPTER 5

CHAPTER 1

INTRODUCTION

A physical chemist's ultimate goal might be to understand and manipulate each aspect of a reactive encounter, i.e., the initial rovibrational states of the reactants, relative orientations, direction of approach, and collision velocities, guiding the breaking and formation of bonds at a state-to-state level of detail. While such detailed understanding and control of chemical reaction is not currently feasible experimentally, a number of strides have nevertheless been made in this direction. Two well-developed areas of this study included vibrationally mediated chemistry[1] and stereodynamical control of chemical reactions,[2] with progress in these areas more fully detailed in subsequent chapters.

The crossroads between these two areas can be beautifully illustrated by a series of experiments by the Zare group on the reaction of CH_4 and CD_3H with Cl atoms.[3-5] In these studies, CH_4, coexpanded with Cl_2, was vibrationally excited to $v_3=1$ (asymmetric stretch); the Cl_2 was then photolyzed at 355 nm to produce collisions between Cl and CH_4 at a collision energy of 1280 cm^{-1}. The state-to-state differential cross sections for the reaction of Cl with $CH_4(v_3=1)$ were measured and compared with results from ground-state CH_4 and $CD_3H(v_1=1$, CH stretch). This series of experiments determined sufficient detail about the nature of the reactive encounter to propose a mechanism for the H-atom abstraction, namely, that small, medium, and large impact parameters produce backwards, forwards, and sideways scattering of the HCl, respectively. CH_4 vibrational excitation was shown to increase the cone angle of acceptance for reaction. This mechanism was then confirmed by studies of steric effects in the reaction of Cl with spatially aligned CD_3H.

This example illustrates three major steps in understanding chemical reaction in quantum-state detail: preparation and interrogation of a specific quantum state of the reactant molecule; control and understanding of the interaction between the reactants; and collection and analysis of the products of the reaction. In a series of four projects, we follow this path toward quantum-state understanding of chemical reactions, beginning with the preparation of a molecule in a single quantum state and concluding with a study of how such a prepared quantum state influences chemical reaction. Over the course of this thesis, the interchange between theory and experiment is emphasized, and in particular, the opportunities for theory to provide insight initially unavailable from experiment alone are stressed.

The first project, described in Chapter 2, involves the experimental investigation of the unimolecular dynamics of HOD via OH vibrational overtone excitation.[6] From an experimental point of view, vibrational excitation of a particular bond, which can be used to prepare this molecule in a single rovibrational quantum state, provides a path towards selective reaction. Since the probability of absorbing a photon varies as the cosine squared of the angle between the transition dipole moment of the molecule and the polarization vector of the light, such photoexcitation can prepare an aligned distribution of reactive molecules for stereochemical studies. Importantly, this study provides evidence that for OH overtone transitions, the transition dipole moment vector tilts *away* from the OH bond with increasing v_{OH} excitation, qualitatively inconsistent with simple local-mode, bond-dipole model predictions of the vibrational transition moments. This observation thus provides the opportunity for exchange between theory and experiment: the relative importance of electrical (i.e., in the dipole surface) versus mechanical (i.e., in the potential surface) anharmonicity effects are investigated by 2D and 3D quantum variational calculations.

The second project, described in Chapter 3, extends the study of unimolecular dynamics to unimolecular *collisions* via photodissociation of a reactive precursor within a cluster. Specifically, the production of radical clusters from the photolysis of Ar-H_2S and Ar_2-H_2S is investigated via quasiclassical trajectory calculations, providing a comparison with earlier experiments on these clusters in supersonic jet expansions.[7,8] If the cluster is considered as a single unit, this process is a means of preparing a wide range of cluster quantum states for subsequent dynamical studies. Alternatively, photodissociation within clusters of potentially *reactive* species provides the possibility of controlling the geometry of the reactive encounter. Thus, this study provides the next step on the path towards understanding reactive bimolecular collisions. Once again, this work allows for interchange between experiment and theory through investigating the details of the experimentally observed photodissociation process. Not only do the photolysis calculations confirm the overall efficiency of radical cluster formation, but they also provide evidence for *bound* clusters with excess rotational energy above the dissociation limit, trapped by an angular momentum barrier that prevents dissociation. These calculations thus contribute additional understanding of the cluster dynamics unavailable from the experiment.

The third project, described in Chapter 4, extends the study of collision dynamics to bimolecular, nonreactive scattering with a computational study of collisional alignment in supersonic expansions. Experimentally, collisions between a light “diluent” gas and heavier “seed” rotor molecules in a seeded supersonic expansion have been shown to produce a distribution of rotor molecules with a preference for **j** perpendicular to the expansion axis. This phenomenon has been demonstrated for a wide variety of rotor molecules and collision partners, aligning a more general class of molecules than can be accomplished with AC and DC field methods. Despite the promising possibility that collisional alignment could be used to prepare reagents for studies of steric effects in chemical reactions, it has yet to see practical application in this way. In part, this results from a current lack of agreement among experimental and theoretical studies about the details of this alignment process. The goal of this chapter thus is to elucidate the mechanism of alignment via classical trajectory calculations on experimentally determined intermolecular potentials. We focus on particular areas of controversy such as the velocity- and j-dependence of alignment, as well as on determining the relative contributions from both elastic (m_j-changing) and inelastic (j-changing) collisions.

The final project, described in Chapter 5, concludes the study of collision dynamics with an investigation of vibrational effects in chemical reaction, focusing on the reaction of Cl with water and its isotopes. While vibrationally mediated chemistry has been investigated in great detail both experimentally and theoretically, few studies have directly probed the effect of the reactive atom on the vibrational state of the molecule. Consequently, we explore the role of the reactive atom in intramolecular vibrational redistribution on the timescale of a reactive encounter via time-dependent quantum reactive scattering. In these studies, the vibrational eigenstates of a reduced-dimensionality model of $Cl + H_2O \rightarrow HCl + OH$ (and isotopic variations) are calculated as a function of Cl-H_2O center of mass separation, generating adiabatic potential energy curves and the nonadiabatic coupling matrix elements between these curves for use in time-dependent dynamics simulations. These calculations allow us to look in detail at the nature of the vibrational eigenfunctions for H_2O/D_2O/HOD with chlorine-atom approach. In this study, we have thus come full circle from our initial work on the overtone spectroscopy of HOD to probe how an initially prepared quantum state is influenced and changed by the reactive encounter.

References for Chapter 1

1. F. F. Crim, *J. Phys. Chem.* **100,** 12725 (1996).

2. A. J. Orr-Ewing, *J. Chem. Soc. Faraday Trans.* **92,** 881 (1996).

3. W. R. Simpson, A. J. Orr-Ewing, and R. N. Zare, *Chem. Phys. Lett.* **212,** 163 (1993).

4. W. R. Simpson, T. P. Rakitzis, S. A. Kandel, A. J. Orr-Ewing, and R. N. Zare, *J. Chem. Phys.* **103,** 7313 (1995).

5. W. R. Simpson, A. J. Orr-Ewing, S. A. Kandel, T. P. Rakitzis, and R. N. Zare, *J. Chem. Phys.* **103,** 7299 (1995).

6. J. R. Fair, O. Votava, and D. J. Nesbitt, *J. Chem. Phys.* **108,** 72 (1998).

7. S. R. Mackenzie, O. Votava, J. R. Fair, and D. J. Nesbitt, *J. Chem. Phys.* **105,** 11360 (1996).

8. S. R. Mackenzie, O. Votava, J. R. Fair, and D. J. Nesbitt, *J. Chem. Phys.* **110,** 5149 (1999).

CHAPTER 2

OH STRETCH OVERTONE SPECTROSCOPY AND TRANSITION DIPOLE ALIGNMENT OF HOD

2.1 Introduction

In recent years, a wealth of experimental studies have been aimed at elucidating photofragmentation and chemical reaction dynamics of vibrationally quantum state selected molecules. As a result of its small size, large vibrational spacings, and relatively convenient access to high overtone absorption bands (i.e., $v_{OH} = 3$, 4, and 5) with near-IR and visible dye lasers, H_2O and its isotopomers have been a focus of significant attention. Of particular relevance has been the highly localized versus delocalized nature of the OH stretch vibrational levels in HOD, which has made it an especially attractive candidate for experimental and theoretical studies of vibrationally mode specific reaction dynamics. Indeed, as beautifully demonstrated in the Crim,[1-4] Rosenwaks,[5-7] and Zare[8] groups, vibrational excitation of HOD has been used to control which bond is broken by subsequent UV photolysis[1,5-8] as well as to manipulate bond specific reaction probabilities.[2-4]

Despite the elegant dynamical studies performed on vibrationally excited HOD, until recently surprisingly little was known about its high-resolution overtone spectroscopy. There have been far-IR and microwave studies of HOD in the ground vibrational state[9] as well as near-IR studies of HOD in the fundamental region that have analyzed single-quantum (i.e., ν_{OH}, ν_{OD}) excitation from the ground to first excited OH or OD stretching states.[10] However, there have been no rotationally resolved studies on HOD excited beyond $v_{OD} = 2$, and, until fairly recently, no rotationally analyzed overtone studies whatsoever in the pure OH stretch manifold. The difficulty of such a rotational analysis is easily appreciated, due to the large rotational constants, anomalous centrifugal effects, and widely spaced, irregular level patterns of a highly asymmetric top. These issues are further exacerbated in light hydrides such as HOD by the anomalously large changes in rotational constants with OH vibrational excitation.

This absence of high overtone data on HOD has recently been changed by efforts from several directions. The first is an overtone study by Bykov *et al.* on the $3\nu_{OH}$ and $5\nu_{OH}$ bands of HOD obtained via intracavity laser spectrometer and optoacoustic dye laser spectrometer, respectively.[11] This study determined vibrational origins and rotational constants for both bands, with a frequency precision of 0.03 cm^{-1} for $3\nu_{OH}$. However, as a prerequisite to vibrationally mediated photolysis studies of HOD[12] and HOD-containing clusters[13] under supersonic jet conditions, we have more recently performed a high-resolution overtone study in our laboratory on the $3\nu_{OH}$ band of HOD. This study, obtained by photoacoustic detection in a room-temperature cell with an injection-seeded optical parametric oscillator, was performed to determine rovibrational frequencies for $3\nu_{OH}$ transitions out of the ground (i.e., $J_{KaKc} = 0_{00}$) rotational state with greater precision.

In addition to this work, high-resolution OH stretch overtone data on HOD via H + HOD "action" spectra and photoacoustic spectra for $4\nu_{OH}$ has been obtained by Crim and co-workers, for which a rotational analysis has not previously been attempted. The successful completion of our work in the $3\nu_{OH}$ region stimulated us to rotationally analyze this unassigned $4\nu_{OH}$ data. In the meantime, vibrationally mediated photolysis studies on HOD in the $4\nu_{OH}$ region have been reported by Brouard and Langford[14] in which the primary aim was toward characterizing the detailed OD photofragment distributions from photolysis of quantum-state-selected HOD. Nevertheless, the work clearly necessitated sufficient understanding of the $4\nu_{OH}$ rotational structure to label the HOD quantum states, which allowed estimates of the band origin and rotational constants to be obtained. However, as some of these results differ substantially from the present analysis, a more detailed spectroscopic investigation of the HOD $4\nu_{OH}$ overtone band is still warranted. Thus, the detailed analysis of both our $3\nu_{OH}$ spectra and the $4\nu_{OH}$ data of the Crim group forms the initial thrust of this chapter.

The second area addressed in this chapter is the *alignment* of the vibrational overtone transition dipole moment vector with respect to the HOD molecular framework. This proves to be a surprisingly subtle issue, one whose resolution is quite sensitive to the topology of the potential energy and dipole moment surfaces. For example, if we think in terms of a simple "bond-dipole" model for a purely localized vibration, the transition dipole moment vector would be aligned perfectly along the axis of the vibrating bond. Conversely, if electrical anharmonicity effects lead to a redistributed charge distribution with nuclear displacement, the transition dipole moment vector can be rotated significantly away from the bond axis by an amount which depends on the degree of overtone excitation. Clever experimental techniques for study of such vibrational-transition-moment anisotropies have been developed for large organic molecules aligned in stretched films.[15] However, this information has proven challenging to obtain for much smaller species such as water, which rotate nearly freely and therefore cannot be effectively aligned by the film. A more traditional alternative is via rotationally resolved spectroscopy of these species in the gas phase. Specifically, this information can be extracted by measuring the fractional a-, b-, and c-type character of each vibrational band, which from a rigid asymmetric top model determines where the transition moment lies relative to the principal inertial axes of the molecule. Consequently, with rotationally resolved data for the OH stretch (ν_{OH}, $3\nu_{OH}$, and $4\nu_{OH}$) series in HOD, one can not only determine the direction of this transition moment vector but also probe how that vector *changes* as a function of OH vibrational excitation. This is of particular interest for such fundamental species as water, where high quality *ab initio* dipole moment and potential energy surfaces exist which can be used with exact 3D quantum variational calculations for rigorous comparison with experiment.

The remainder of this chapter is organized as follows. Section 2.2 briefly reviews the experimental apparatus for $3\nu_{OH}$ and $4\nu_{OH}$ photoacoustic spectroscopy of HOD. In Sect. 2.3, the results from the $3\nu_{OH}$ analysis are used to facilitate rotational assignment of the $4\nu_{OH}$ overtone spectrum of HOD of Crim and co-workers, and relative a- and b-type band intensities are determined for the ν_{OH}, $3\nu_{OH}$ and $4\nu_{OH}$ overtone series. These intensity ratios probe the vibrational dependence of the transition dipole moment vector and are used in Sect. 2.4 to test theoretical models of the H_2O dipole moment surface. The conclusions of this chapter are summarized in Sect. 2.5.

2.2 Experimental

The source of light for the $3\nu_{OH}$ photoacoustic signals is a single-mode optical parametric oscillator (OPO) generating narrow-bandwidth infrared radiation, which is described elsewhere.[16] Briefly, the tripled output at 355 nm of an injection-seeded, pulsed Nd:YAG laser is used to pump two β-barium borate (BBO) crystals in a four-mirror ring resonator to generate "signal" and "idler" beams via parametric amplification. The ring resonator configuration is exploited by injection seeding the OPO cavity with a tunable, single-mode cw dye laser prior to the UV pump, which therefore generates near Fourier transform limited, tunable output (3.5 ns, $\Delta\nu = 160$ MHz) for both signal and idler pulses. Day-to-day reproducibility and frequency stability at the MHz level[17] for the single-mode 355 nm pump source is maintained by servo loop locking the injection seed for the Nd:YAG laser fundamental to a stabilized optical transfer cavity,[18] which is locked to a polarization-stabilized HeNe laser.[19] Based on the stability of the optical transfer cavity, frequency differences can be routinely measured to a precision of better than a few ten-thousandths of a cm^{-1} over several hundred cm^{-1}, which is far narrower than the Doppler broadened line width for HOD at room temperature ($\Delta\nu_{FWHM} \approx 0.030$ cm^{-1}). The spectral precision of these measurements is quantitatively verified by comparison with well-known HITRAN $|03^{-}>$ H_2O overtone transitions[20,21] simultaneously observed in the photoacoustic cells.

For the $4\nu_{OH}$ band work, a similar photoacoustic cell arrangement is used in the Crim group but with a conventional pulsed dye laser operating in the 13,750 cm^{-1} region. The bandwidth of the dye laser is 0.05 cm^{-1}, which is now in excess of room temperature Doppler widths for HOD. This multimode dye laser has the considerable advantage over the single mode OPO light source of being able to scan relatively quickly over the entire photoacoustic spectrum. However, the corresponding disadvantage is a much lower overall accuracy of frequency measurement. Consequently, the dye laser wavelength scan has been calibrated to 56 $|04^{-} >$ H_2O overtone transitions embedded in the photoacoustic spectrum, based on the H_2O transition frequencies reported in the HITRAN database.[20,21] It is worth noting that this calibration plot is quite linear but shifted by nearly 10 cm^{-1} from values obtained simply from wavelength readings on the tuning mechanism. Left uncorrected, this would lead to errors of comparable magnitude in the least-squares fit band origins, with smaller but also significant effects on the reported rotational constants. This suggests the dye laser calibration to be the predominant reason for the significant discrepancies between the recently reported spectroscopic values of Brouard and Langford[14] and our current results from the calibrated $4\nu_{OH}$ photoacoustic data. From the scatter in this calibration, the frequency precision of the dye laser is estimated to be $2\sigma = 0.07$ cm^{-1}, dominated by residual nonlinearity in the dye laser wavelength scan.

These light sources (either the pulsed OPO or dye laser output) are then sequentially passed through two photoacoustic cells, the first containing 10 Torr of pure H_2O, the second containing 10 Torr of a mixture of H_2O/HOD/D_2O in a near-stoichiometric 1:2:1 ratio. Photoacoustic signals from each cell are simultaneously digitized via sample and hold circuits and recorded as a function of frequency. Transitions for both pure HOD $3\nu_{OH}$ and $4\nu_{OH}$ are readily identified by comparison between spectra recorded for the two cells. Absolute frequencies are obtained by calibration against H_2O second and third overtone transitions in this spectral region tabulated in the HITRAN database.[20,21]

2.3 Results

2.3.1 HOD: $3\nu_{OH}$

The transition frequencies, rotational assignment and asymmetric top spectral fits of the $3\nu_{OH}$ band of HOD are obtained in the following way. In order to minimize the effects of centrifugal distortion, it is useful to restrict the photoacoustic scans to regions corresponding to low J_{KaKc}. The initial search is guided by theoretical calculations by Tennyson and co-workers[22] on the H_2O potential surface of Polyansky *et al.*,[23] which predict a $3\nu_{OH}$ band origin at 10632.5 cm^{-1}. Due to the light H/D masses, one must contend with an anomalously large vibrational dependence of the A, B, and C rotational constants, which can be estimated for $v_{OH} = 3$ by linear extrapolation from the ground and $v_{OH} = 1$ rotational constants. A simulated asymmetric top spectrum for the $3\nu_{OH}$ band generated from these predictions enables the search to be constrained to maxima in the P and R branch regions at low J_{KaKc}, which proves sufficiently reliable to make initial rotational assignments of the overtone spectra. These assignments are then rigorously confirmed by ground-state combination differences with the microwave data of De Lucia *et al*.,[9] which also agree to within 100 MHz, i.e., <10% of the Doppler broadened line widths ($\Delta\nu_{\mathrm{Doppler}} \approx 1$ GHz) observed in a room temperature photoacoustic cell. A summary of the low J_{KaKc} transitions (J<5) observed and assigned in the P-branch (10631-10656 cm^{-1}) and R-branch (10680-10690 cm^{-1}) regions are reported in Table 2.1.

The $3\nu_{OH}$ spectral data for HOD have been analyzed by least squares fitting to a Watson[24] asymmetric top Hamiltonian (A-type reduction, I^r representation), including up to quartic centrifugal distortion terms; the results are summarized in Table 2.2. The resulting simulation of the HOD spectrum in this region, shown in Fig. 2.1c, agrees essentially quantitatively in position and intensity with the observed transitions in Fig. 2.1.a. As unambiguous confirmation of this rotational assignment, we have performed vibrationally mediated photodissociation studies of HOD in supersonic jets, where by virtue of supersonic cooling the spectrum collapses to a *single* $3\nu_{OH}$ $1_{01} \leftarrow 0_{00}$ transition out of the 0_{00} ground rotational state.[12] Of special note, Tennyson's prediction[22] of the HOD band origin is within 0.8 cm^{-1} of the experimental result, which provides strong quantitative confirmation of the Polansky potential surface[23] for H_2O. Furthermore, this $3\nu_{OH}$ data set allows quite reliable extrapolation to the $4\nu_{OH}$ overtone manifold, permitting detailed rotational assignment of the third overtone OH stretch HOD data of Crim and coworkers. To facilitate comparison with fits of other OH stretch transitions of HOD, these fits have

Table 2.1. Observed $3\nu_{OH}$ transitions out of low-J_{KaKc} states in HOD via high-resolution photoacoustic spectroscopy.

J'	K_a'	K_c'	J''	K_a''	K_c''	ν (cm^{-1})
1	1	0	1	1	1	10631.314(0)[a]
2	1	1	2	1	2	10636.353(3)
3	1	2	3	1	3	10643.752(-1)
1	1	0	1	0	1	10645.613(-1)
1	0	1	0	0	0	10646.917(0)
2	0	2	1	1	1	10647.092(1)
2	1	1	2	0	2	10648.302(-1)
3	1	2	3	0	3	10652.813(-1)
4	1	3	4	1	4	10653.236(0)
2	1	2	1	1	1	10655.996(1)
3	3	0	3	2	1	10680.378 (0)
3	1	3	2	0	2	10680.689(-11)
5	3	3	4	3	2	10680.689(6)
4	1	4	3	1	3	10680.763(-1)
5	3	3	5	2	4	10682.533(-1)
4	2	2	3	2	1	10683.851(1)
4	0	4	3	0	3	10686.072(0)
4	1	4	3	0	3	10689.822(-1)
5	0	5	4	1	4	10689.908(0)

[a] Numbers in parentheses are residual differences from predicted transition frequencies from the fit.

[b] Blended peak; weight = 0.1 in fit.

Table 2.2. HOD $\nu_{OH}=3$ spectroscopic constants from centrifugally distorted asymmetric top least-squares fit (in cm^{-1}).

A	20.3873(24)[a]
B	9.0739(7)
C	6.1667(7)
Δ_J	$4.81(13)\times10^{-4}$
Δ_{JK}	0[b]
Δ_K	$1024(24)\times10^{-2}$
δ_J	$1.69(15)\times10^{-4}$
δ_K	$2.95(22)\times10^{-3}$
ν_0	10631.679(2)
σ_{fit}	0.0017

[a] Uncertainties represent two standard deviations from least-squares fit.
[b] Zero within uncertainty and thus constrained to be zero.

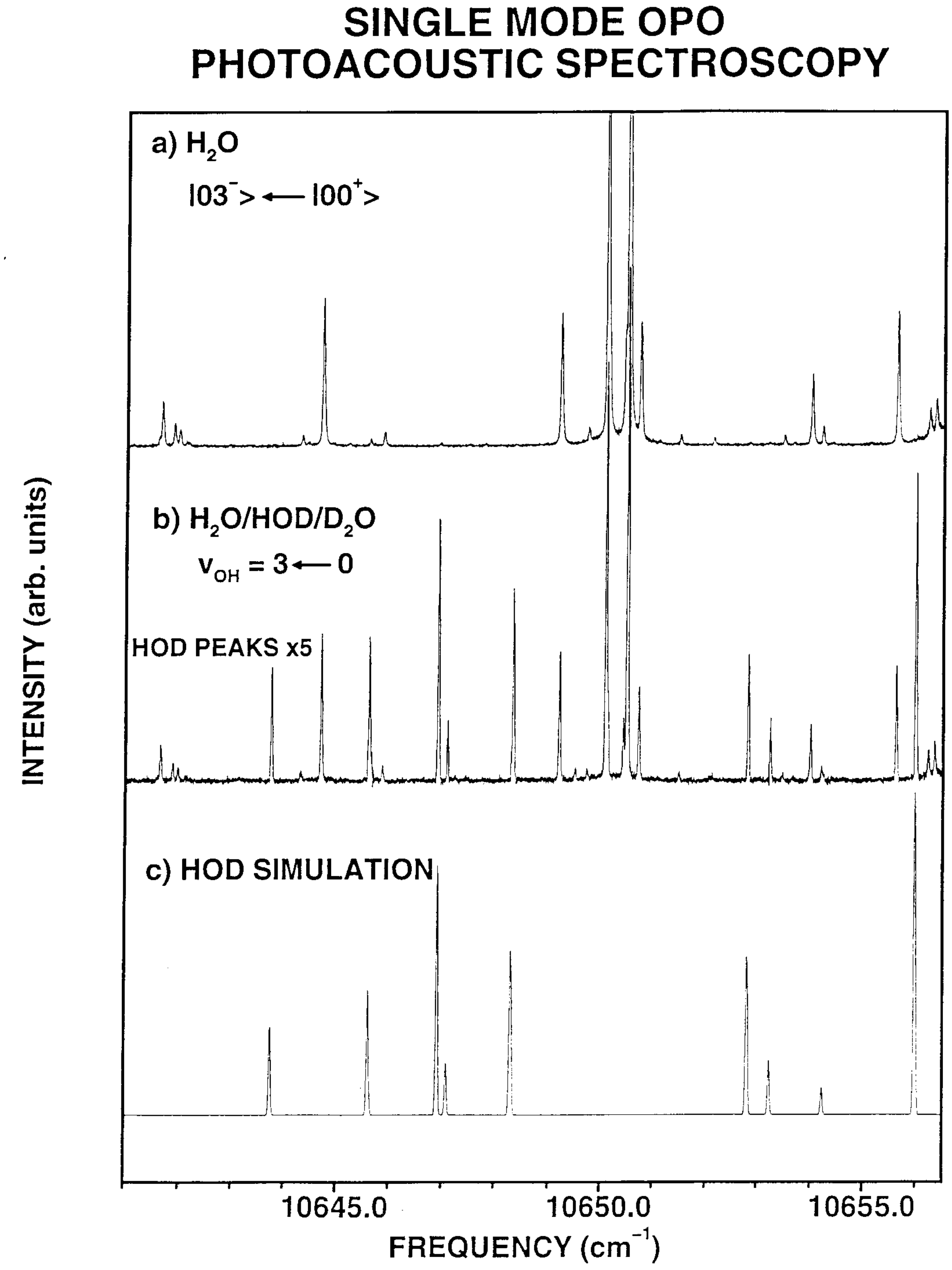

Figure 2.1. Sample high-resolution photoacoustic scan over the $3\nu_{OH}$ overtone region in (a) H_2O and (b) H_2O, HOD and D_2O (≈1:2:1) photoacoustic cells. Transitions present in only the mixed isotope cell are due exclusively to HOD (and enhanced five-fold for visual clarity). (c) The results of a least squares fit to an asymmetric top Watson Hamiltonian are shown for HOD $3\nu_{OH}$ in the lowest panel.

been repeated with parameters limited to the lowest order A, B, and C constants and a vibrational origin. The results of such a rigid asymmetric top fit of HOD for $3\nu_{OH}$ are listed in Table 2.3.

For a rigid asymmetric top, the ratio of a-type, b-type, and c-type band intensities is determined by the square modulus of the transition dipole moment component along the corresponding inertial axes of the molecule. For $3\nu_{OH}$-excited HOD, only a-type and b-type transitions are observed, consistent with a transition moment in the plane of the molecule. To specify the intramolecular alignment of the in-plane transition moment, integrated a-type and b-type line strengths are measured and compared with predicted line intensities from the Watson Hamiltonian. Averaged over all line strengths measured, the $3\nu_{OH}$ second overtone band of HOD corresponds to an a-type/b-type ratio of 2.7(10):1, where the uncertainty represents two standard deviations.

Table 2.3. HOD spectroscopic constants[a] (in cm^{-1} unless otherwise noted) from rigid rotor fits to A_v, B_v, C_v.

	v_{OH}				
	0[b]	1[c]	3 (this work)	4 (this work)	4 (previous)[d]
A_v	23.256(95)	22.292(31)	20.235(13)	19.357(6)	19.465
B_v	9.084(36)	9.072(12)	9.041(9)	9.029(6)	9.042
C_v	6.398(29)	6.318(7)	6.163(5)	6.089(5)	6.092
ν_0 ($v \leftarrow 0$)		3707.32(9)	10631.75(6)	13853.50(4)	13844.8
			(10632.5)[e]	(13853.4)[e]	(13853.4)[e]
Δ_v (amu·Å^2)	0.054(15)	0.054(4)	0.037(4)	0.030(3)	
σ_{fit}	0.10	0.17	0.067	0.085	0.2

[a] Uncertainties represent two standard deviations obtained from the least-squares fit.
[b] Fit to $J \leq 5$ data of De Lucia *et al*.[9]
[c] Fit to $J \leq 5$ data of Benedict *et al.*[10]
[d] From Brouard and Langford.[14]
[e] Predictions by Tennyson and coworkers based on the Polyansky *et al*. potential surface.[23]

2.3.2 HOD: 4ν_{OH}

Scans over the 4ν_{OH} band have been obtained by tandem photoacoustic spectroscopy in cells containing i) H_2O and ii) isotopically mixed H_2O/HOD/D_2O. Since pure D_2O absorptions in this region correspond to even higher ($\Delta\nu_{OD} = 5$) overtone excitation[10] and can be neglected, comparison of the two spectra readily permits contributions from H_2O and HOD to be identified separately. Sample data for H_2O and HOD overtone absorptions in the 4ν_{OH} region from the H_2O and the H_2O/HOD/D_2O photoacoustic cells are shown in Fig. 2.2a, demonstrating relatively clean rotational resolution of the H_2O and HOD overtone signals. The region scanned is between 13760 cm^{-1} and 13858 cm^{-1}, which from our rotational assignment covers most of the P branch and the Q branch up to and including the H_2O vibrational origin.

The analysis of the 4ν_{OH} spectra for HOD follows an identical strategy to the 3ν_{OH} band. However, with v_{OH} = 0, 1 and 3 manifolds rotationally characterized, considerably less uncertainty exists in the extrapolation procedure. Specifically, linear extrapolations of the principal rotational constants for v_{OH} = 0, 1, and 3 produce excellent predictions for A_4, B_4, and C_4. Similarly, a Birge-Sponer extrapolation of the ν_{OH} and 3ν_{OH} band origins yields the necessary information to estimate the 4ν_{OH} band origin. Unlike the previous analysis of 3ν_{OH}, the much smaller extrapolation up to 4ν_{OH} is now sufficiently accurate to demonstrate an immediate and unambiguous correspondence between predicted and experimentally determined spectra. Based on this simulation, preliminary rotational assignments for the low-J_{KaKc} transitions are readily made and rigorously confirmed by ground state combination differences.

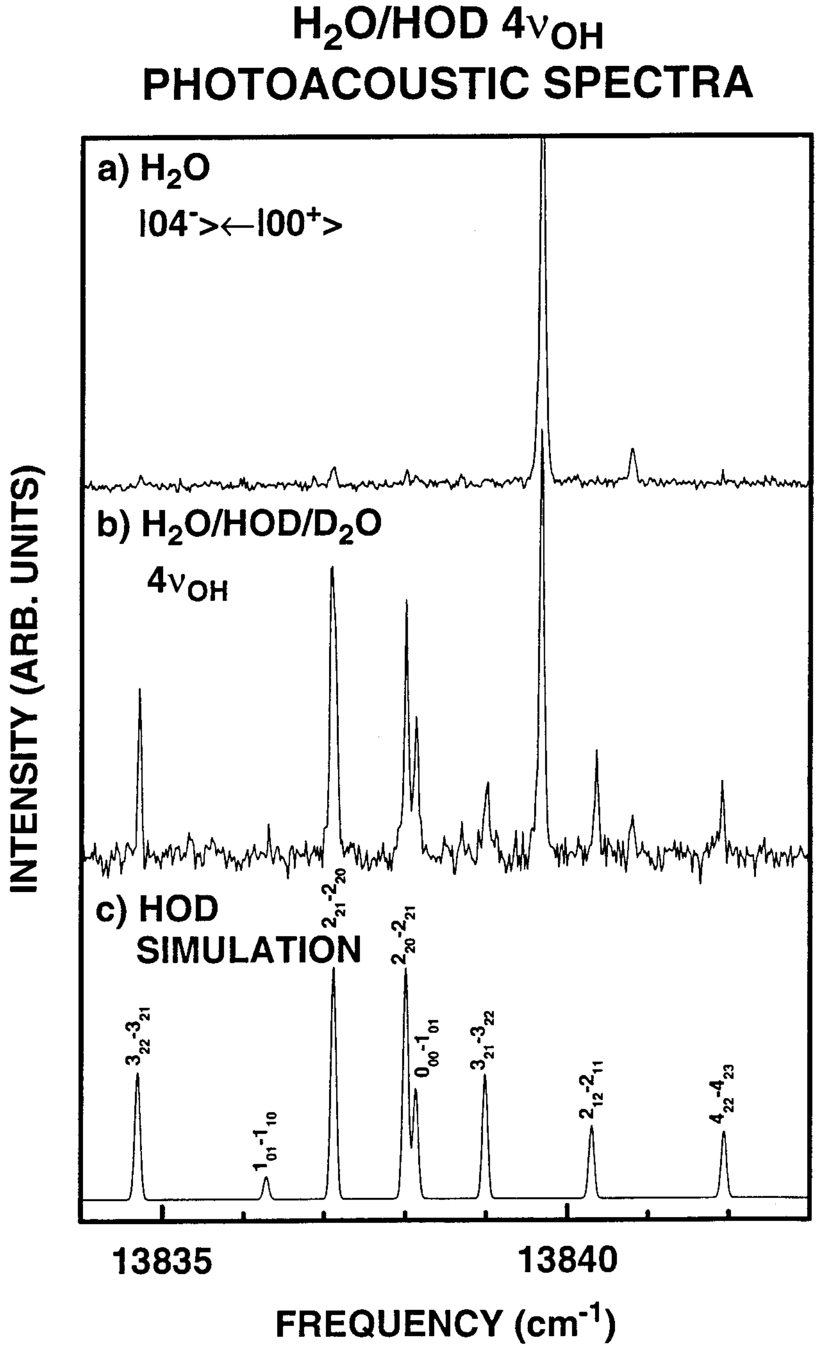

Figure 2.2. Sample of the photoacoustic spectra in the $4\nu_{OH}$ overtone region of the OH stretch for (a) H_2O and (b) $H_2O/HOD/D_2O$ (≈1:2:1) cells. Transitions present in only the $H_2O/HOD/D_2O$ cell are exclusively from HOD. (c) Simulation of the HOD spectrum using A, B, and C rotational constants and vibrational origin obtained from a least-squares fit of a Watson asymmetric top Hamiltonian to the transitions in Table 2.4. The constants from the fit are given in Table 2.5.

This procedure quickly leads to a complete rotational assignment of HOD transitions in the spectral region scanned. The measured HOD $4\nu_{OH}$ overtone absorption frequencies and rotational assignments are provided in Table 2.4.

By analogy to analysis of the $3\nu_{OH}$ overtone band, these transitions are least-squares fit to a Watson asymmetric top Hamiltonian (I^r representation) including up to quartic terms. While the frequency precision is lower than for $3\nu_{OH}$, the transitions are fit by these parameters to within $2\sigma = 0.09$ cm^{-1} (see Table 2.5). The quality of fit is demonstrated in Fig. 2.2b and c, comparing a 9 cm^{-1} section of the photoacoustic spectrum with the least-squares prediction. As with the $3\nu_{OH}$ band, the $J \leq 5$ transitions are also fit to a rigid rotor Hamiltonian, with the results given in Table 2.3.

Also reported in Table 2.5 are the $4\nu_{OH}$ band origin predictions from Tennyson and co-workers,[22] as well as the previous estimates of the $4\nu_{OH}$ band origin and rotational constants from Brouard and Langford.[14] Note that the agreement between theoretical and experimental band origins is extremely good, to within 0.1 cm^{-1}. Conversely, there is 8.7-cm^{-1} discrepancy between our results and the previously reported values of Brouard and Langford. As anticipated, the agreement between current and previous values is far better for the rotational constants, though there still are appreciable discrepancies outside our experimental uncertainties for A and B. Again, given the significant differences in our own work between uncorrected dye laser readings and the HITRAN database for the $4\nu_{OH}$ H_2O lines, it is apparent that independent calibration of the dye laser scan is absolutely essential in obtaining accurate transition frequencies.

Table 2.4. Observed $4\nu_{OH}$ transitions in HOD.

J'	K_a'	K_c'	J''	K_a''	K_c''	ν (cm^{-1})	J'	K_a'	K_c'	J''	K_a''	K_c''	ν (cm^{-1})
5	1	5	6	0	6	13760.92(-3)	6	3	4	6	3	3	13811.37(3)
4	1	3	5	1	4	13764.65(4)	5	3	3	5	3	2	13814.58(-1)
4	0	4	5	1	5	13771.89(1)	4	0	4	4	1	3	13814.74(-3)
3	2	1	4	2	2	13772.59(4)	2	1	2	3	0	3	13815.135(-2)
3	2	2	4	2	3	13774.78(5)	1	1	0	2	1	1	13815.92(-2)
4	1	4	5	1	5	13774.99(2)	4	3	2	4	3	1	13816.52(-2)
4	0	4	5	0	5	13775.85(5)	5	3	2	5	3	3	13816.99(-4)
4	1	4	5	0	5	13778.94(5)	4	3	1	4	3	2	13817.17(0)
3	1	2	4	1	3	13781.81(0)	3	3	1	3	3	0	13817.79(0)
3	0	3	4	1	4	13785.46(-1)	3	3	0	3	3	1	13817.86(-1)
7	4	4	7	4	3	13786.00(1)	6	3	3	6	3	4	13818.20(2)
6	4	3	6	4	2	13787.83(-1)	1	1	1	2	1	2	13820.95(-8)
6	4	2	6	4	3	13788.21(1)	5	2	4	5	2	3	13822.14(0)
5	4	2	5	4	1	13789.33(0)	1	0	1	2	0	2	13822.53(-8)
5	4	1	5	4	2	13789.37(-4)	0	0	0	1	1	1	13823.81(-2)
2	2	0	3	2	1	13789.87(0)	3	0	3	3	1	2	13825.31(-8)
4	4	0	4	4	1	13790.62(2)	4	2	3	4	2	2	13829.96(-3)
4	4	1	4	4	0	13790.62(2)	3	1	3	3	1	2	13830.67(-2)

Table 2.4. Observed $4\nu_{OH}$ transitions in HOD. (*continued*)

J'	K_a'	K_c'	J''	K_a''	K_c''	ν (cm^{-1})	J'	K_a'	K_c'	J''	K_a''	K_c''	ν (cm^{-1})
3	1	3	4	1	4	13790.77(1)	3	2	2	3	2	1	13834.72(0)
2	2	1	3	2	2	13791.02(2)	1	0	1	1	1	0	13836.31(2)
3	0	3	4	0	4	13791.71(6)	2	2	1	2	2	0	13837.11(-1)
3	1	3	3	2	2	13791.89(14)	2	2	0	2	2	1	13838.01(0)
3	1	3	4	0	4	13796.89(-10)	0	0	0	1	0	1	13838.13(0)
2	0	2	3	1	3	13798.20(8)	3	2	1	3	2	2	13839.00(0)
2	1	1	3	1	2	13798.93(3)	2	1	2	2	1	1	13840.36(5)
5	1	4	5	2	3	13805.59(-6)	4	2	2	4	2	3	13841.92(-7)
2	1	2	3	1	3	13806.07(-2)	1	1	1	1	1	0	13846.64(-3)
2	1	1	2	2	0	13806.19(10)	5	2	3	5	2	4	13847.34(2)
2	0	2	3	0	3	13807.14(-5)	1	1	0	1	1	1	13852.33(2)
1	0	1	2	1	2	13810.63(-2)	2	1	1	2	1	2	13857.27(4)

[a] Numbers in parentheses are residual differences from predicted transition frequencies from the fit.

Table 2.5. HOD $4\nu_{OH}$ spectroscopic constants[a] (in cm^{-1}).

A	19.443(9)
B	9.054(8)
C	6.094(4)
Δ_J	$3.5(18)\times10^{-2}$
Δ_{JK}	$5(8)\times10^{-2}$
Δ_K	$8.7(9)\times10^{-1}$
d_J	$1.9(14)\times10^{-2}$
d_K	$-2(17)\times10^{-2}$
ν_0	13853.636(28)

[a] Uncertainties represent two standard deviations obtained from the least-squares fit.

Of special relevance to the direction of the overtone transition dipole moment in HOD, the ratio of a-type to b-type intensities is determined from the photoacoustic scans to be 6.7(5):1. It is worth noting that this ratio is more than *twice* as large as the 2.7(10):1 value observed for $3\nu_{OH}$, thus indicating significant changes in the alignment of the transition dipole moment vector with OH stretch excitation. We will return to this point later in the discussion section.

2.4 Discussion

2.4.1 OH stretch dependence of HOD rovibrational constants

The vibrational dependence of the rotational constants can be most simply characterized by a low-order Dunham expansion in the OH stretch quantum, i.e.,

$$A_v = A_e + \alpha_e^A (v_{OH} + ½) \tag{2.1a}$$

$$B_v = B_e + \alpha_e^B (v_{OH} + ½) \tag{2.1b}$$

$$C_v = C_e + \alpha_e^C (v_{OH} + ½) \tag{2.1c}$$

As shown in Fig. 2.3a, the data quantitatively corroborate a linear dependence on v_{OH}. These Dunham expressions can be extrapolated to the OH vibrational minimum at $v_{OH} \approx -½$; the corresponding "equilibrium" HOD rotational constants (corrected for zero-point motion in the OH stretch coordinate only) and values for α_e^A, α_e^B, and α_e^C are listed in Table 2.6. Note the anomalously large sensitivity of A_v to v_{OH}, decreasing by nearly 20% from $v_{OH} = 0$ to $v_{OH} = 4$. The results of these rotational

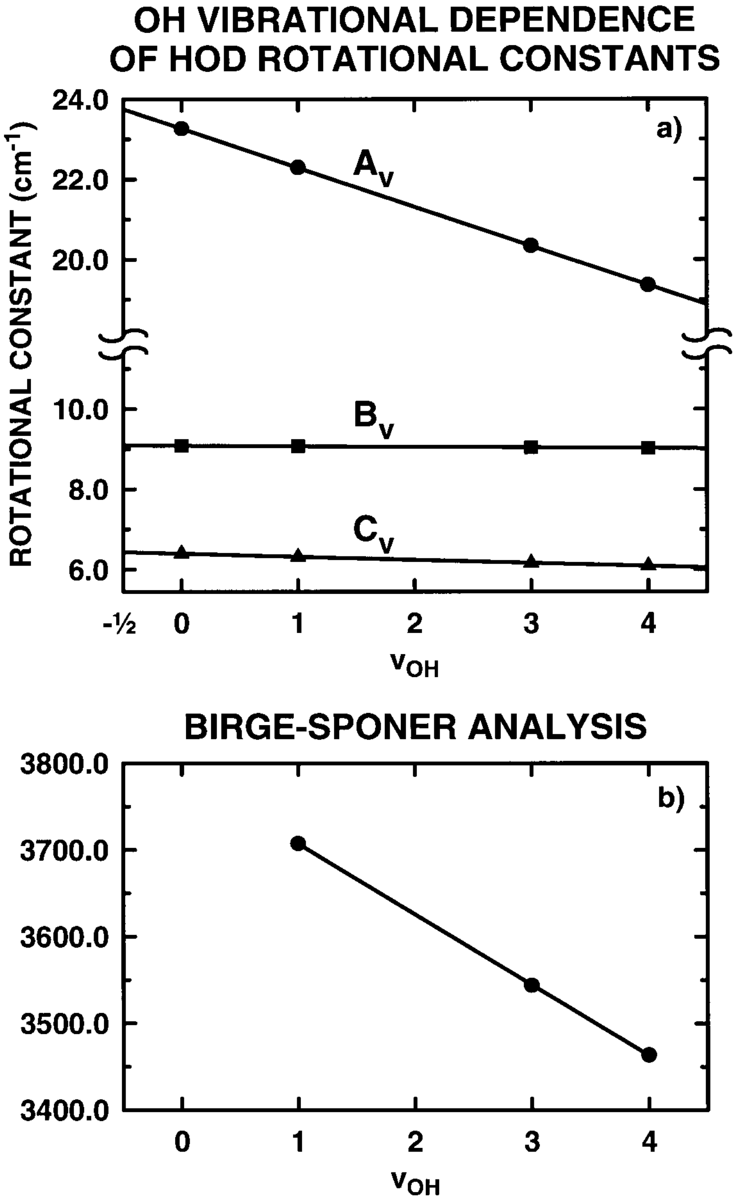

Figure 2.3. Rotational constants and vibrational origins obtained from least-squares fits of a rigid-rotor Watson asymmetric top Hamiltonian to ground-state data and ν_{OH}, $3\nu_{OH}$, and $4\nu_{OH}$ transitions in HOD (see Table 2.3). (a) Least-squares fits of a low-order Dunham expansion (Eqns. 2.1a-c) to A_v, B_v, and C_v reveal the strong linear dependence of these rotational constants on OH vibrational quantum. Note in particular the ≈20% change in A_v from $v_{OH} = 0$ to 4. (b) The ν_{OH}, $3\nu_{OH}$, and $4\nu_{OH}$ vibrational origins are fit to a Birge-Sponer expression $(\nu_0 / v_{OH}) = -(\omega_e x_e)v_{OH} + (\omega_e - \omega_e x_e)$. The linearity of this plot indicates near Morse oscillator behavior in the OH stretch of HOD. The "equilibrium" rotational constants (corrected for zero-point motion of OH only), α_e's, harmonic frequency ω_e, and vibrational anharmonicity $\omega_e x_e$ obtained from these fits are given in Table 2.6.

Table 2.6. HOD Dunham coefficients[a] (in cm^{-1}) for OH stretch excitation.

A_e	23.749(12)
B_e	9.092(3)
C_e	6.435(3)
α_e^A	-0.9751(41)
α_e^B	-0.0141(10)
α_e^C	-0.0772(11)
ω_e	3869.9(19)
$\omega_e x_e$	81.4(6)

[a] Uncertainties represent two standard deviations obtained from the least-squares fit.

analyses can also be stated in terms of inertial defect ($\Delta = I_C - I_B - I_A$), which for a rigid planar molecule should essentially vanish. As listed in Table 2.3 for v_{OH}=0 to 4, the inertial defects for HOD are consistently ≈0.05 amu·Å^2 and yet all slightly positive due to large amplitude in-plane zero-point vibrational motion.[25,26]

The series of HOD band origins for ν_{OH} can be fit to the standard Birge-Sponer expression

$$E_v = \omega_e (v_{OH} + ½) - \omega_e x_e (v_{OH} + ½)^2 \qquad (2.2)$$

to obtain harmonic frequencies and vibrational anharmonicities. A corresponding Birge-Sponer plot of the ν_{OH}, $3\nu_{OH}$, and $4\nu_{OH}$ band origins given in Table 2.3 and shown in Fig. 2.3b yields ω_e = 3869.9(19) cm^{-1} and $\omega_e x_e$ = 81.4(6) cm^{-1} (see Table 2.4). For a simple 1D Morse oscillator model of the OH stretch vibration, the equilibrium bond strength, D_e, is related to the vibrational anharmonicity by $\omega_e x_e = \omega_e^2/(4D_e)$. This translates into an equivalent Morse oscillator dissociation energy of $D_0 \approx D_e - ½\omega_e \approx$ 126(3) kcal/mol, in reasonable agreement with the experimental D_0 value for H_2O of 119(1) kcal/mol.[27]

2.4.2 Intramolecular alignment of the transition dipole moment vector

The relative a-type to b-type intensity ratios for $3\nu_{OH}$ and $4\nu_{OH}$ are 2.7(10):1 and 6.7(5):1, respectively. These values can be further augmented by data from Benedict *et al.* for ν_{OH},[10] which yield an a-type to b-type ratio of 1.4(1):1. These data clearly indicate a strong dependence of intensity ratios, and thus the intramolecular alignment of the HOD transition dipole moment vector, on OH vibrational quanta. Our analysis proceeds as follows. For sufficiently small amplitude vibrations, vibrational and rotational motion can be approximately decoupled; in this limit, the transition dipole moment vector is defined by

$$\vec{M}_{v'\text{-}v''} = \left\langle v' \middle| \vec{\mu}(\vec{R}) \middle| v'' \right\rangle \tag{2. 3}$$

In Eqn. 2.3, $\vec{\mu}(\vec{R})$ is the dipole moment operator, $\vec{R}$ represents all internal displacement coordinates, and thus $\vec{M}_{v'\text{-}v''}$ is solely a function of initial (v") and final (v') vibrational state. For vibrational excitation in a triatomic asymmetric top such as HOD, this transition dipole moment vector lies in the molecular plane and therefore supports "hybrid" a- and b-type bands. The fractional intensity of each type is determined by the angle between the transition moment and the a and b inertial axes, respectively. Figure 2.4 depicts the location of these inertial axes as referenced to the HOD equilibrium geometry.

In terms of $\vec{M}_{v'\text{-}v''}$, the fractional a-type or b-type intensities of a vibrational band can be written as

$$I_{a/b} = \frac{\left|\vec{M}_{v'\text{-}v''} \cdot (\vec{a}/\vec{b})\right|^2}{\left|\vec{M}_{v'\text{-}v''} \cdot \vec{a}\right|^2 + \left|\vec{M}_{v'\text{-}v''} \cdot \vec{b}\right|^2} \tag{2.4}$$

where $\vec{a}$ and $\vec{b}$ are unit vectors along the a and b axes. This expression can be more

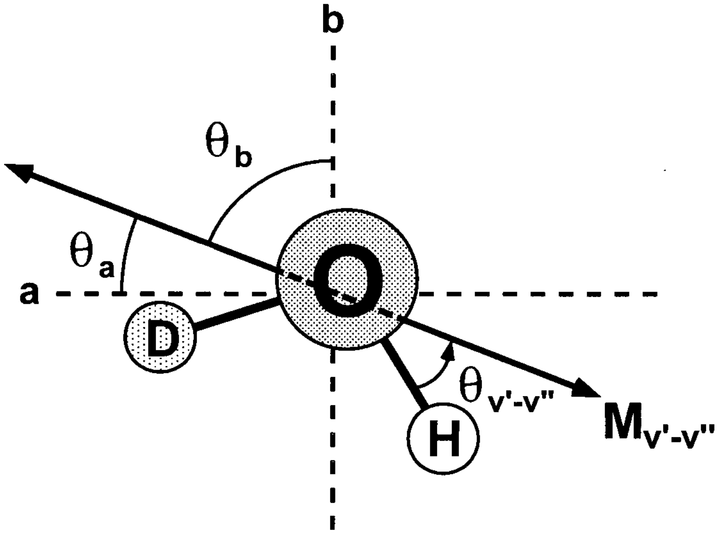

Figure 2.4. Diagram of the alignment of the transition dipole moment, $\vec{M}_{v'-v''}$, in the plane of the HOD molecule. The geometry of HOD with respect to the a and b axes of the molecule is determined from the equilibrium bond lengths and bond angles given by Benedict *et al.*[10] The angle $\theta_{v'-v''}$ between $\vec{M}_{v'-v''}$ and the OH bond is listed in Table 2.7 for the OH vibrational series ν_{OH}, $3\nu_{OH}$, and $4\nu_{OH}$.

conveniently rewritten in terms of experimentally measured a-type to b-type intensity ratios as

$$\frac{I_a}{I_b} = \frac{\left|\vec{M}_{v'-v''} \cdot \vec{a}\right|^2}{\left|\vec{M}_{v'-v''} \cdot \vec{b}\right|^2} = \frac{\cos^2\theta_a}{\cos^2\theta_b} = \cot^2\theta_a \qquad (2.5)$$

where θ_a and θ_b are the angles between $\vec{M}_{v'-v''}$ and the $\vec{a}$ and $\vec{b}$ axes, with $\theta_a + \theta_b = \pi/2$. Based on the known HOD equilibrium geometry[10] and θ_a determined from Eqn. 2.5, the angle between the transition dipole moment vector and the vibrationally excited OH bond is given by $\theta_{v'-v''} \approx 59° - \theta_a$ (see Fig. 2.4). Table 2.7 summarizes the results for the series of OH stretch overtone transitions. Interestingly, $\vec{M}_{v'-v''}$ does not lie along the OH bond, i.e., $\theta_{v'-v''} \neq 0$. Furthermore, there is a clear *counterclockwise* rotation of the transition dipole moment *away* from the OH bond with increasing vibrational excitation.

Table 2.7. Experimental and theoretical angle between the transition dipole moment and the OH bond.

Band	2D, bond-dipole	2D, dipole surface	3D, dipole surface	Experiment
ν_{OH}	3°	25°	24(1)°	19(1)°
$3\nu_{OH}$	1°	31°	29(1)°	28(2)°
$4\nu_{OH}$	1°	40°	36(1)°	38(1)°

[a] Uncertainties represent two standard deviations obtained from the least-squares fit.

In order to gain physical insight into these trends, we next predict the intramolecular alignment of $\vec{M}_{v'-v''}$ at various levels of theory. This requires solving for the wave functions $\Psi_{v'}(\vec{R})$ and $\Psi_{v''}(\vec{R})$ for each vibrational level and choosing a trial form of the dipole moment surface, $\vec{\mu}(\vec{R})$. The transition dipole moment $\vec{M}_{v'-v''}$ can then be calculated directly from Eqn. 2.3.

The first approach we explore in an attempt to reproduce the behavior of the experimental transition moment vector is based on a simple linear “bond-dipole” model of the vibrational excitation.[28-30] Explicitly, this calculation involves approximating the dipole moment surface of the molecule by placing point charges at each of the atoms ($+\delta$ at H and D, -2δ at O) that are not allowed to redistribute with vibrational excitation. Stated simply, this model predicts a purely linear dependence of dipole moment on OH/OD stretch excitation and therefore explicitly neglects contributions from "electrical anharmonicity" in the dipole moment surface. The potential energy surface for nuclear displacements is taken from Polyansky *et al*.[23] The vibrational wave functions on this potential surface are then obtained by solving for the two-dimensional (2D) OH/OD stretching wavefunctions with the bend coordinate fixed at 104.5°. Such a model includes only the "mechanical anharmonicity" inherent in the OH stretching coordinate and furthermore neglects any mixing between pure stretching excitations and bend-stretch combinations.

As can be seen from Fig. 2.5 and Table 2.7, this calculation qualitatively fails to reproduce the experimental results. Specifically, $\theta_{v'-v''} \approx 0$; that is, $\vec{M}_{v'-v''}$ is predicted to lie nearly along the OH bond for each overtone transition. This behavior is easily understood by examining in more detail the OH/OD stretch nature of this excitation. The dependence of the 2D wave functions on number of OH stretch quanta is shown in Fig. 2.6 from the ground state up to $v_{OH} = 4$. These plots show extremely little mixing with the OD stretch coordinate, r_{OD}, consistent with a pure "local-mode" stretch excitation along the OH bond. In this limit, the dipole moment vector $\vec{\mu}(\vec{R})$ can be expanded in a Taylor series in r_{OH} to produce the following

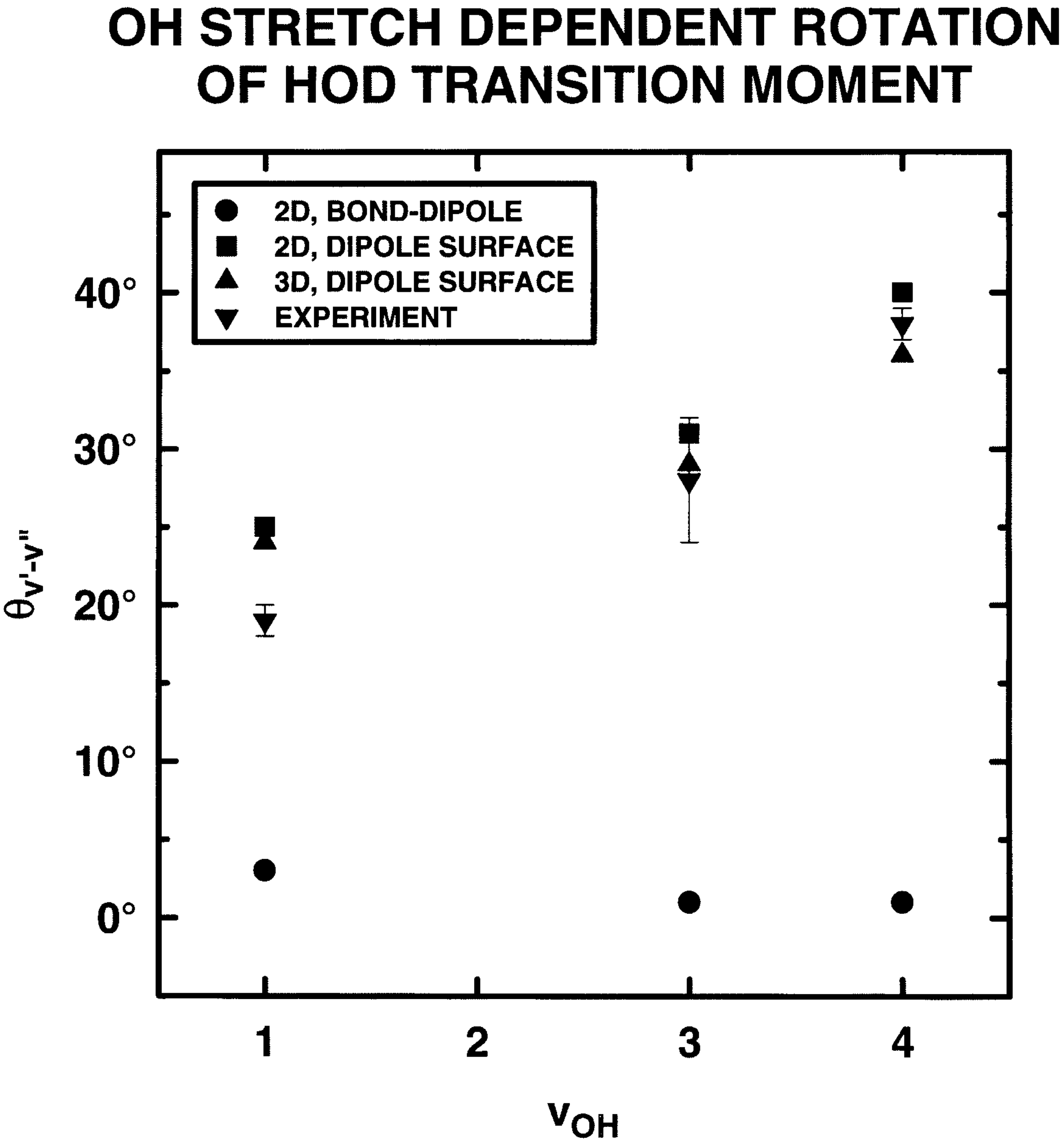

Figure 2.5. Plot of the experimentally and theoretically determined angle of $\vec{M}_{v'-v''}$ with the OH bond for a series of OH stretch excitations (see Table 2.7). Despite the local-mode nature of the OH stretch excitation, this angle grows to almost 40° for the highest measured vibrational band ($4\nu_{OH}$). This figure clearly demonstrates the failure of the bond-dipole approximation to reproduce the experimentally determined angles, as well as the near-quantitative agreement between experiment and calculations, which include the dipole surface of water from Gabriel *et al.*[30]

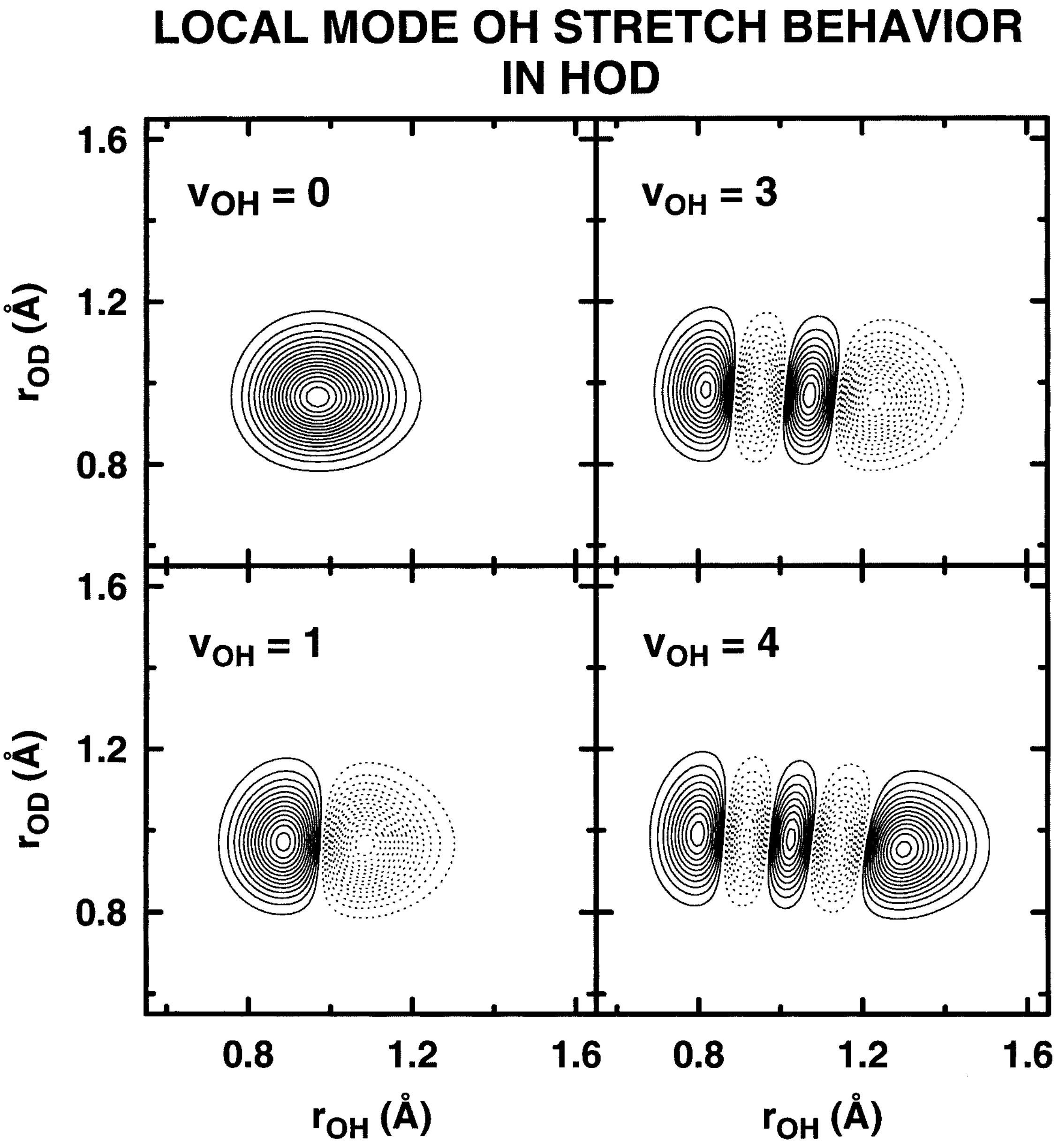

Figure 2.6. Plot of the 2D OH/OD stretch wavefunctions for v_{OH} = 0, 1, 3, and 4 calculated on the potential energy surface of H_2O from Polyansky *et al.*[23] The uniformity in the OD coordinate among OH vibrational levels demonstrates the nearly pure "local-mode" character of the OH stretch in HOD.

expression for the transition moment $\vec{M}_{v'\text{-}v''}$:

$$\vec{M}_{v'\text{-}v''} = \vec{\mu}\Big|_{r_{OH}=r_e} \langle v'|v''\rangle \quad + \quad d\vec{\mu}/dr_{OH}\Big|_{r_{OH}=r_e} \langle v'|(r_{OH} - r_e)|v''\rangle \quad + \quad \ldots \quad (6)$$

For anything but a pure rotational transition with $\Delta v=0$, the first term in $\vec{M}_{v'\text{-}v''}$ is zero due to orthogonality of the different vibrational wave functions. In the local-mode, bond-dipole approximation, the only nonvanishing contribution to $\vec{M}_{v'\text{-}v''}$ arises from $d\vec{\mu}/dr_{OH}$. Since only the component of $\vec{\mu}$ parallel to the OH bond changes with r_{OH}, $\vec{M}_{v'\text{-}v''}$ would thus lie parallel to the OH bond, with $\theta_{v'\text{-}v''} = 0$. These predictions are in clear disagreement with experiment, indicating that a more sophisticated model of the HOD dipole moment surface is necessary. The small but nonvanishing values of $\theta_{v'\text{-}v''}$ predicted from this model simply reflect weak mixing of OH and OD stretch vibrations due to a perturbative breakdown of the local-mode picture.

A much improved dipole moment surface can be obtained from the *ab initio* work of Gabriel *et al.*[31] which conveniently provides $\vec{\mu}(\vec{R})$ as an explicit function of intramolecular coordinates. A second set of predictions for the overtone transition moment vector is performed with this alternate dipole surface but still for 2D OH/OD stretch degrees of freedom. Thus, this model incorporates “electrical anharmonicity” in the dipole surface while still neglecting possible coupling between bend and stretch excitations. The results of these calculations are reported in Table 2.7 and plotted in Fig. 2.5. Both the magnitude of $\theta_{v'\text{-}v''}$ and the vibrationally dependent “tilt” away from the OH bond are now in quite reasonable agreement with experiment. These results provide strong confirmation of the dipole moment surface of Gabriel *et al.* and indicate that electrical anharmonicity in the H_2O dipole moment surface plays the dominant role in intramolecular alignment of $\vec{M}_{v'-v''}$ in the OH overtone stretch manifold of HOD.

In principle, there could be additional contributions to this intramolecular alignment of $\vec{M}_{v'-v''}$ from mixing between HOD bend and OH/OD stretch motion on the potential energy surface. Indeed, the role of 2:1 Fermi resonant bend-stretch coupling has proven quite important in theoretical studies of intramolecular vibrational relaxation (IVR) in overtone CH excited hydrocarbons.[31-37] Furthermore, it is conceivable that overall rotation of the HOD molecule can be responsible for an enhanced Coriolis-induced coupling of the different vibrational modes. As a final test, therefore, we relax all constraints on vibrational mode mixing by repeating these HOD calculations in all 3 intramolecular and 3 overall rotational degrees of freedom. To do this, we use the TRIATOM suite of programs developed by Tennyson *et al.*[38] to calculate rovibrational wave functions on the full 3D potential energy surface of Polyansky *et al.*[23] These wave functions are then used with the same dipole moment surface of Gabriel *et al.* to predict the series of OH stretch overtone spectra in HOD, explicitly calculating intensities of J_{KaKc}-resolved HOD rovibrational transitions. These rovibrational transitions can in turn be readily assigned and their intensities used to determine the theoretical alignment, $\theta_{v'-v''}$, of the transition moment vector as a function of OH overtone excitation via Eqn. 2.5. The results in Table 2.7 and Fig. 2.5 demonstrate that this potential and dipole surface also reproduce $\theta_{v'-v''}$ quite adequately as well as the experimentally observed tilt away from the OH bond with increasing OH vibrational excitation. However, the agreement is not appreciably improved from the simpler 2D calculations for the OH stretch manifold, indicating that stretch-bend interactions are not as important as electrical anharmonicity in controlling the alignment of the transition dipole moment vector in HOD.

Finally, with the *ab initio* dipole moment surface for water, one can now explicitly investigate why the transition moment vector "tilts" away from the OH bond with overtone stretch excitation. This is difficult to represent for a 2D vector quantity as a function of three intramolecular coordinates. However, as one compromise, Fig. 2.7 displays the two nonvanishing orthogonal projections of the full dipole surface i) $\mu_{\|}$ parallel to the OH bond and ii) $\mu_{\perp}$ perpendicular (but in plane) to the OH bond, where a positive sense of $\mu_{\|}$ and $\mu_{\perp}$ corresponds to the O-H and ≈O-D bond directions, respectively. These two projections are plotted as a function of r_{OH}, with the OD bond length and HOD bend angle fixed near the equilibrium values. To establish the relevant length scale, the equilibrium OH separation and classical turning points for $v_{OH} = 4$ are indicated. In qualitative agreement with the linear bond-dipole model, the component of $\vec{\mu}$ *parallel* to the OH bond varies approximately linearly with r_{OH}, though with some additional curvature at high r_{OH}. However, in clear contrast to bond-dipole predictions, the corresponding *perpendicular* component of $\vec{\mu}$ is far from independent of the OH bond length. Indeed, the magnitude of $\mu_{\perp}$ decreases by nearly 30% of the increase in $\mu_{\|}$ over the range of $v_{OH} = 4$ classical turning points. The latter implies $d\mu_{\perp}/dr_{OH}$ is nonzero, and specifically that the component of $\vec{M}_{v'-v''}$ perpendicular to the OH bond is nonzero. Consequently, $\vec{M}_{v'-v''}$ must rotate *away from* the OH bond, in direct contrast to the bond-dipole picture.

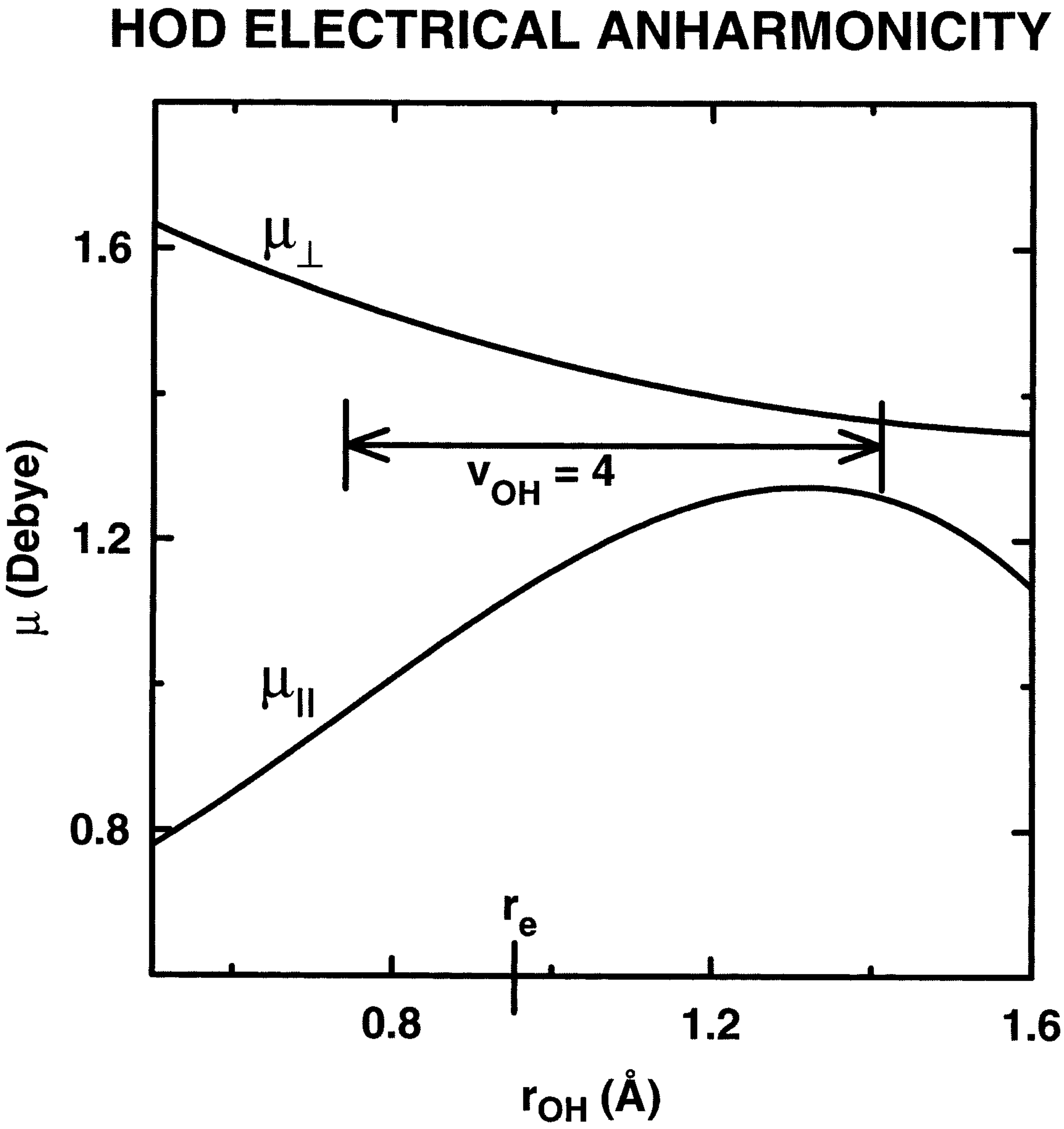

Figure 2.7. Components of the dipole moment surface of HOD (= dipole surface of H_2O from Gabriel *et al.*[30]) parallel ($\mu_\parallel$) and perpendicular ($\mu_\perp$) to the OH bond as a function of r_{OH}, at the equilibrium values of the OD bond length and HOD bend angle. The equilibrium OH bond length and the classical turning points for $v_{OH} = 4$ are noted. As expected, $\mu_\parallel$ is roughly linear in OH bond displacement for sufficiently small r_{OH}, i.e., consistent with a simple bond-dipole model. However, over the same range of displacements, $\mu_\perp$ strongly *decreases* with r_{OH}, which is in direct contrast with bond-dipole predictions and responsible for *counterclockwise* rotation of the vibrational transition moment vector ($\vec{M}_{v'-v''}$) away from the OH bond axis.

As a final note, the combination of Fig. 2.7 and a nearly perpendicular HOD bond angle imply that the component of the dipole moment along the OD bond must be *decreasing* with OH stretch excitation over the range of $r_{OH} < 1.6$ Å. However, this trend must eventually reverse, since in the limit of infinite r_{OH} separation, $\vec{\mu}$ asymptotically approaches the dipole moment of isolated OD radical. This would yield $\mu_{\perp}=\sin(104.5^{o})\cdot$ 1.65 D $\approx$ 1.60 D,[39] which is substantially larger than the $\approx$1.35 D value theoretically predicted at $r_{OH} = 1.6$ Å. This behavior further underscores the dramatic importance of electrical anharmonicity in the dipole moment surface and therefore the relevance of detailed comparisons between *ab initio* theory and experiment for such fundamental molecular systems as H_2O.

2.5 Summary

High-resolution infrared and visible photoacoustic spectroscopy is used to investigate the second and third OH stretch overtone bands of HOD. Rotational analysis of these data permits A_v, B_v, and C_v rotational constants and vibrational origins to be determined for $v_{OH} = 3$ and 4. In conjunction with earlier studies of the ground state and first OH stretch excited manifold, the vibrational dependence of these spectroscopic data can be well fit by simple Dunham and Birge-Sponer analyses in v_{OH}. More quantitatively, the $3\nu_{OH}$ and $4\nu_{OH}$ vibrational origins for HOD (in the Born-Oppenheimer approximation) can be used to test the accuracy of current *ab initio*/empirical potential energy surfaces by Polyansky *et al.* Agreement between experiment and full 3D quantum variational calculations on this surface is excellent: 0.8 cm^{-1} and 0.1 cm^{-1} for $3\nu_{OH}$ and $4\nu_{OH}$, respectively.

Experimental intensities of a-type and b-type transitions within each of the ν_{OH}, $3\nu_{OH}$, and $4\nu_{OH}$ manifolds are analyzed to determine the intramolecular alignment of the transition dipole moment vector. This vector is found to lie significantly away from the OH bond and furthermore “tilts” systematically with increasing OH stretch excitation. These results are in clear contrast with simple bond-dipole model predictions, which for a local-mode excitation would be perfectly aligned along the OH bond, suggesting the importance of electrical anharmonicity in the dipole moment surface. This is explicitly tested by further comparison with predictions from an *ab initio* dipole moment surface of Gabriel *et al.*, which are in excellent qualitative agreement with experimental results. The absence of significant contributions to this transition dipole alignment from bend-stretch rotationally induced vibrational mixing is explicitly tested by comparing 2D OH/OD stretch calculations (i.e., at fixed HOD bend angle) with full QM variational rovibrational calculations (with both 3D vibrational and external rotational motion included). These overtone results underscore the importance of nonlinear effects in the dipole moment surface (i.e., electrical anharmonicity) as the predominant influence on intramolecular alignment of the transition dipole moment vector.

References for Chapter 2

1. R. L. Vander Wal, J. L. Scott, F. F. Crim, K. Weide, and R. Schinke, *J. Chem. Phys.* **94,** 3548 (1991).

2. A. Sinha, M. C. Hsiao, and F. F. Crim, *J. Chem. Phys.* **94,** 4928 (1991).

3. R. B. Metz, J. D. Thoemke, J. M. Pfeiffer, and F. F. Crim, *J. Chem. Phys.* **99,** 1744 (1993).

4. J. D. Thoemke, J. M. Pfeiffer, R. B. Metz, and F. F. Crim, *J. Phys. Chem.* **99,** 13748 (1995).

5. I. Bar, Y. Cohen, D. David, S. Rosenwaks, and J. J. Valentini, *J. Chem. Phys.* **93,** 2146 (1990).

6. I. Bar, Y. Cohen, D. David, T. Arusi-Parpar, S. Rosenwaks, and J. J. Valentini, *J. Chem. Phys.* **95,** 3341 (1991).

7. Y. Cohen, I. Bar, and S. Rosenwaks, *J. Chem. Phys.* **102,** 3612 (1995).

8. M. J. Bronikowski, W. R. Simpson, B. Girard, and R. N. Zare, *J. Chem. Phys.* **95,** 8647 (1991).

9. F. C. De Lucia, R. L. Cook, P. Helminger, and W. Gordy, *J. Chem. Phys.* **55,** 5334 (1971).

10. W. S. Benedict, N. Gailar, and E. K. Plyler, *J. Chem. Phys.* **24,** 1139 (1956).

11. A. D. Bykov, V. A. Kapitanov, O. V. Naumenko, T. M. Petrova, V. I. Serdyukov, and L. N. Sinitsa, *J. Mol. Spec.* **153,** 197 (1992).

12. D. F. Plusquellic, O. Votava, and D. J. Nesbitt, *J. Chem. Phys.* **109,** 6631 (1998).

13. Votava, O., Plusquellic, D. F., Mackenzie, S. R., Fair, J. R., Nesbitt, D. J. (in preparation).

14. M. Brouard and S. R. Langford, *J. Chem. Phys.* **106,** 6354 (1997).

15. J. Michl and E. W. Thulstrup, *Spectroscopy with polarized light: solute alignment by photoselection in liquid crystals, polymers, and membranes* (VCH, 1995).

16. O. Votava, J. R. Fair, D. F. Plusquellic, E. Riedle, and D. J. Nesbitt, *J. Chem. Phys.* **107,** 8854 (1997).

17. D. F. Plusquellic, O. Votava, and D. J. Nesbitt, *Appl. Opt.* **35,** 1464 (1996).

18. E. Riedle, S. H. Ashworth, J. T. Farrell, Jr., and D. J. Nesbitt, *Rev. Sci. Instrum.* **65,** 42 (1994).

19. T. M. Niebauer, J. E. Faller, H. M. Godwin, J. L. Hall, and R. L. Barger, *Appl. Opt.* **27,** 1285 (1988).

20. Rothman, L. S., HITRAN database (ONTAR, 1996)

21. L. S. Rothman, R. R. Gamache, R. H. Tipping, C. P. Rinsland, M. A. H. Smith, D. C. Benner, V. M. Devi, J.-M. Flaud, C. Camy-Peret, A. Perrin, A. Goldman, S. T. Massie, L. R. Brown, and R. A. Toth, *J. Quant. Spectrosc. Radiat. Transfer* **48,** 469 (1992).

22. Tennyson, J., private communication

23. O. L. Polyansky, P. Jensen, and J. Tennyson, *J. Chem. Phys.* **105,** 6490 (1996).

24. J. K. G. Watson, *J. Chem. Phys.* **46,** 1935 (1967).

25. T. Oka and Y. Morino, *J. Mol. Spec.* **6,** 472 (1961).

26. J. K. G. Watson, *J. Chem. Phys.* **98,** 5302 (1993).

27. J. A. Kerr, *Chem. Rev.* **66,** 465 (1966).

28. I. Schek, J. Jortner, and M. L. Sage, *Chem. Phys. Lett.* **64,** 209 (1979).

29. M. L. Sage and J. Jortner, *Adv. Chem. Phys.* **47,** 293 (1981).

30. M. S. Child and L. Halonen, *Adv. Chem. Phys.* **57,** 1 (1984).

31. W. Gabriel, E.-A. Reinsch, P. Rosmus, S. Carter, and N. C. Handy, *J. Chem. Phys.* **99,** 897 (1993).

32. D. J. Nesbitt and R. W. Field, *J. Phys. Chem.* **100,** 12735 (1996).

33. E. L. Sibert, III, W. P. Reinhardt, and J. T. Hynes, *Chem. Phys. Lett.* **92,** 455 (1982).

34. E. L. Sibert, III, W. P. Reinhardt, and J. T. Hynes, *J. Chem. Phys.* **81,** 1115 (1984).

35. E. L. Sibert, III, W. P. Reinhardt, and J. T. Hynes, *1984* **81,** 1135 (1984).

36. M. Quack, *Ann. Rev. Phys. Chem.* **41,** 839 (1990).

37. M. Quack and W. Kutzelnigg, *Ber. Bunsenges. Phys. Chem.* **99,** 231 (1995).

38. J. Tennyson, J. R. Henderson, and N. G. Fulton, *Comput. Phys. Commun.* **86,** 175 (1995).

39. D. D. Nelson, Jr., A. Schiffman, D. J. Nesbitt, J. J. Orlando, and J. B. Burkholder, *J. Chem. Phys.* **93,** 7003 (1990).

CHAPTER 3

OPEN-SHELL CLUSTER FORMATION VIA LASER PHOTOLYSIS: QUASICLASSICAL TRAJECTORY STUDIES OF Ar_n-H_2S AND Ar_n-SH CLUSTER DYNAMICS

3.1 Introduction

Over the past decade, the study of radical van der Waals complexes has been the focus of considerable interest. An especially active area in this field has been the study of rare gas-radical hydride cluster species, with particular emphasis on complexes of rare gases such as Ne, Ar, and Kr with OH(OD),[1-22] and SH(SD)[23-28] radicals, which have been mapped out both experimentally and theoretically. Such prototype systems are ideal for developing an understanding of radical solvation and close-range inelastic energy transfer effects, as well as providing the fundamental basis for further studies of radical complexes with reactive species.[1,29-31]

Typical preparation methods of such rare-gas/radical clusters involve generation of the radical from an appropriate hydride precursor (e.g., SH/OH from H_2S, H_2O) via UV photolysis or discharge, followed by coexpansion of the radical with the rare-gas partner in a supersonic jet. The spectroscopy and dynamics of these clusters can then be probed via laser-induced fluorescence (LIF) or resonance-enhanced multiphoton ionization (REMPI) by pumping to rovibrational levels of an excited electronic state, usually many centimeters downstream from the source. High-resolution studies of these vibrationally and rotationally cold clusters have provided a wealth of spectroscopic information about intermolecular potential energy surfaces in the electronically excited-state; a recent example is the development of high quality empirical potential energy surfaces by Miller and coworkers for R-SH complexes (R = Ar, Kr, Ne)[26,27] out of the first excited $(\tilde{A})$ state. Such studies do not, however, significantly explore the ground-state cluster potential surface, since the collisional cooling process produces population overwhelmingly in the lowest rovibrational levels. While this cooling clearly aids in the spectroscopic analysis of the excited state, it also limits the range of ground-state quantum states available for dynamical studies. Alternative spectroscopic methods for characterizing the ground-state potential surface have been stimulated emission pumping studies by Lester and coworkers on Ar/Ne-OH[13,32,33] as well as the dispersed fluorescence studies of Miller and coworkers on Ne-OH[19] and Ne/Ar/Kr-SH.[28]

At the same time, a number of studies have been carried out investigating photodissociation dynamics in small clusters. Systems sampled by these techniques include complexes of one or few rare-gas atoms with small molecules, in an effort to link gas-phase photolysis of monomer precursors with photodissociation in solvated environments. These studies raise the intriguing possibility that the photolyzed atom can, in some circumstances, leave behind a bound, highly excited *open-shell* cluster. Several groups have previously provided indirect experimental evidence for such products; examples include I-HI from $(HI)_n$ photodissociation[34] and Ar-I from Ar-HI photodissociation.[35] Theoretical calculations by Juanes-Marcos and Garcia-Vela of Ar-Cl from Ar-HCl photolysis[36,37] and Bowman and coworkers of Ar-OH from Ar-H_2O have also predicted these open-shell cluster products.[38]

More recently, direct spectroscopic evidence from our group has been presented for the production of bound, rovibrationally excited radical clusters from photolysis of closed-shell precursor clusters.[38-40] Via this technique, the rare gas and UV chromophore are coexpanded in a slit supersonic jet to form cold, closed-shell clusters. The monomer hydride is then photolyzed within the cluster, the fast H atom escapes with high efficiency, and the resulting radical cluster is probed via LIF. The time delay (typically 100 ns) between photolysis and probe lasers is shorter than the timescale for subsequent collisions in the jet, thus probing strictly *unimolecular* dynamics for formation of open-shell clusters.

Specifically, this technique has been demonstrated to be an efficient source of hot Ar-SH and Ar_2-SH radical clusters from photolysis of Ar-H_2S and Ar_2-H_2S followed by H atom ejection. Since these open-shell clusters are formed with high internal excitation, this in principle opens up a wide range of the ground-state potential surface for detailed investigation. An important preliminary and dynamically intriguing question to address, however, is how such a relatively "violent" photolysis event can produce weakly bound radical clusters so *efficiently*. Figure 3.1 outlines the key features of this process. Ar_n-SH (n = 1, 2) clusters are formed from Ar_n-H_2S photolysis via the following sets of pathways:

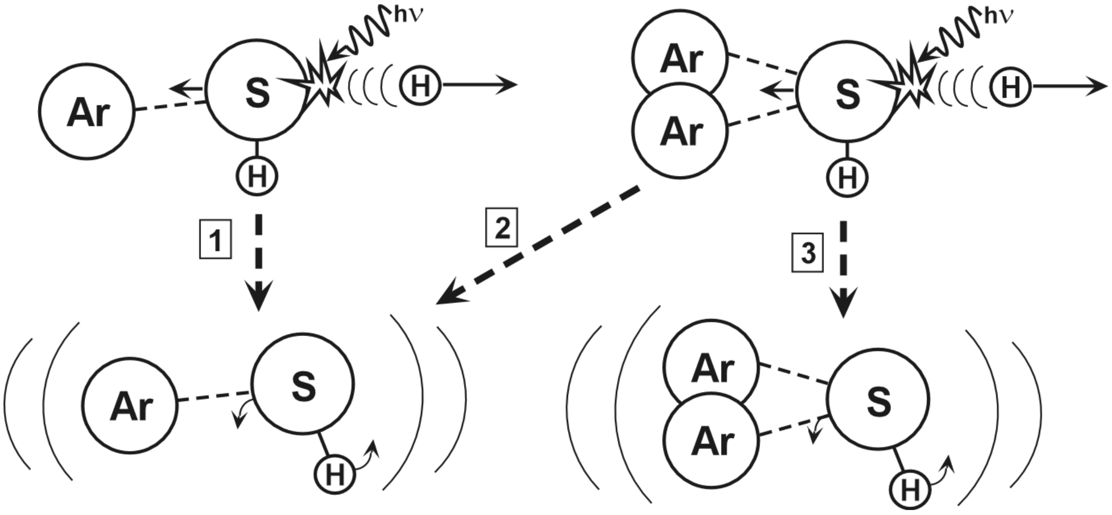

Figure 3.1. Schematic representation of the production of Ar_n-SH (n = 1, 2) clusters from photolysis of Ar_n-H_2S precursors. Pathways 1 and 3 depict "nonfragmentary" photolysis, in which excess energy is accommodated by the cluster, and pathway 2 depicts a "boil-off" mechanism, in which excess energy is removed by the escape of an Ar atom.

$$\mathrm{Ar_n\text{-}H_2S + h\nu \rightarrow Ar_n\text{-}SH + H} \qquad (3.1)$$

$$\mathrm{Ar_n\text{-}H_2S + h\nu \rightarrow Ar_{n-1}\text{-}SH + Ar + H} \qquad (3.2)$$

Ar_n-SH radical clusters are in effect produced by two mechanisms: i) "boil off," in which one Ar atom escapes to remove excess energy, and ii) "nonfragmentary," in which this excess energy is successfully accommodated by the remaining radical cluster. Indeed, it is initially surprising that the clusters survive this photolysis process at all: the excess photolysis energy is as much as two orders of magnitude larger than the radical-cluster binding energy in this interaction. The simple dynamical explanation is that by conservation of momentum, the light H atom can carry off as much as 95% of the photolysis energy. The remaining excess energy from H_2S photolysis is further reduced by transformation into the Ar_n-SH center-of-mass (COM) frame, which further increases the probability that internal energy will not exceed the binding energy of the open-shell cluster.

While simple conservation principles begin to explain how the energy is disposed, several dynamical aspects warrant further investigation. First of all, previous experimental work has provided estimates of the efficiency of each formation process by comparison with LIF signals from SH monomer populations in the jet. However, uncertainty in radiative lifetimes of the monomer and cluster species, as well as the extent of Ar_n-H_2S clustering in the jet, distribute these estimates over approximately an order of magnitude range. Second, we would like to probe the energetics of cluster formation, with particular attention to the "nonfragmentary" photolysis pathways (i.e., where no additional Ar atom is boiled off to stabilize the nascent complex). Experimentally, the dominant features in the cluster LIF spectra have been attributed to intermolecular progressions (e.g. van der Waals stretch and librational modes) out of the lowest vibrational states of Ar-SH and Ar_2-SH. However, this cannot explain the strong intensity peaking at the highest-energy end of the spectrum, which one speculates arise from highly internally excited clusters near the dissociation limit in the ground electronic state. Thus, it is necessary to show that the intracluster photolysis process can produce highly rovibrationally excited (albeit long-lived) molecules, as well as to study how that excess intermolecular energy is distributed. Furthermore, once these hot free-radical clusters are generated by unimolecular photolysis, they experimentally exhibit a much slower cooling on a 10-μs timescale. It is therefore interesting to determine whether this is a purely due to bimolecular cooling by collisions (which would imply remarkably high energy-transfer efficiencies), or if any *noncollisional* processes (such as unimolecular dissociation of clusters with $E > D_e$) might contribute to the decrease in average internal excitation.

In order to address these issues, we have used quasiclassical trajectory calculations to simulate the unimolecular photolysis dynamics in Ar-H_2S and Ar_2-H_2S photolysis. In these simulations, the ground-state Ar_n-H_2S wavefunction is used to generate and sample from an appropriate distribution of initial coordinates and momenta. This initial wavefunction is projected (in a Franck-Condon sense) onto an excited-state, repulsive surface on which the photolysis dynamics are calculated. The resulting trajectories allow us to explore the dynamics of H atom photoejection and subsequent stabilization of the open-shell van der Waals cluster. The remainder of this chapter is organized as follows. Section 3.2 describes the details of the computational methodology for generating initial conditions and calculating the photolysis trajectories. Section 3.3 describes the results of these quasiclassical trajectories, including the lifetimes of radical clusters, the energetics and dynamics of cluster formation, and branching ratios among photolysis products. Section 3.4 summarizes the key conclusions of this study.

3.2 Computational Details

3.2.1 Ground-state potential surfaces: *Ar_n-$H_2S(\tilde{X})$*

In order to generate the initial conditions for Ar_n-H_2S and subsequently calculate the photodissociation dynamics, two potential surfaces are required: one for the ground electronic state, Ar_n-$H_2S(\tilde{X})$, and one for the first excited electronic state accessed by the photolysis pulse. Neglecting three-body terms, one could calculate what one needs with only the relevant two n=1 (i.e., Ar-H_2S) surfaces; unfortunately, neither dimer potential surface is currently available. However, for our current purpose we can obtain a qualitatively correct description of the initial state sampling simply by substituting the $V(R,\theta,\phi)$ Ar-H_2O potential of Cohen and Saykally(AW2),[41] where R represents the distance from the Ar atom to the center of mass of the H_2S (i.e., H_2O) subunit; θ, rotation of the Ar *in* the H_2S plane; and ϕ, Ar rotation *out of* this plane. In these coordinates, $(\theta, \phi) = (0°, 0°)$ is defined with Ar along the C_{2v} axis of the H_2S, proximal to the H atoms. The minimum energy configuration is located at $(R, \theta, \phi) = (3.636$ Å, $74.3°, 0°)$, i.e., rotated 74.3° away from the C_{2v} axis in the plane of the H_2O, with an energy of 143 cm^{-1}. The ground-state wavefunction for this system is highly angularly delocalized with near free rotation in θ. The sampling for the larger Ar_2-H_2S clusters requires an Ar-Ar potential as well. This interaction is described by the semiempirical Ar-Ar interaction potential of Aziz and Chen (HFD-C[42]), with a well depth of 99.5 cm^{-1} and an equilibrium Ar-Ar distance of 3.759 Å.

3.2.2 *Excited-state potential surfaces:* Ar_n-$H_2S(\tilde{A})$

In the excited state, the interaction between the Ar and H_2S subunits can no longer be approximated by the corresponding Ar-H_2O surface, since the dissociative H-SH interaction lies at the heart of the excited-state potential. Furthermore, an intermolecular vibrational SH potential must be included for any dynamics calculations. Since the H_2S is thus fragmented into two subunits, the dissociative H atom and the remaining SH radical, the interaction between the Ar and H_2S is likewise separated into Ar-SH and Ar-H interactions.

The dissociative potential of the H_2S monomer is modeled after the *ab initio* calculations of Theodorakopoulos *et al.* for the lowest dissociative state, the $1^1A''$ state.[43] In these calculations, the non-breaking SH bond distance (r) and HSH bond angle are fixed at their equilibrium values (2.52 Å and 92.2°), and the excited-state potentials are calculated as a function of the breaking SH bond distance. The lowest adiabatic dissociative state represents two strongly coupled diabatic states ($^1A_2$ and $^1B_1$) crossing near 2.2 a_0 and as such is not well modeled by a single exponential fit.[44] To approximate this state, we fit the *ab initio* points outside the crossing region, i.e., those with $r > 2.2\ a_0$, to a single exponential. The parameters obtained from this exponential fit are given in Table 3.1. As noted above, this potential is essentially only valid for a fixed non-breaking SH bond distance and HSH bond angle; however, for a rapid photodissociation process, the H atom should depart before any significant SH rotation or vibration occurs. Thus, we calculate this potential based solely on the dissociative SH bond distance. The remaining, nondissociating bond in the H_2S

subunit is modeled by a Morse oscillator potential with parameters obtained from Ramsay (see Table 3.1).[45]

Table 3.1. Parameters of the potential.

HS-H Dissociation: $V = A \exp(-Br_{HS-H})$	
A	482417 cm^{-1}
B	2.36/Å
SH Stretch: $V = D_e(1-\exp(-\alpha(r-r_e))^2$	
r_e	1.34 Å
D_e	30419 cm^{-1}
α	1.86/Å

No full potential is available for the Ar-SH interaction; we have thus chosen to adapt the spin-orbit averaged Ar-OH potential of Lester, Clary, and coworkers[13] by replacing the mass of oxygen with the mass of sulfur. This potential is defined in Jacobi coordinates (R, θ), with R as the distance from the Ar to the OH center of mass, and θ as the angle between R and the OH internuclear axis ($\theta = 0°$ for H pointed toward the Ar). The minimum energy is 127 cm^{-1} in the linear OH-Ar configuration, and the equilibrium distance between the Ar and the OH center of mass is 3.7 Å. This surface overestimates the binding energy of Ar-SH: D_0 for Ar-OH is 107 cm^{-1},[3] while D_0 for Ar-SH is estimated to be 82 cm^{-1}.[24] In addition, a recent model potential developed by Yang *et al.* demonstrates that the Ar-SH ground-state potential is weaker, but more isotropic, than the Ar-OH potential.[28] We thus expect that our calculations may overestimate the number of bound Ar_n-SH clusters formed from Ar_n-H_2S photolysis; however, the effects on the *relative* efficiencies for Ar-SH and Ar_2-SH production should be less significant. The remaining interaction for Ar-H_2S, i.e., Ar-H, is modeled by the potential of Tang and Toennies.[46]

For Ar_2-H_2S, the Ar-Ar interaction is described by the potential of Aziz and Chen used for the ground electronic surface (Sect. 3.2.1).

3.2.3 Initial-condition sampling

The initial conditions for the quasiclassical trajectory calculations are generated in two steps; the first involves sampling the ground-state potential surface in a manner approximately consistent with the ground-state wavefunction. This process is initially detailed for the Ar-H_2S calculations, after which the necessary modifications for the Ar_2-H_2S photolysis simulations are described.

To sample the ground-state potential energy surface also requires a rough estimate of the ground-state zero-point energy. The zero-point energy of Ar-H_2O is 44.65 cm^{-1} above the potential minimum.[47] In the pseudodiatomic approximation, this energy is proportional to the inverse square root of the reduced mass; thus, we scale the Ar-H_2O zero-point energy by $\sqrt{\mu_{Ar-H_2O}/\mu_{Ar-H_2S}}$ for Ar-H_2S, resulting in an energy eigenvalue of 36.68 cm^{-1}. The zero-point energy for the trimer (Ar_2-H_2S) is estimated as twice that of the dimer (Ar-H_2S), since there are now two such pseudodiatomic modes.

Next, we generate a microcanonical ensemble of relative Ar-H_2S positions, i.e., with each initial condition having a total energy equal to this ground-state zero-point energy. Most quasiclassical sampling techniques based on the ground-state eigenfunction typically require first calculating the eigenfunction, then weighting the sampling of coordinates and momenta consistent with the probability distribution. However, for the present purposes, the ground-state potential is quite approximate, thus a more qualitative sampling method will suffice. To that end, we sample the relative positions of the Ar and H_2S subunits with a probability that decreases exponentially with potential energy. This distribution mimics the relationship between the ground-state potential energy function and probability distribution of a harmonic oscillator.

For a one-dimensional, quantum-mechanical harmonic oscillator, the ground-state probability distribution is described by

$$\mathrm{P(R)} = \left|\Psi_{\mathrm{H.O.}}\right|^2 = \mathrm{N}e^{-\mu\omega \mathrm{R}^2/\hbar} \qquad (3.5)$$

where N is a normalization constant, μ is the reduced mass of the oscillator, and ω is its vibrational frequency. Since the potential energy of the harmonic oscillator is given by $V(R) = \frac{1}{2}\mu\omega^2R^2$, and its ground-state energy, $E_{g.s.}$, is equal to $\hbar\omega/2$, this probability distribution can be rewritten as

$$\mathrm{P(R)} = \mathrm{N}e^{-\mathrm{V(R)}/\mathrm{E}_{\mathrm{g.s.}}} \qquad (3.6)$$

with V(R) = 0 at the potential minimum. Thus, the probability distribution in coordinate space for a harmonic oscillator is an exponentially decreasing function of the potential energy, with P maximized at the potential minimum and down by a factor of *e* at the classical turning points (i.e., where $V = E_{g.s.}$). This probability distribution thus reproduces the classically allowed region of a 1D harmonic oscillator and goes to zero in the classically forbidden regions.

In a similar vein, we describe the probability in coordinate space for an Ar at a particular point on the Ar-H_2S surface by:

$$P(R,\theta,\phi) = Ne^{-V_{Ar\text{-}H_2S}(R,\theta,\phi)/E_{g.s.}} \qquad (3.7)$$

where $E_{g.s.} = 44.65\ cm^{-1}$ and $V_{Ar\text{-}H_2S}(R,\theta,\phi)$ is the Ar-H_2S potential energy. Operationally, we sample the Ar-H_2S surface by randomly placing the Ar within a (10 Å)^3 box centered on the H_2S. If the potential energy at this point is greater than the ground-state eigenenergy, this initial condition is rejected; otherwise, its relative probability is calculated from Eqn. 3.7 (with N fixed to 1), and compared with a random number on the interval [0,1]. If the calculated probability is greater than this random number, this initial position is accepted. A similar procedure is carried out for the Ar_2-H_2S clusters. Since for two separable harmonic oscillators, the total probability is given by the product of the probabilities for the individual oscillators, the total Ar_2-H_2S probability is estimated as

$$P = Ne^{-\left[V_{Ar^1\text{-}H_2S}+V_{Ar^2\text{-}H_2S}\right]/E_{g.s.}} \qquad (3.8)$$

where $E_{g.s.}$ is the ground-state energy of a *single* Ar-H_2S interaction. A plot of 500 initial Ar-H_2S positions is given in Fig. 3.2. In this plot, x and y are coordinates in the H_2S plane defined with respect to its COM: y lies along the C_{2v} axis, with positive y above the S atom, and z is perpendicular to the plane. The maximum density of initial positions peaks at the Ar-H_2S minimum, but the spread in points adequately represents the "floppy" nature of the intermolecular potential.

Once the relative Ar-H_2S positions, and thus the Ar-H_2S potential energy, has been determined, the remaining zero-point energy is placed in kinetic energy relative to the center of mass of the cluster. In the frame of a stationary H_2S, the magnitude of this momentum for the single-Ar case is approximately

$$p_{\mathrm{Ar}} = m_{\mathrm{Ar}} \sqrt{\frac{2\left(E_{\mathrm{g.s.}} - V_{\mathrm{Ar\text{-}H_2S}}\right)}{\mu_{\mathrm{Ar,H_2S}}}} \tag{3.9}$$

where $\mu_{\mathrm{Ar,H_2S}}$ is the reduced mass of the Ar and H_2S subunits. The orientation of the Ar velocity with respect to the H_2S subunit is then randomly selected. A plot of this distribution of momenta relative to the H_2S is given in Fig. 3.3. For the two-Ar case, the relative orientation of the two momenta also affects total energy in the COM frame. Consequently, the magnitudes and relative orientations of the momenta are randomly sampled up to the maximum value given by Eqn. 3.9. The final momenta are then each scaled such that the resulting kinetic energy in the COM frame is consistent with the chosen zero point and potential energies.

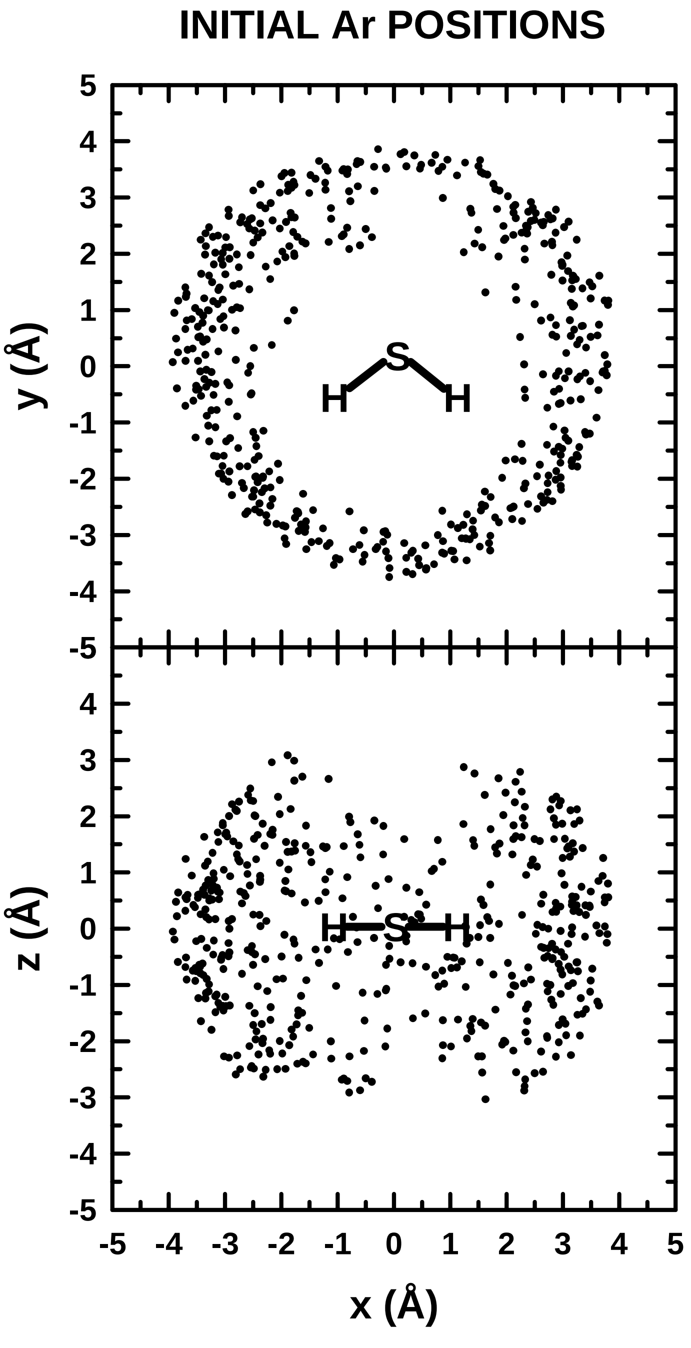

Figure 3.2. Initial condition sampling for the Ar position relative to the H_2S subunit for 500 trajectories of Ar-H_2S. With respect to the COM of H_2S, x and y are in the H_2S plane, with positive y above the S atom and along the C_{2v} axis; z is perpendicular to this plane. The sampling probability decreases exponentially with potential energy, so that the maximum density is at the Ar-H_2S minimum and the spread in points mimics the “floppy” nature of the intermolecular potential.

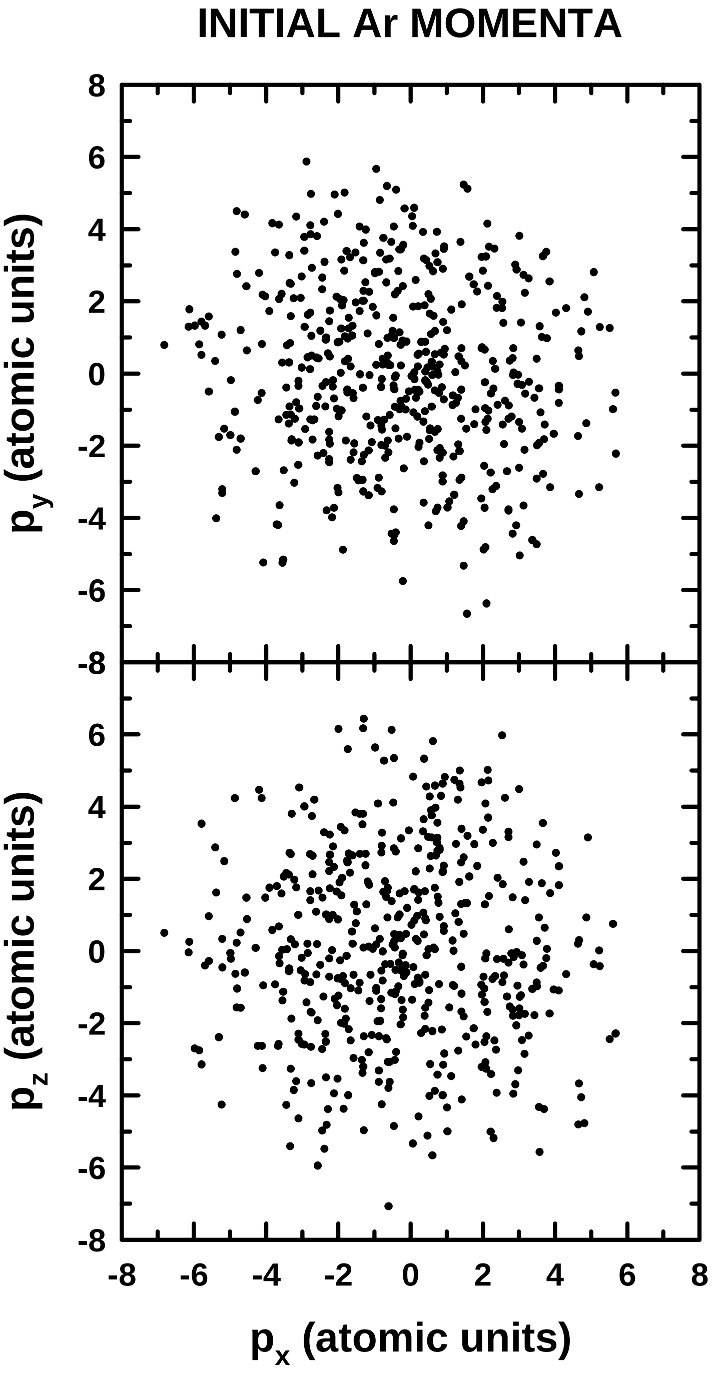

Figure 3.3. Initial condition sampling for the Ar momentum relative to the H_2S subunit for 500 trajectories of Ar-H_2S, with coordinates defined as in Figure 3.2. All excess ground state energy above the Ar-H_2S potential energy is placed in Ar momentum, with random orientation with respect to the H_2S subunit.

3.2.4 Photoexcitation and trajectory calculations

Once the initial positions and momenta for the Ar and H_2S subunits are determined, each initial condition is promoted to the excited-state surface, and the internal energy is adjusted to equal the excess energy from the photolysis. If this process were strictly vertical (in a Franck-Condon sense), the relative positions and momenta of the atoms would be unchanged by the photoexcitation. Simply substituting the ground-state potential with the excited-state potential, however, would not ensure the appropriate excited-state internal energy, i.e., the sum of the initial ground-state and photolysis energies minus the SH bond dissociation energy. Since the part of the $\tilde{A}$-state potential surface most relevant to the photolysis is the dissociative H-SH bond potential, we optimize the dissociative H-SH bond distance so that the total energy in the cluster is equal to the appropriate excited-state internal energy. In effect, this step initially places all of the photoexcitation into potential energy. Two cases are examined: photolysis at 248 nm, which provides 8855 cm^{-1} above the bond dissociation energy, and at 193 nm, which provides 20,300 cm^{-1} of excess energy.

Once the initial conditions are projected onto the excited-state surface in this manner, the photodissociation trajectories are calculated by integrating Hamilton's equations of motion in Cartesian coordinates with a variable-order, variable-stepsize, Adams-method numerical integrator.[48] Trajectories are typically integrated until all Ar-SH distances exceed 20 a_0, or until a fixed integration time has elapsed (1 ns for Ar-H_2S photolysis, 250 ps for Ar_2-H_2S). Conservation of energy is verified to be better than one part in 10^6, more typically in 10^7, over the duration of each trajectory.

Approximately 500 trajectories are initially calculated for each initial cluster size and photolysis wavelength; additional trajectories are subsequently calculated as detailed in the next section. For each trajectory, the momenta and positions of all atoms are recorded as a function of time, typically in 60-fs steps, for subsequent analysis of product branching ratios, lifetimes of cluster species, energetics of bound clusters, and dynamical pathways.

3.3 Results

Our first step in examining the results of these photolysis trajectory calculations is to determine the timescale on which the radical clusters are formed and fall apart, as well as to take a preliminary look at which species are generated. Next, we analyze the energetics of the radical clusters, first by investigating the overall energy partitioning among the various rotational and vibrational modes of the cluster for the whole product distribution, then by focusing on individual trajectories. This examination leads to a discussion of the dynamics of cluster formation, and more specifically, the role of cluster angular momentum. Finally, we bring these pieces together in order to determine overall product branching ratios for comparison with experimental results.

3.3.1 Time-dependent radical concentrations

We begin the trajectory calculations by examining the 193-nm photolysis of Ar-H_2S and Ar_2-H_2S, for which the simplest picture emerges. The concentrations of radical species as a function of time after photolysis for Ar-H_2S and Ar_2-H_2S

photolysis at this wavelength are depicted in Figs. 3.4a and b. Both calculations converge on this 1-ns timescale: the concentration of each radical species levels off such that little change occurs past the 10-ps mark, i.e., few additional radical clusters would be predicted to fall apart if the calculations were continued for additional time. As seen in Fig. 3.4a, the concentration of bound Ar-SH formed from Ar-H_2S drops dramatically such that by the end of the calculation, little or no bound radical cluster product remains.

In contrast, for Ar_2-H_2S photolysis, a significant amount of Ar-SH remains bound: the calculation levels off with roughly 20% of the trajectories following this pathway. Yet few or no trajectories produce Ar_2-SH product. Taken together, these two calculations demonstrate that for 193-nm photolysis of Ar-H_2S and Ar_2-H_2S, the primary product is Ar-SH, formed from "boiling off" one Ar atom from Ar_2-H_2S photolysis. This result is not surprising: 193-nm photolysis releases 20,300 cm^{-1} of excess energy; even a dynamical reduction by 20 ($\approx M_{HS}/M_H$) is an order of magnitude larger than can be accommodated in the cluster without boiling off at least one subunit.

The photolysis of Ar-H_2S and Ar_2-H_2S at 248 nm reveals more complex behavior (Figs. 3.4c and d). In both cases, significant numbers of radical clusters survive for the duration of the calculation (1 ns for Ar-H_2S and 250 ps for Ar_2-H_2S precursors). These cluster concentrations level off for Ar-H_2S photolysis (note the log (time) axis), suggesting satisfactory convergence in the calculations. For the Ar-H_2S precursor, Ar-SH appears to be formed at 248 nm with roughly 20% efficiency,

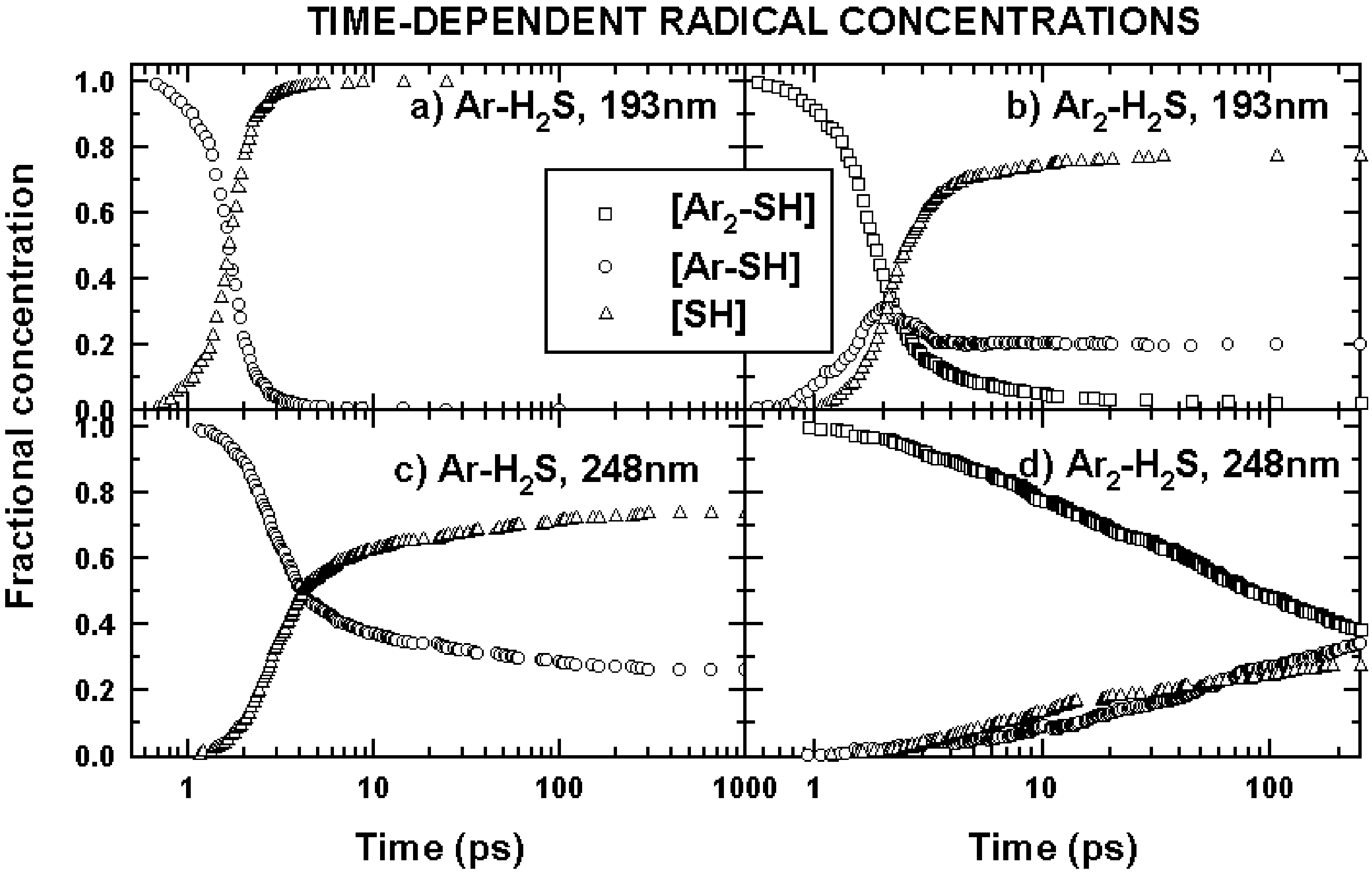

Figure 3.4. Time-dependent radical concentrations from photolysis of Ar$_n$-H$_2$S clusters at two wavelengths. a) Ar-H$_2$S photolysis at 193 nm. b) Ar$_2$-H$_2$S photolysis at 193 nm. c) Ar-H$_2$S photolysis at 248 nm. d) Ar$_2$-H$_2$S photolysis at 248 nm.

providing additional confirmation that the nonfragmentary photolysis channel for Ar-H_2S can indeed result in significant open-shell cluster formation. By way of contrast, the radical cluster species concentrations for 248 nm Ar_2-H_2S photolysis do not appear to stabilize asymptotically on the 250-ps timescale of this calculation. Rather, the Ar_2-SH concentrations decrease approximately linearly with logarithmic time, such that ~25% of the initially formed Ar_2-SH clusters fragment with each 10-fold increase in time.

These calculations clearly support a significant channel for open-shell radical cluster (Ar-SH or Ar_2-SH) formation at both 193 nm and 248 nm. The dominant channel at 193 nm is Ar-SH formed by fragmentary photolysis, i.e., ejection of a hot H atom from Ar_2-H_2S followed by boil-off a single Ar atom. The efficiency for this open-shell cluster formation process is much higher at 248-nm photolysis, since there can now be contributions from both nonfragmentary Ar-H_2S and Ar_2-H_2S photolysis as well as from Ar_2-H_2S photolysis followed by subsequent boil off. Since the Ar_2-H_2S photolysis at 248 nm has not converged, it cannot yet be determined how many additional Ar_2-SH clusters will fall apart, nor what products they will form. At this stage, then, it is difficult to probe the relative importance of the photolysis pathways.

In principle, this issue could be resolved by carrying out the calculations for a longer time. However, based on the near-linear dropoff of Ar_2-SH concentration with *logarithmic* time, a calculation nearly two orders of magnitude longer would be required for convergence. Rather than simply extending the computational time, we first examine the energetics and dynamics of cluster formation to look for a way to predict propensities towards various pathways and to estimate final branching ratios.

In the ensuing analysis, we primarily focus on the photolysis of Ar-H_2S at 248 nm; results for clusters of all types will then be summarized in Sect. 3.3.4.

3.3.2 Energetics of radical cluster formation

In the corresponding experimental work, our group observed that photolysis of weakly bound closed-shell precursors produced rotationally and vibrationally hot radical clusters. Accordingly, we will explore the energetics of bound radical clusters formed from Ar-H_2S photolysis at 248 nm, looking at the total energy left in the cluster as well as how it is partitioned among the various rotational and vibrational modes.

As can be observed in Fig. 3.4c, the trajectories divide into two groups: those in which the radical cluster falls apart to form Ar and SH, and those which remain bound on the timescale of the calculation (1 ns). Since this calculation is nearly converged (i.e., the radical concentrations level off), we can then separately examine the energetics of bound and unbound clusters, assuming that those clusters remaining bound on this timescale will be bound for all time. In doing this, we take advantage of the rapid departure of the H atom; once it has left the precursor closed-shell cluster, no additional forces act upon the resulting radical cluster, and thus all energy in the COM frame of the radical cluster remains there for all time. Consequently, we can calculate the COM energy of the radical cluster immediately after the H atom has departed. Thus, the calculation can be halted when the H atom interaction with the cluster is negligible; this point is chosen to be 20 a_0 away from the S atom, where the

H-SH interaction is less than 10^{-14} cm^{-1}. To obtain better statistics for the subsequent analysis, we have calculated an additional 5000 trajectories of Ar-H_2S at 248 nm.

Figure 3.5 contains a histogram of the energy remaining in the Ar-SH COM frame after photolysis, separated into bound and unbound at the end of the 1-ns calculation. Superimposed is a dividing line at the dissociation energy of the Ar-SH (i.e., Ar-OH) potential surface, $D_e = 127$ cm^{-1}. As expected, all unbound clusters have internal energy greater than D_e; however, only approximately half of the bound clusters (henceforth "energetically bound") have E less than D_e, and *half* (henceforth "quasibound") have E *greater than* D_e. This result is initially puzzling: it would seem that all clusters with $E > D_e$ should ultimately fall apart.

To investigate further, we first determine the partitioning of energy in all bound Ar-SH clusters (i.e., energetically bound and quasibound) by separating the internal energy into E_{vdW} (cluster van der Waals stretch energy), E_{rot} (cluster end-over-end rotation), and E_{SH} (vibration and libration of the SH subunit). Since E_{SH} is significantly smaller than E_{vdW} and E_{rot} (i.e., ≤ 10%), we can focus exclusively on the E_{vdW} and E_{rot}, with histograms of the energy partitioning given in Fig. 5.6. The clusters are quite vibrationally hot; however, the E_{vdW} distribution ends abruptly at the dissociation limit. The excess cluster energy lies rather in rotation, with the end-over-end rotational energy distribution extending significantly beyond the dissociation limit (Fig. 5.6b).

The reason behind this unequal partitioning is clear: only E_{vdW} (not E_{rot}) $> D_e$ will cause the cluster to dissociate. However, for quasibound clusters (i.e., with total E > De), sufficient transfer from E_{rot} to E_{vdW} might seem inevitable. In contrast, the

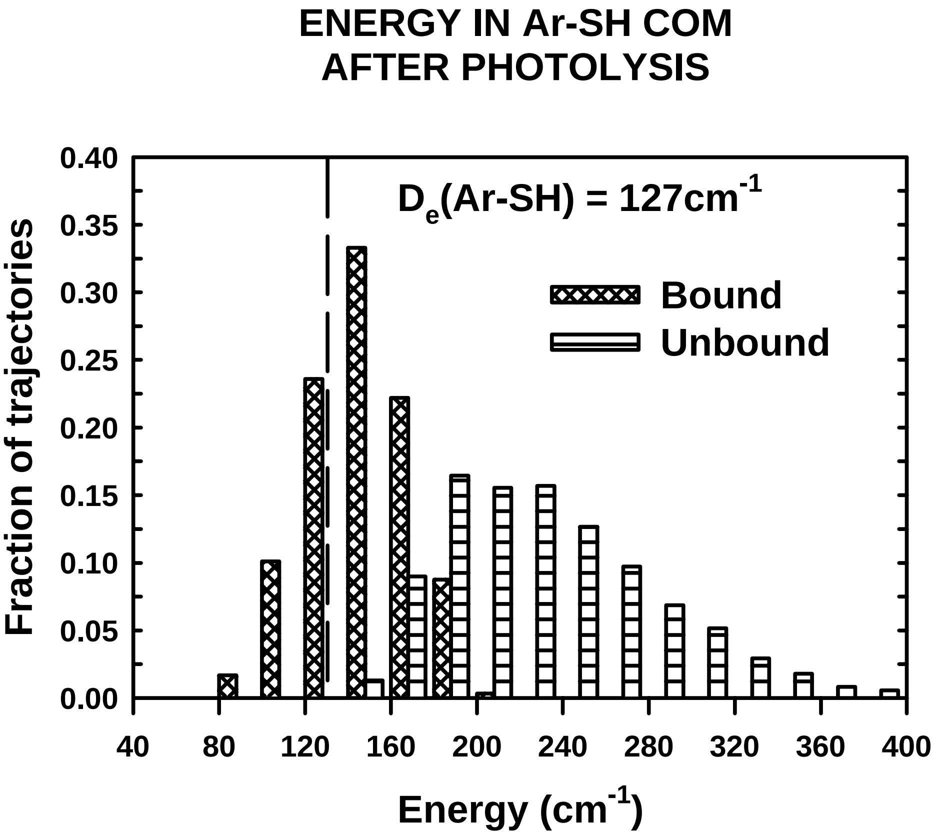

Figure 3.5. Histogram of the energy remaining in 5000 Ar-SH clusters after photolysis, separated into bound and unbound at the end of 1 ns. The line at 127 cm^{-1} denotes the dissociation energy (D_e) of the Ar-SH. Notably, half of the bound clusters at the end of this calculation have $E > D_e$.

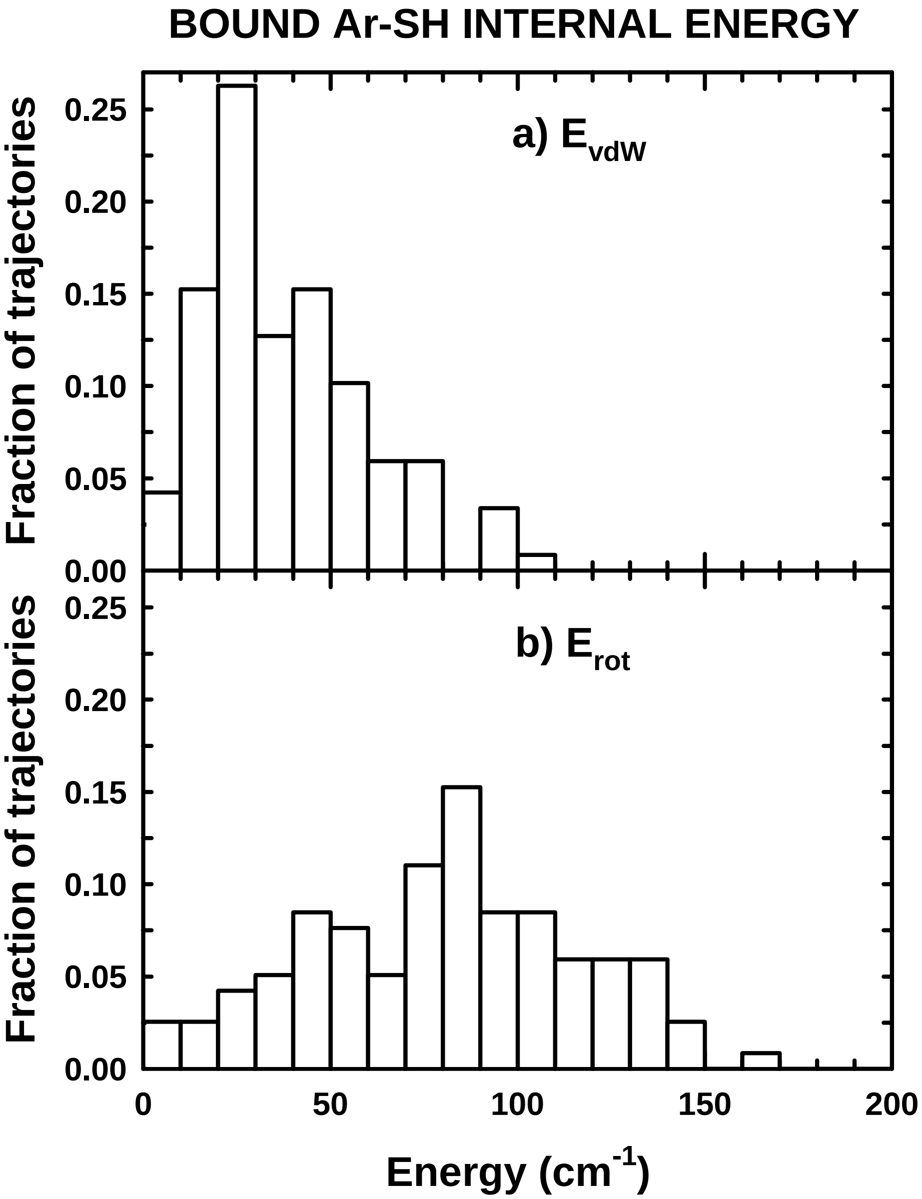

Figure 3.6. Histograms of the energy partitioning between a) E_{vdW}, van-der-Waals-stretch vibrational modes and b) E_{rot}, end-over-end rotational of the Ar-SH cluster. While the vibrational energy distribution tails off at the dissociation limit (D_e = 127 cm^{-1}), the rotational energy distribution clearly exceeds this limit.

convergence of the cluster calculations (Fig. 3.4c) indicates that relatively few, if any, of the clusters remaining bound at 1 ns will ultimate fall apart. The quasibound clusters must therefore be subject to a *dynamical* constraint preventing intracluster rotational-to-vibrational energy transfer; this possibility is explored in the next section.

3.3.3 Dynamics of radical cluster formation

As noted above, the "quasibound" clusters, i.e., those with $E > D_e$ that remain bound at the end of the 1-ns calculation, can contain energy above the dissociation limit as long as that energy is trapped in rotation. Since this must correlate to high angular momentum states, we next look at the angular momentum distributions for both energetically bound and quasibound trajectories.

Figure 3.7 contains a histogram representing the total radical-cluster angular momenta for bound Ar-SH clusters from 248-nm photolysis. A clear distinction between the energetically bound and quasibound distributions exists: the center of the angular momenta of quasibound clusters, near $40\hbar$, is shifted approximately $10\hbar$ higher than that of energetically bound clusters. Importantly, the center of each distribution exceeds the average pre-photolysis angular momentum (from the initial condition sampling) by $> 20\hbar$; thus, most of the angular momentum observed in these bound clusters is generated by photolysis. In addition, it represents an unusually hot distribution of clusters: for a peak value of $J = 40\hbar$, the rotational temperature would be greater than 300 K, much higher than temperatures typically available by coexpanding rare-gas atoms with pre-generated radicals. Correspondingly, we might

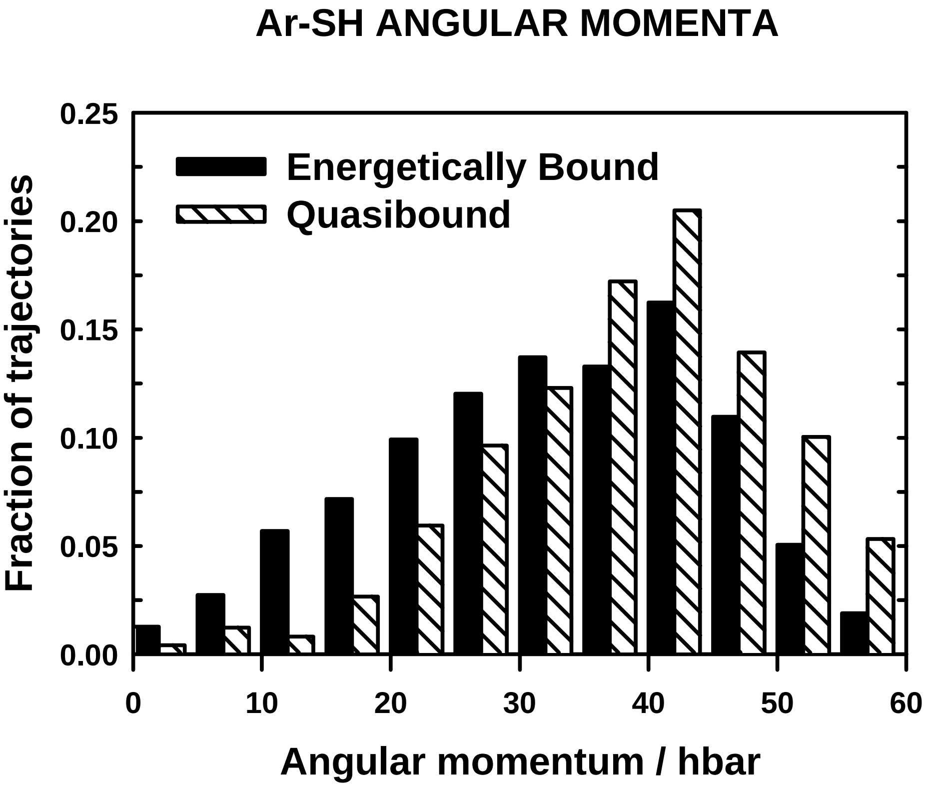

Figure 3.7. Distribution of total radical-cluster angular momenta for bound Ar-SH clusters from 248 nm photolysis, partitioned into energetically bound ($E < D_e$) and quasibound ($E > D_e$). The center of the angular momenta of quasibound clusters is approximately $10\hbar$ higher than that of energetically bound clusters; both have rotational temperature ≥ 300 K.

expect these high angular momentum states to constrain cluster dynamics in a way not typically observed in jet expansions.

Such a constraint can be shown to exist for diatomic molecules, in which incorporating the kinetic energy from orbital angular momentum (L) into an effective potential, $V_L^{eff}(R) = V(R) + L^2/(2\mu R^2)$, can produce a barrier at a given value of $R = R^*$. Any trajectory with total energy less than $V_L^{eff}(R^*)$ and $R < R^*$, will remain classically bound, regardless of whether its total energy exceeds the dissociation limit of the diatomic. Indeed, Garcia-Vela has demonstrated that such a barrier can prevent Ar-Cl dissociation subsequent to Ar-HCl photolysis.[36] For the triatomic Ar-SH, since the SH bond distance is smaller than the Ar-SH distance and the H atom is much lighter than the S, we might anticipate behavior similar to that of a pseudodiatomic. Thus, we next explore the possibility that the quasibound trajectories are held bound by an angular momentum barrier.

First, we must determine how to calculate such a barrier for the triatomic Ar-SH complex. In the diatomic case, $V_L^{eff}(R)$ is obtained by invoking the orbital angular momentum as a constant of the motion; in the triatomic case, the total angular momentum (J) is instead conserved. Pollack has shown that for triatomics, an effective potential can be written which may contain a rigorous barrier to dissociation;[49] for Ar-SH, this effective potential can be written as

$$V_J^{eff}(R, r_, \theta) = V(R, r, \theta) + J^2/2I,$$

$$I = m_{Ar}m_{SH}/m_{Ar\text{-}SH}\, R^2 + m_S m_H/m_{SH}\, r^2 \qquad (3.10)$$

where R is the distance between the Ar and the center of mass of SH, r is the SH bond distance, θ is the angle between these two vectors, and J is the total angular momentum.

Finding the total angular momentum barrier, defined as $E_{barrier}$, requires two steps. First, V_J^{eff} is minimized as a function of (r, θ) at parametric values of R, producing $V_J^{eff}(R)$. Second, $E_{barrier}$ is determined by maximizing $V_J^{eff}(R)$ for R outside the well region, i.e., $E_{barrier} \equiv V_J^{eff}(R^*)$, where $R = R^*$ is the location of this maximum. Operationally, since the minima in $V_J^{eff}(R)$ should occur near the equilibrium value of r (see Table 3.1) and $\theta = 0°$, we set $V_J^{eff}(R) = V_J^{eff}(R, r = r_{eq}\ \theta = 0^o)$, then find $E_{barrier}$ from this potential. As in the diatomic case, if photolysis generates an Ar-SH cluster with $R < R^*$ and total energy less than $E_{barrier}$, it will remain classically bound. Importantly, the V_J^{eff} obtained in this fashion produces a minimum barrier, which corresponds to all angular momentum lying in end-over-end tumbling of Ar-SH; when SH angular momentum is nonzero, the width of the barrier is larger.

To estimate the barrier height for trajectories in our calculations, we have calculated $V_J^{eff}(R)$ for several representative values of J; these effective potentials are plotted in Fig. 3.8. Notably, while $E_{barrier}$ is only on the order of a few wavenumbers for the lowest angular momentum ($20\hbar$), it rises nearly to 100 cm^{-1} for an angular momentum of $60\hbar$. Clearly, the angular momenta sampled by the Ar-SH clusters, as seen in Fig. 3.7, provide barriers sufficient to accommodate energies far above the dissociation limit. Accordingly, we expect to find a significant number of photolysis

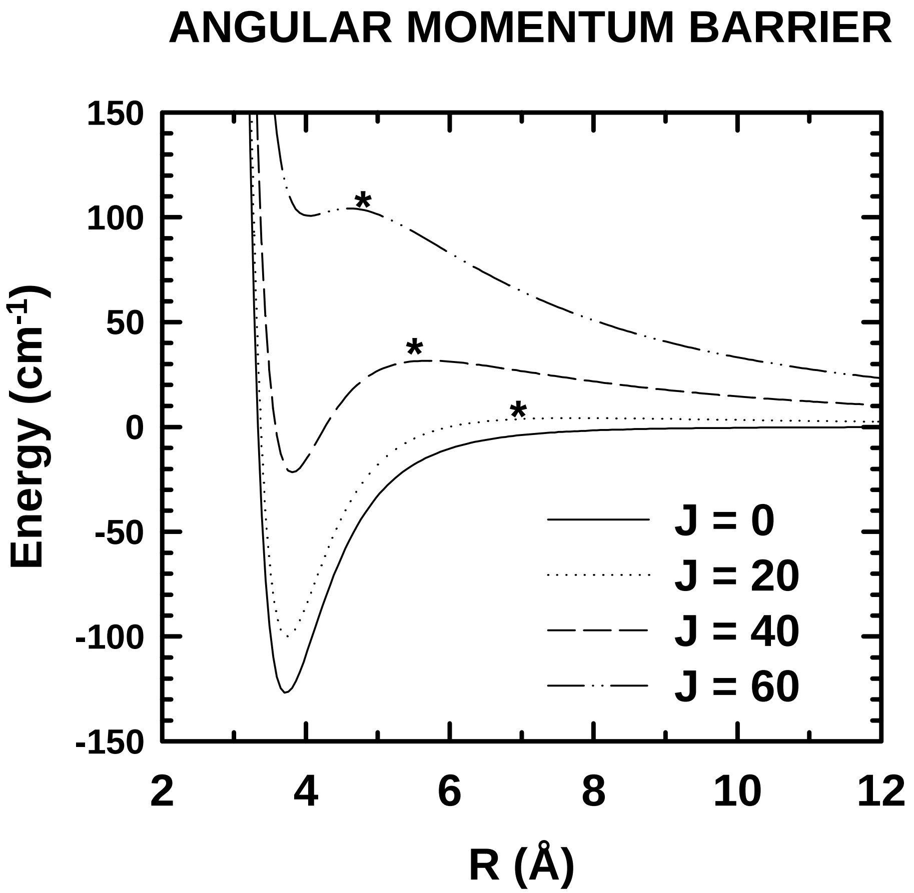

Figure 3.8. Effective potential, V_J^{eff}, for several representative values of J as a function of R, with r fixed to its equilibrium value (see Eqn. 10). The asterisks designate R= R*, i.e., the location of the effective angular momentum barrier. This barrier rises nearly to 100 cm^{-1} for an angular momentum of 60$\hbar$.

trajectories with E > D_e but less than $E_{barrier}$. Any such dynamically bound trajectories will be designated as “quasibound.”

To determine which trajectories are quasibound, we return to those shown in Fig. 3.4. These trajectories are separated into three categories (energetically bound, quasibound, and unbound) by calculating the total internal energy and comparing to $E_{barrier}$, which is in turn obtained from maximizing Eqn. 3.10 with respect to R for each trajectory. We find that for photolysis of Ar-H_2S at 248 nm, nearly *all* the trajectories with E > D_e that survive to 1-ns (i.e., quasibound trajectories) have $E < E_{barrier}$ and are thus dynamically bound. Thus, we can conclude that the angular momentum barrier plays a significant role in the classical dynamics of cluster formation.

The question remains, however, whether such high rotational states will live for sufficient time to be experimentally detected. From a quantum-mechanical perspective, the finite height of the angular momentum barrier provides a finite probability of tunneling, although tunneling might seem unlikely for a system involving heavy Ar and S masses. We follow the general procedure of Child[50] to obtain a JWKB estimate of the tunneling lifetime, τ:

$$\tau = \frac{\pi}{\omega}\left(\frac{[\kappa^2(1+\kappa^2)]^{1/4}}{(1+\kappa^2)^{1/2}-\kappa}\right) \qquad 3.11$$

where

$$\kappa = \exp\left[-\int_b^c \mathrm{k(R)dR}\right]$$

$$\mathrm{k(R)} = \left\{2\mu_{\text{Ar-SH}}\left[\mathrm{E} - \mathrm{V(Ar\text{-}SH)}\right]\right\}^{1/2} / \hbar\ ,$$

ω is the classical attempt frequency, and b,c are inner and outer points, respectively, in R at which $V_J^{eff} = E_{tot}$. We set ω at 40 cm^{-1}, which is approximately the vibrational frequency of Ar-SH.[24] This tunneling lifetime can then be compared to the experimental delay between the photolysis and probe pulses (typically 100 ns) to estimate how many quasibound clusters would fall apart before being detected.

Figure 3.9 contains the tunneling lifetimes calculated for quasibound clusters resulting from photolysis of Ar-H_2S at 248 nm. These lifetimes are plotted as a function of $\Delta E/E_{barrier}$, where ΔE is the energy above the dissociation limit such that as $\Delta E/E_{barrier} \rightarrow 0$, the total energy decreases toward the dissociation limit. X's represent Ar-SH clusters whose tunneling lifetimes are shorter than 100 ns (i.e., tunneling on a timescale shorter than the photolysis-probe delay), and o's represent clusters whose tunneling lifetimes are greater than that delay. Not surprisingly, the shortest tunneling lifetimes are clustered near $\Delta E/E_{barrier} \rightarrow 1$, i.e., when the total internal energy of the cluster approaches the barrier height. Intriguingly, tunneling lifetimes shorter than the 100-ns experimental timescale represent approximately *half* of the quasibound clusters; from this initial estimate, we would expect that nearly half thus fall apart prior to detection.

As discussed above, angular momentum of the SH subunit increases the width of the barrier "seen" by the molecule thus drastically increasing the tunneling lifetime of a given cluster. Accordingly, we would expect fewer clusters to tunnel than indicated by this 1D estimate. Nevertheless, this effect opens the possibility that tunneling may contribute to the dramatic cluster cooling observed experimentally as the photolysis-probe delay increases up to 10 μs. However, since our calculations

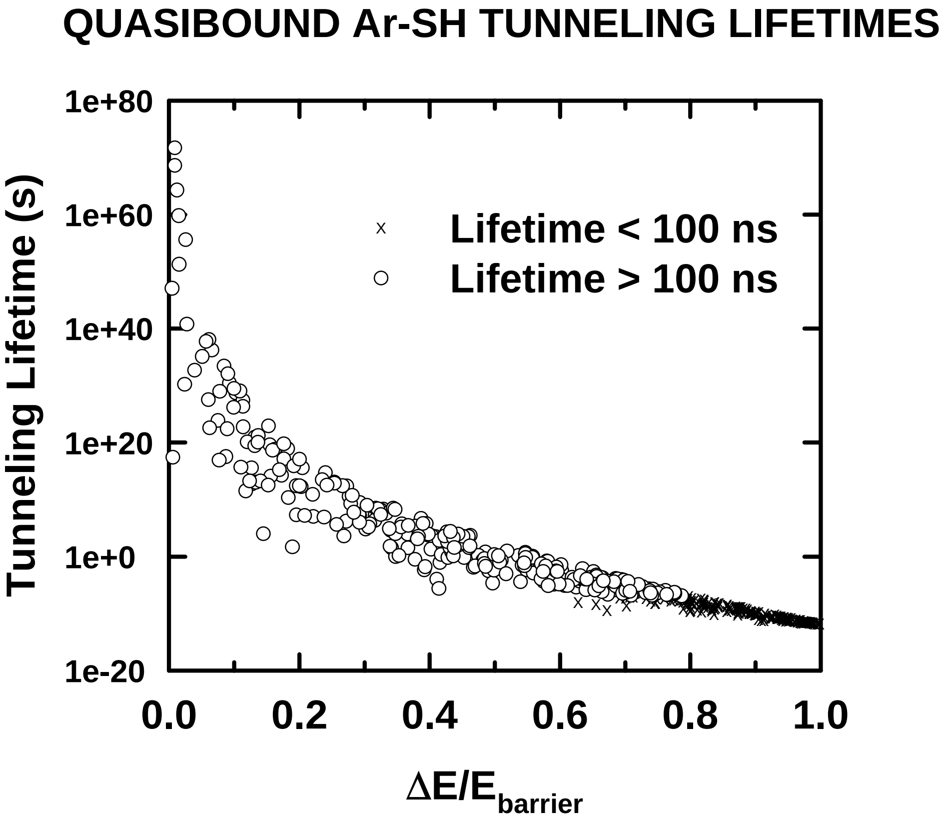

Figure 3.9. Tunneling lifetimes of quasibound clusters versus $\Delta E/E_{barrier}$ from photolysis of Ar-H_2S at 248 nm, where ΔE is the energy in the cluster above the dissociation limit and $E_{barrier}$ is the barrier height. The x's represent lifetimes shorter than 100 ns (the photolysis-probe delay), and o's represent lifetimes greater than that delay. While trajectories with tunneling lifetimes less than 100 ns are clustered near $\Delta E/E_{barrier} \rightarrow 1$, these represent approximately half of these quasibound trajectories.

confirm a significant population of clusters with $E < D_e$ (i.e., which cannot undergo quantum mechanical tunneling), loss of the hottest clusters by tunneling is not the only source of the observed cooling. In addition, the large dynamic range observed in the tunneling lifetimes (from one vibrational period to billions of years) indicates that few clusters will fall apart in the range of experimental delays (<10% of the trajectories in Fig. 3.9 have lifetimes in the 100-ns to 10-μs). Thus, while tunneling may contribute to an overall loss of signal in comparison with classical predictions, it is not likely to be the source of the dramatic cooling on the experimental timescale.

3.3.4 Efficiency and mechanisms of cluster formation: comparison with experiment

With an understanding of the energetics and dynamics of radical cluster formation, we have a basis for predicting the relative contributions of various photolysis mechanisms to the experimental spectra. For this purpose, we summarize the branching ratios between photolysis products in Table 3.2. These branching ratios include all classically bound clusters (i.e., energetically bound and quasibound), since the number of clusters predicted to tunnel cannot be precisely determined (as discussed in the previous section). The frequency of bound versus unbound trajectories can be estimated from relative populations in calculations given in Fig. 3.4. However, some calculations had either not converged by the end of the calculation or had not produced measurable products.

To aid in determining branching ratios among the photolysis products, we thus perform additional calculations on systems nonconverged results. We first focus on Ar-H_2S, for which we can calculate the internal energy and angular momentum of the

Table 3.2. Calculated product branching ratios for Ar-H_2S and Ar_2-H_2S photolysis at 193 nm and 248 nm.

		Product distribution, %			
		Ar-SH			Ar_2-SH
$\lambda_{photolysis}$ (nm)	Precursor	**Total**	$E < D_e$	$D_e < E < E_{barrier}$	**Total**
193	Ar-H_2S	**0.06(2)**[a]	0	0.06(2)	
	Ar_2-H_2S	**17(2)**	12(2)	4(1)	**0**
248	Ar-H_2S	**24(2)**	13(2)	11(1)	
	Ar_2-H_2S	**51(3)**	50(3)	0.8(4)	**0.8(4)**

a) Numbers in parentheses represent 2σ.

cluster as soon as the H atom flies off and thus obtain branching ratios among bound, quasibound, and unbound clusters. Calculations at both wavelengths converged in the original 1-ns timescale, but no Ar-SH product was observed at 193 nm. Thus, we have calculated an additional 20,000 trajectories at 193 nm, halting the trajectories after H-atom flyoff and determining if any radical clusters will survive. Out of these, none are energetically bound, but 11/20,000 are quasibound.

For Ar_2-H_2S, we can also use the understanding of cluster energetics and dynamics to explore the photolysis in more detail, although the picture is not quite as simple, i.e., the classical fate of the cluster is not necessarily determined after H atom flyoff. If the total internal energy of the cluster is less than the dissociation energy for either Ar-Ar or Ar-SH, then we expect Ar_2-SH to remain classically bound. This allows interrogation of the Ar_2-H_2S trajectories at 248 and 193 nm to determine if any form bound Ar_2-SH. For 248-nm photolysis, 4/500 have energy below the barrier to boiling off any subunit and thus form Ar_2-SH, while none out of 5500 at 193 nm do. The remaining clusters contain sufficient energy to boil off one or more of the subunits (Ar *or* SH), with SH boil-off resulting in an unbound cluster and Ar boil-off in a bound, quasibound, or unbound Ar-SH cluster. Since prior to the boil off of a subunit, the fate of the cluster cannot be determined, the calculation must continue until one subunit escapes.

While cluster concentrations from the 193-nm Ar_2-H_2S trajectories level off during the timescale of the original calculation, the 248-nm trajectories do not. Correspondingly, we propagate forward those 248-nm trajectories still containing Ar_2-SH at the end of the previous 250-ps calculation for an additional decade of time, i.e., 2.5 ns. Based on the observation of a ~25% drop in concentration in each decade of time (see Fig. 3.4), we might expect an additional ~25% loss during this extended calculation. Instead, the dissociation rate decreases such that only an additional ~11% fall apart (i.e., approximately 25% remain after 2.5 ns). This decreased rate may imply that some ultimately unbound clusters will survive long enough to be probed; however, the binding energy of the Ar-OH potential used is larger than the binding energy of Ar-SH, and our estimates represent an upper limit to the dissociation lifetimes that would be observed experimentally.

More important for our branching ratio estimates, *all* of these clusters boil off an Ar to form Ar-SH. We thus anticipate all of the remaining trajectories in this group (i.e., those which still contain Ar_2-SH after 2.5 ns) will ultimately fall apart to

Ar + Ar-SH, rather than Ar_2 + SH or Ar + Ar + SH. Accordingly, we have estimated the net product branching ratios in Table 3.2 based on this assumption.

This estimate thus completes the branching ratios in Table 3.2, providing the basis for elucidating the dominant cluster formation mechanisms as well as for comparing with experimental results. By measuring relative Ar-SH/Ar_2-SH signals as a function of reciprocal argon concentration, the relative importance of the various photolysis channels were experimentally determined at both photolysis wavelengths. The key results are highlighted below and discussed in the context of the trajectory calculations.

First of all, even at the highest photolysis energy, some fraction of the Ar-SH species observed experimentally resulted from Ar-H_2S photolysis, i.e., from a nonfragmentary pathway. This result is supported by our trajectory calculations, with a nearly 20% survival rate of Ar-SH from Ar-H_2S at 248 nm and a small but nonzero survival rate at 193 nm. Incidentally, *all* of the 193-nm clusters are *quasibound* (i.e., with $D_e < E < E_{barrier}$), compared to half of the 248-nm trajectories. This must result from accommodation of a much larger excess photolysis energy, producing hotter clusters. Also notable is the efficiency of the "boil-off" mechanism for Ar-SH production from Ar_2-H_2S; 17% and 51% of Ar_2-H_2S precursors follow that path at 193 nm and 248 nm, respectively. In each of these cases, fewer Ar-SH clusters are quasibound than bound, presumably because the extra Ar atom typically carries away sufficient energy so that the remaining cluster contains $E < D_e$.

In contrast to the importance of the nonfragmentary pathways for Ar-H_2S, nonfragmentary photolysis of Ar_2-H_2S (i.e., producing Ar_2-SH) is not a major channel at either wavelength. At first, this might seem surprising: given a particular amount of energy to accommodate, Ar_2-SH has more modes of motion for energy disposal than Ar-SH. However, while additional modes may *delay* dissociation, the excess energy can eventually build up in a particular mode and lead to boil off of one subunit. In addition, if H_2S dissociation were strictly uncoupled from interactions with the Ar atom(s), less kinetic energy would be "lost" by transforming the velocity of the dissociating SH into the COM frame of the radical cluster with two Ar atoms present than with one Ar present. In this limit, an Ar_2-SH cluster must accommodate more energy than Ar-SH; thus, the boil-off mechanism dominates.

The relative importance of photolysis mechanisms in the trajectory calculations leads us to two addition points of comparison with experiment. First, experimental evidence showed that at 193 nm, fragmentary photolysis of Ar_2-H_2S is more dominant over nonfragmentary photolysis than at 248 nm. In other words, an Ar_2-SH cluster is more likely to boil off an atom at the higher photolysis energy, consistent with the greater excess energy generated at 193 nm. This observation agrees with our calculations, which yield no Ar_2-SH product from 193-nm photolysis of Ar_2-H_2S; however, we cannot predict whether additional trajectories would produce any such product and thus cannot exactly determine the relative importance of these pathways. Second, the experiments showed that the probability of nonfragmentary photolysis of both Ar_2-H_2S and Ar-H_2S decreases with photolysis energy, but that nonfragmentary photolysis of Ar_2-H_2S decreases more slowly than Ar-H_2S. Clearly, while the calculations agree that nonfragmentary photolysis decreases as a function of collision energy for both precursor clusters, the second point cannot be addressed without any Ar_2-SH product from 193-nm photolysis of Ar_2-H_2S.

Having explored the dynamics of the Ar_n-H_2S photolysis system, we now expand our focus to investigate more generally the feasibility of radical cluster formation from photolysis of closed-shell precursors. To that end, we work through the simple ballistic model proposed previously[39] to estimate the energetics of radical cluster formation, focusing on precursors containing clusters of H_2S/H_2O (designated H_2X) with a single additional subunit, typically a rare gas (designated Rg).

In this model, the first assumption is that the H_2X is uncoupled from interactions with the accompanying subunit during the photolysis step. Consequently, by conservation of momentum, the departing H atom must carry away most of the excess energy from the photolysis, leaving the following in XH translational energy:

$$T_{XH} = \frac{m_{XH} \cdot v_{XH}^2}{2} = \frac{h\nu - D_0(\text{HX–H})}{(1 + m_{XH}/m_H)} \qquad (3.12)$$

For H_2S, this reduces the photolysis energy imparted to the SH by ~34-fold from the excess photolysis energy; for H_2O, by ~17-fold. The recoil energy of the XH is further reduced by transformation into the COM frame of the remaining radical cluster, with a *larger* reduction for *lighter* collision partners:

$$E_{Rg-XH} = \frac{\mu_{Rg-XH} \cdot v_{XH}^2}{2} = \frac{\mu_{Rg-XH}}{m_{XH}} \cdot \frac{h\nu - D_0(\text{HX} - \text{H})}{(1 + m_{XH}/m_H)} \qquad (3.13)$$

Eqn. 3.13 thus represents an upper limit on the COM energy imparted to the radical cluster by photolysis of the monomer.

Using Eqn. 3.13, we calculate this COM cluster energy for photolysis of H_2O and H_2S with a variety of cluster partners, plotted in Fig. 3.10 as a function of collision partner mass. The photolysis wavelengths represented are 193 nm and 248 nm for H_2S, and 193 nm for H_2O; for comparison, the experimental dissociation energies of the radical clusters are also shown. Several interesting trends can be seen in this figure. First of all, decreasing the mass of the collision partner does indeed decrease the COM energy. However, a similar trend is observed in the binding energies of the radical clusters, so simply reducing the mass of the collision partner would not ensure an increased probability of radical cluster formation. Second, the photolysis products of H_2S and H_2O at 193 nm nearly overlap on this chart. This results from two competing effects: the lighter mass of O versus S causes the H atom to carry away less energy, but the H-OH bond is stronger than the H-SH bond, leaving less excess energy from the photolysis within the cluster.

Third, and most importantly, it is clearly feasible to produce bound open-shell clusters even when the COM energy estimated by this ballistic model is larger than D_0. Indeed, even though E_{COM} for Ar-H_2S photolysis at 193 nm is nearly fourfold larger than the binding of Ar-SH, free-radical clusters are observed both experimentally and theoretically. This raises the possibility that *any* of the clusters found in Fig. 3.10 might be formed via photolysis of the closed-shell precursor.

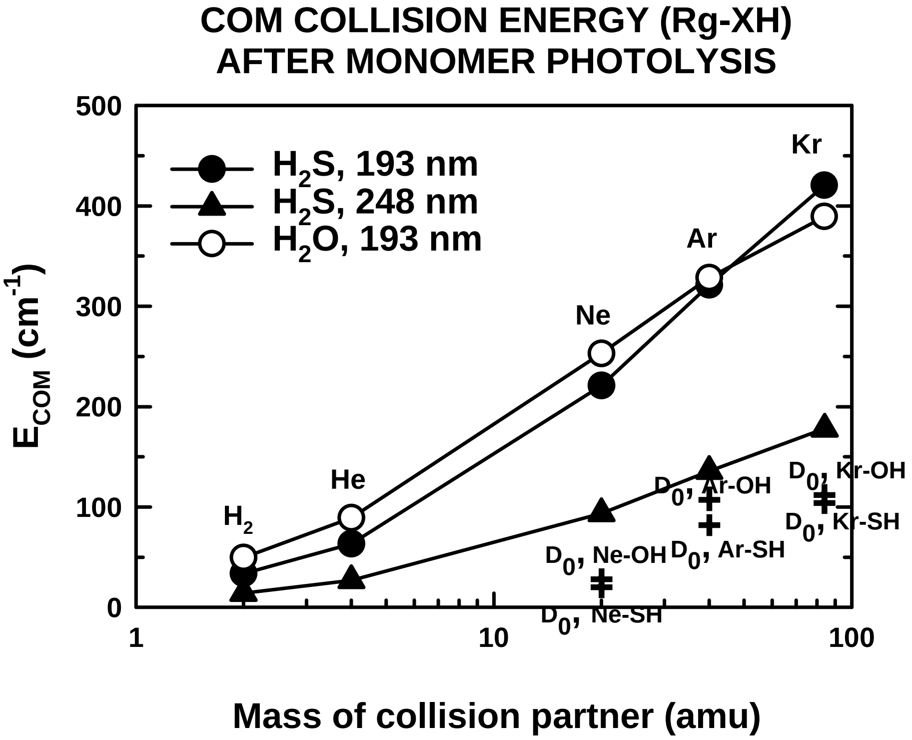

Figure 3.10. COM cluster energy versus collision partner mass for photolysis of H_2O and H_2S clustered with a single collision partner (calculated from Eqn. 3.13). Superimposed are the dissociation energies for appropriate rare-gas/radical clusters (denoted with a + and labeled). These calculations assume no potential-energy interaction between the collision partner and radical during the photolysis process and thus represent an upper limit to the COM energy.

3.5 Conclusions

We have carried out quasiclassical trajectory calculations for the photolysis of Ar-H_2S and Ar_2-H_2S at 193 nm and 248 nm. These calculations serve as a basis for comparison to our earlier experiments on photolysis of these clusters in a supersonic jet expansion, in which we observed a remarkable efficiency for formation of the radical cluster species Ar-SH and Ar_2-SH from photolysis of the closed-shell precursors.

First, the quasiclassical photolysis calculations confirm the overall efficiency of radical cluster formation. Indeed, for photolysis of Ar-H_2S at 248 nm, roughly 20% of the precursors form bound Ar-SH clusters. Even at the shorter photolysis wavelength of 193 nm, the fragmentary photolysis of Ar_2-H_2S forms Ar-SH clusters with roughly 20% efficiency. The timescales on which unbound radical clusters fall apart are typically much shorter than the experimental timescale, ranging from ~5 ps for 193 nm photolysis of Ar-H_2S to ~10 ns for 248 nm photolysis of Ar_2-H_2S. The remarkable efficiency of radical cluster formation results in part from the fact that the relatively light H atom, by conservation of momentum, carries away the majority of the excess photolysis energy in kinetic energy.

However, the calculations confirm that the clusters retain sufficient energy in their COM frame for significant intracluster rovibrational excitation. The energy found in these clusters is primarily partitioned between relative rotation and vibration of the Ar and SH subunits. Ar-SH vibrational states up to the dissociation limit are populated, indicating that the photolysis process yields bound clusters that sample significant regions of the potential energy surface. In addition, rotational energies up to and *beyond* the dissociation limit are found in bound clusters, pointing to the existence of an angular momentum barrier to dissociation. Indeed, nearly half of the bound Ar-SH clusters from photolysis of Ar-H_2S at 248 nm, and all of the bound Ar-SH from photolysis at 193 nm, contain total energy greater than the dissociation limit. However, that energy, trapped in rotation, is unavailable for transfer into vibration; thus, the clusters are classically bound. Quantum mechanical tunneling calculations indicate that as an upper limit, roughly half of these quasibound clusters may fall apart prior to probing on the experimental timescale (i.e., 100-ns delay between photolysis and probe pulses).

These calculations provide a basis for comparing the relative efficiencies of two radical-cluster formation mechanisms: nonfragmentary (in which no Ar atoms are lost) versus “boil off” (in which one Ar atom carries away the excess energy). Overall, the nonfragmentary production of Ar-SH from photolysis of Ar-H_2S is demonstrated to be remarkably efficient at the longest photolysis wavelength (248 nm), while the “boil off” mechanism produces a large fraction of bound Ar-SH clusters ($\approx$ 20%) from Ar_2-H_2S, even at the shortest wavelength (193 nm). Finally, the overall efficiency of this method for bound closed-shell cluster production from Ar_n-H_2S photolysis provides evidence that this technique could be extended to bound clusters of other hydrides (e.g., H_2O) and clustering species (e.g., H_2, Kr, Ne).

References for Chapter 3

1. M. I. Lester, C.-C. Chuang, P. M. Andrews, M. Yang, and M. H. Alexander, *Faraday Discuss.* **102,** 311 (1996).

2. W. M. Fawzy and M. C. Heaven, *J. Chem. Phys.* **89,** 7030 (1988).

3. W. M. Fawzy and M. C. Heaven, *J. Chem. Phys.* **92,** 909 (1990).

4. S. K. Bramble and P. A. Hamilton, *Chem. Phys. Lett.* **170,** 107 (1990).

5. M. T. Berry, M. R. Brustein, and M. I. Lester, *Chem. Phys. Lett.* **153,** 17 (1988).

6. M. T. Berry, M. R. Brustein, J. R. Adamo, and M. I. Lester, *J. Phys. Chem.* **92,** 5551 (1988).

7. M. T. Berry, M. R. Brustein, and M. I. Lester, *J. Chem. Phys.* **90,** 5878 (1989).

8. M. T. Berry, M. R. Brustein, and M. I. Lester, *J. Chem. Phys.* **92,** 6469 (1990).

9. M. I. Lester, *NATO ASI Ser., Ser. B* **227,** 143 (1990).

10. M. I. Lester, R. W. Randall, L. C. Giancarlo, and S. E. Choi, *J. Chem. Phys.* **99,** 6211 (1993).

11. M. I. Lester, R. A. Loomis, L. C. Giancarlo, M. T. Berry, C. Chakravarty, and D. C. Clary, *J. Chem. Phys.* **98,** 9320 (1993).

12. M. I. Lester, S. E. Choi, L. C. Giancarlo, and R. W. Randall, *Faraday Discuss.* **97,** 365 (1994).

13. M. I. Lester, W. H. J. Green, C. Chakravarty, and D. C. Clary, *Adv. Ser. Phys. Chem.* **4,** 659 (1995).

14. P. P. Korambath, X. T. Wu, and E. F. Hayes, *J. Chem. Phys.* **107,** 3460 (1997).

15. B. C. Chang, L. Yu, D. Cullin, B. Rehfuss, J. Williamson, T. A. Miller, W. M. Fawzy, X. Zheng, S. Fei, and M. Heaven, *J. Chem. Phys.* **95,** 7086 (1991).

16. B. C. Chang, J. M. Williamson, D. W. Cullin, J. R. Dunlop, and T. A. Miller, *J. Chem. Phys.* **97,** 7999 (1992).

17. B. C. Chang, D. W. Cullin, J. M. Williamson, J. R. Dunlop, B. D. Rehfuss, and T. A. Miller, *J. Chem. Phys.* **96,** 3476 (1992).

18. B.-C. Chang, J. R. Dunlop, J. M. Williamson, T. A. Miller, and M. C. Heaven, *Chem. Phys. Lett.* **207,** 62 (1993).

19. B.-C. Chang, J. R. Dunlop, and T. A. Miller, *Chem. Phys. Lett.* **207,** 55 (1993).

20. B.-C. Chang, J. R. Dunlop, J. M. Williamson, and T. A. Miller, *J. Opt. Soc. Am. B* **11,** 198 (1994).

21. C. C. Carter, T. A. Miller, H.-S. Lee, P. P. Korambath, A. B. McCoy, and E. F. Hayes, *J. Chem. Phys.* **110,** 1508 (1999).

22. T.-S. Ho, H. Rabitz, S. E. Choi, and M. I. Lester, *J. Chem. Phys.* **102,** 2282 (1995).

23. M. C. Yang, A. P. Salzberg, B. C. Chang, C. C. Carter, and T. A. Miller, *J. Chem. Phys.* **98,** 4301 (1993).

24. M.-C. Yang, C. C. Carter, and T. A. Miller, *J. Chem. Phys.* **107,** 3437 (1997).

25. C. C. Carter and T. A. Miller, *J. Chem. Phys.* **107,** 3447 (1997).

26. P. P. Korambath, X. T. Wu, E. F. Hayes, C. C. Carter, and T. A. Miller, *J. Chem. Phys.* **107,** 3460 (1997).

27. C. C. Carter, T. A. Miller, H.-S. Lee, A. B. McCoy, and E. F. Hayes, *J. Chem. Phys.* **110,** 5065 (1999).

28. M.-C. Yang, C. C. Carter, and T. A. Miller, *J. Chem. Phys.* **110,** 7305 (1999).

29. R. A. Loomis and M. I. Lester, *J. Chem. Phys.* **103,** 4371 (1995).

30. R. A. Loomis, R. L. Schwartz, and M. I. Lester, *J. Chem. Phys.* **104,** 6984 (1996).

31. R. A. Loomis and M. I. Lester, *Annu. Rev. Phys. Chem.* **48,** 643 (1997).

32. M. T. Berry, R. A. Loomis, L. C. Giancarlo, and M. I. Lester, *J. Chem. Phys.* **96,** 7890 (1992).

33. C.-C. Chuang, P. M. Andrews, and M. I. Lester, *J. Chem. Phys.* **103,** 3418 (1995).

34. C. Jacques, L. Valachovic, S. Ionov, E. Bohmer, Y. Wen, J. Segall, and C. Wittig, *J. Chem. Soc. Faraday Trans.* **89,** 1419 (1993).

35. T. Suzuki, H. Katayanagi, and M. C. Heaven, *J. Phys. Chem. A* **101,** 6697 (1997).

36. A. Garcia-Vela, *J. Chem. Phys.* **108,** 5755 (1998).

37. J. C. Juanes-Marcos and A. Garcia-Vela, *J. Chem. Phys.* **111,** 2606 (1999).

38. K. M. Christoffel and J. M. Bowman, *J. Chem. Phys.* **104,** 8348 (1996).

39. S. R. Mackenzie, O. Votava, J. R. Fair, and D. J. Nesbitt, *J. Chem. Phys.* **105,** 11360 (1996).

40. S. R. Mackenzie, O. Votava, J. R. Fair, and D. J. Nesbitt, *J. Chem. Phys.* **110,** 5149 (1999).

41. R. C. Cohen and R. J. Saykally, *J. Chem. Phys.* **98,** 6007 (1993).

42. R. A. Aziz and H. H. Chen, *J. Chem. Phys.* **67,** 5719 (1977).

43. G. Theodorakopoulos and I. D. Petsalakis, *Chem. Phys. Lett.* **178,** 475 (1991).

44. G. Theodorakopoulos, I. D. Petsalakis, and C. A. Nicolaides, *Chem. Phys. Lett.* **207,** 321 (1993).

45. D. A. Ramsay, *J. Chem. Phys.* **20,** 1920 (1952).

46. K. T. Tang and J. P. Toennies, *Chem. Phys.* **156,** 413 (1991).

47. R. C. Cohen and R. J. Saykally, *J. Phys. Chem.* **94,** 7991 (1990).

48. NAG Fortran Library (Oxford University: Oxford, 1997)

49. E. Pollak, *J. Chem. Phys.* **86,** 1645 (1987).

50. M. S. Child, *Semiclassical Mechanics with Molecular Applications* (Clarendon Press, Oxford, 1991).

CHAPTER 4

DYNAMICS OF COLLISIONAL ALIGNMENT IN SUPERSONIC EXPANSIONS: TRAJECTORY STUDIES OF HE + CO, O_2 AND CO_2

4.1 Introduction

Probing and ultimately controlling the dynamics of chemical reactions at the quantum state-to-state level has long been a goal of chemical physics research. At the highest level of detail, studies of bimolecular reaction dynamics would permit the stereochemistry to be manipulated, influencing what region of the potential surface is sampled as the reagent molecules approach and collide. One key step in this overall scheme is to orient or align the colliding molecules with respect to some lab-/body-fixed axis frame, either by static (DC) fields, optical (AC) fields, or simply directed collisions in an anisotropic flow.[1] Depending on the efficiency of these processes, such techniques ultimately offer the opportunity to probe the detailed topology of a reactive potential energy surface, or, in other words, the "steric effect" in a chemical reaction.

This general area of molecular control of stereodynamics has witnessed enormous growth over the past 30 years, primarily exploiting alignment and/or orientation of rotational angular momentum states in external fields. Mathematically, orientation and alignment refer to ordered moments of the m_j distribution (the z-axis projection of **j**). Oriented samples correspond to $<m_j> \neq 0$, with the lowest order quantum-mechanical orientation given by[2]

$$O_0^{(1)} = <\left\langle jm_j \middle| j_z \middle| jm_j \right\rangle> \Big/ \sqrt{j(j+1)} \qquad (4.1)$$

where the outer brackets represent an average over the m_j distribution. Alternatively, aligned samples can have $<m_j> = 0$ but require a non-uniform distribution in $|m_j|$, with a lowest order alignment given by

$$A_0^{(2)} = <\left\langle jm_j \middle| 3j_z^2 - \boldsymbol{j}^2 \middle| jm_j \right\rangle> \Big/ \sqrt{j(j+1)} \qquad (4.2)$$

In the classical limit, this orientation and alignment can be related to the first and second Legendre moments, respectively, of the corresponding angular distribution of **j**. For collision systems symmetric with respect to the relative velocity vector (i.e., in the absence of any external fields), the final m_j and $-m_j$ populations are exactly equal, which precludes any orientation effects. However, the distributions in $|m_j|$ can be non-uniform and therefore result in finite rotational alignment. In general, a distribution with an excess of **j** states parallel or perpendicular to the alignment axis corresponds to $A_0^{(2)} > 0$ or $A_0^{(2)} < 0$, respectively.

The use of angular momentum quantum states to influence or control bimolecular collision geometries was originally developed by the Bernstein[3] and

Brooks[4] groups. In these studies, a |jkm> state-selected molecular beam of symmetric-top CH_3I molecules was focused with an inhomogeneous hexapole electric field and subsequently oriented along a specific laboratory direction with a homogeneous electric field. By crossing this oriented beam of CH_3I with a beam of Rb or K atoms, it was demonstrated that reaction preferentially occurs when the iodine end of CH_3I is pointed toward the reactive alkali species, thus providing first experimental insights for steric effects in simple atom-abstraction processes.

Although the hexapole focusing methods have enjoyed widespread use,[5-8] this technique is typically constrained to molecules exhibiting a large, first-order Stark effect. Alternatively, electric-field techniques have been developed that exploit the second-order Stark effect to align the rotational states of linear molecules.[9-11] More recently, Loesch and coworkers[12-14] and Friedrich *et al.*[15,16] have utilized strong homogeneous electric fields to create highly oriented "pendular" states of rotationally cooled linear molecules by the so-called "brute force" technique. Such methods have been particularly successful in linear hydrogen-bonded clusters,[17-21] where the large dipole moments and small rotational constants make them especially convenient to manipulate into the pendular regime.

The use of DC electric field methods for alignment and orientation requires the molecule to have a large permanent dipole moment, which significantly limits the range of applicability. Alternatively, magnetic-field alignment techniques developed by Herschbach and coworkers can be applied more generally to both polar and nonpolar molecules, but with the restriction that these species must be paramagnetic.[22,23] In principle, optical (AC) field methods offer more generality; for example, polarized light can be used to orient or align molecules by single-photon excitation,[24-30] selective photodissociation,[31-33] Raman scattering,[34,35] laser-induced AC Stark effect,[36,37] or intense non-resonant laser fields.[38-40] Indeed, much of the work in the area of rotational alignment has been carried out simply using single-photon excitation followed by polarized fluorescence detection, with the necessary theoretical framework developed by Zare and coworkers and Meyer for parallel bands of linear and symmetric-top molecules,[41-45] and by Weida and Parmenter for perpendicular transitions of symmetric-top molecules as well as a-, b-, and c-type transitions of asymmetric tops.[46] Unlike static DC field methods, rotational alignment via single-photon excitation requires no permanent dipole moment; however, it does require significant transition strengths and a relatively long-lived upper state.

A more general alternative is the use of collisions in an anisotropic velocity distribution to create the alignment, as pictured schematically in Fig. 4.1 for linear molecules without internal degrees of freedom. When a velocity gradient exists between such molecules, collisions along the direction of flow will preferentially align their angular momenta (**j**) *perpendicular* to the flow. Stated physically, the molecules with **j** parallel to the flow present a larger cross sectional area for collisional reorientation, while molecules with **j** perpendicular to the flow are less likely to be hit. As modeled by Zare and coworkers,[47] even if all such collisions simply randomize the direction of **j**, this will lead to a net alignment of angular momenta perpendicular to the gas flow (i.e., negative alignment). This concept of

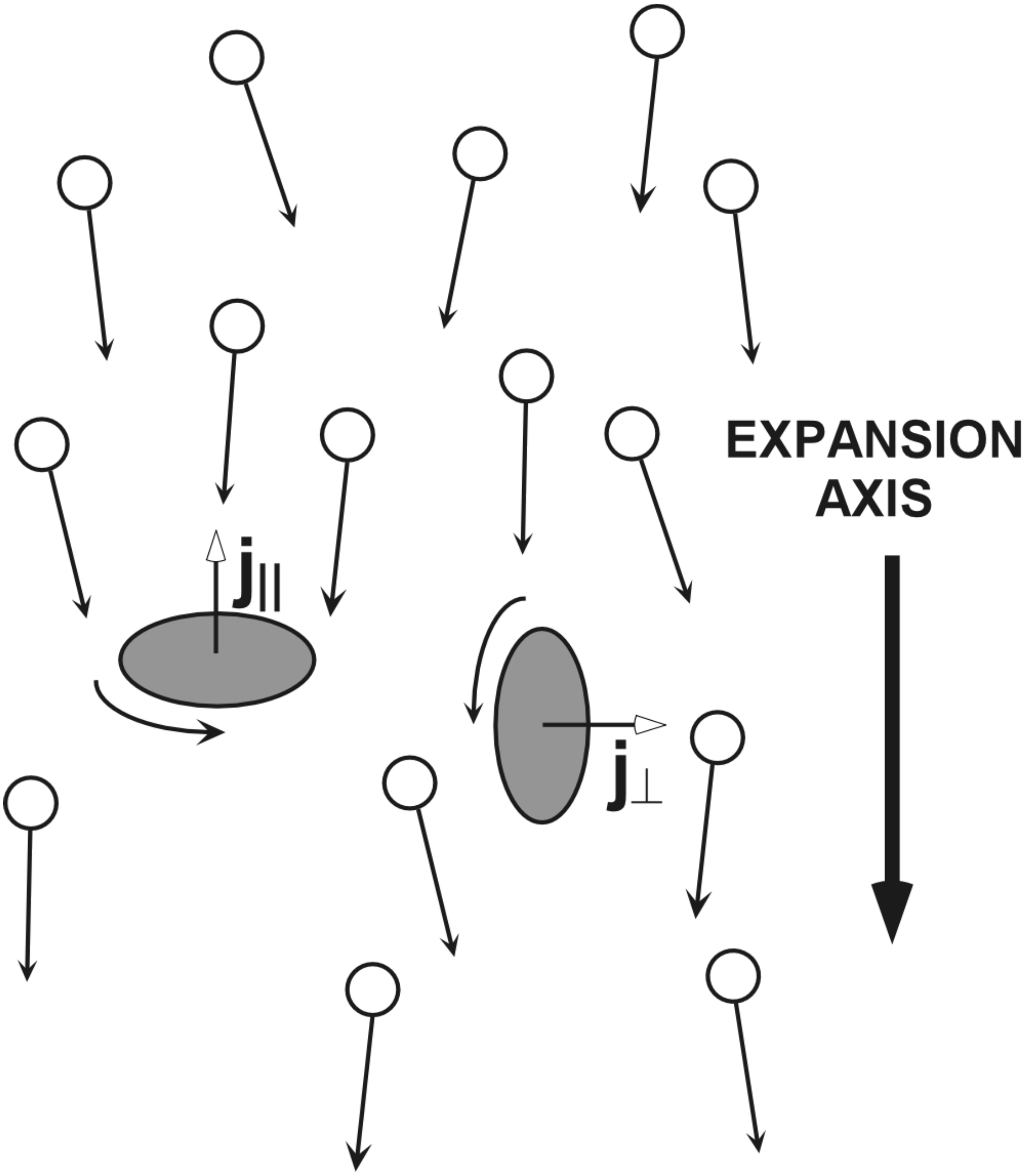

Figure 4.1. A schematic depiction of collisional alignment in supersonic expansions. The lighter, faster-moving "diluent" atoms (white circles) collide with heavier, slower-moving "seed" rotor molecules (gray ovals) along the expansion axis. Rotor molecules with **j** parallel to the expansion axis present a larger collisional cross section than those with **j** perpendicular and thus are more subject to reorienting collisions.

alignment by reorienting collisions, first presented by Gorter,[48] can be easily extended to alignment in supersonic expansions. For an expansion mixture containing a lighter “diluent” gas and a heavier “seed” gas, velocity gradients cause the slower-moving seed gas molecules to undergo multiple, anisotropic collisions with the faster-moving diluent gas molecules. These directed collisions align seed molecule rotations by creating an anisotropic distribution of m_j along the expansion axis.

Indeed, such anisotropically aligned distributions of seed molecules in a supersonic expansion were observed as early as the 1970s by the Zare group, who studied directed collisions in a neat expansion of Na atoms (“diluent”) with small concentrations of Na_2 (“seed”) to align the rotations of the dimers.[47] Since then, many experimental studies have demonstrated collisional alignment of rotor molecules for a wide range of collision partners and expansion conditions, producing aligned distributions of Na_2,[49,50] I_2,[51-55] CO_2,[56] CO,[57] O_2,[58-60] and N_2.[61] These studies demonstrate the powerful generality of collisional alignment: in principle, any non-spherical molecule (i.e., with an anisotropic state-to-state collision cross section) can be rotationally aligned by collisions in a directed flow.

While several studies have attempted to characterize the alignment process, contrasting descriptions of the collisional mechanism have arisen. For example, experimental IR-based studies by Weida and Nesbitt demonstrate that alignment of CO_2 seeded in a He expansion becomes increasingly negative as a function of CO_2 rotational angular momentum;[56] this is quite similar to the observations of Hefter *et al.*[49] in Na expansions, which indicate increasingly negative alignment of Na_2 with j up to j = 10. Conversely, under certain expansion conditions Herschbach and coworkers find that alignment of I_2 in Ne becomes *less* negative with I_2 rotational angular momentum,[53,54] though only a limited number of rotational levels were accessed with their laser excitation source. Quite recently, studies of the alignment dependence on the final velocity of the "seed" molecule have produced more strikingly contradictory results. For example, experiments performed by the Aquilanti group on O_2 and N_2 with a range of diluent gases including He indicate that rotor molecules moving *faster* than the average are increasingly aligned with **j** *perpendicular* to the expansion axis.[58,61] On the other hand, studies by Harich and Wodtke in He + CO expansions lead to exactly the opposite conclusion, i.e., the faster CO molecules are preferentially aligned with **j** *parallel* to the expansion axis.[57]

In parallel with this experimental work, there have been several theoretical studies of collisional alignment in supersonic expansions. Early efforts by Sanders and Anderson[62] and more recent ones by Pullman *et al.*[63] have explored alignment of I_2 by Ar collisions. Sanders and Anderson specifically address the evolution of rotational alignment over multiple collisions but do not identify the mechanism for how this alignment is created on a collision-by-collision basis. Conversely, Pullman *et al.* focus exclusively on the single-collision regime, exploring the alignment dependence on impact parameter, collision energy, and I_2 initial angular momentum as a function of an Ar-I_2 model interaction potential. For all potentials studied, classical trajectories fall primarily into two regimes: trajectories at small impact parameters produce more molecules with **j** perpendicular to the collision axis, while those at large impact parameters produce more with **j** parallel. In addition, potentials with an attractive well exhibit "sticky," long-lived collision complexes. This ultimately leads to aligned molecules with **j** perpendicular to the relative velocity vector, although with overall alignments typically smaller in magnitude than direct collisions.

The recent experimental results highlight important new theoretical issues not adequately addressed by previous work. For example, the final j-state and velocity dependence of the rotational alignment remain relatively unexplored. Furthermore, the contradictory velocity dependences reported for He + O_2 and He + CO alignment studies raise the possibility of extreme sensitivity to the molecular interaction potential. Given these qualitative differences and the importance of the interaction potential suggested by the Ar-I_2 collisional alignment simulations, further study of the role of the interaction potential in these particular systems would appear to be in order.

The focus of this chapter is a detailed investigation of collisional alignment mechanisms in supersonic expansions. To facilitate comparison with experiment, three collision systems (He + CO_2, He + CO, and He + O_2) have been studied that are based on realistic interaction potentials. Using classical trajectory calculations, the supersonic jet expansion conditions are simulated by producing multiple collisions between He “diluent” gas atoms and single “seed” molecules along the expansion axis. To address the possible dependence of alignment effects on initial collision velocity, these studies are performed for three different collision energies corresponding roughly to three different temperature regions ($\approx$ 300 K, 100 K and 20 K) in the expansion. These simulations permit direct comparison with experimental results, as well as an opportunity to investigate the mechanism for alignment formation on a collision-by-collision basis.

The remainder of this chapter is organized as follows. In Sect. 4.2, we describe the details of the computations used to model the supersonic expansions. In Sect. 4.3, we discuss the results of these computations, addressing both multicollisional alignment effects and single-collision mechanistic details. In Sect. 4.4, we compare these results to experiments and discuss the implications. The conclusions of our studies are summarized in Sect. 4.5.

4.2 Computational Approach

To investigate the mechanism of collisional alignment in supersonic expansions, classical trajectory calculations are used to simulate multiple-collision dynamics between light "diluent" gas atoms and heavier "rotor" molecules. To address the dependence of alignment on relative velocity, three different regions of the expansion are represented, corresponding to 300 K (E_{com} = 266 cm^{-1}), 100 K (E_{com} = 89 cm^{-1}) and 20 K (E_{com} = 18 cm^{-1}) collision conditions. The choice of O_2, CO, and CO_2 "seed" rotor molecules and He "diluent" atoms enables direct comparison of these trajectory calculations to the experiments of Aquilanti *et al.*,[58] Harich and Wodtke,[57] and Weida and Nesbitt.[56] A multicollision simulation consists of a single rotor molecule undergoing many successive but uncorrelated collisions (up to $N_{coll} \approx$ 200) with He atoms at the same energy (details provided below). From several thousand of these multicollision simulations, we group the results together in an ensemble of rotors (i.e., $N_{ensemble} \approx N_{sim} \cdot N_{coll} \approx 500{,}000$), from which the relevant statistics for collisional development of the rotational alignment can be explored for each choice of rotor molecule and region of the expansion.

For each multicollision simulation, we first need an appropriate He-rotor interaction potential. While details of the diluent-seed potentials have been neglected in early hard-sphere theories of collisional alignment,[47] in light of the qualitative discrepancies observed for He + O_2 versus He + CO collision systems,[57,58,61] we choose to model the He-rotor interactions as accurately as possible, with potentials experimentally determined from crossed molecular beam scattering or cluster IR-spectra studies. Figure 4.2 shows contour maps of the potentials used for He-O_2,[64] He-CO,[65] and He-CO_2.[66] At first glance, the He-O_2 and He-CO potentials appear qualitatively similar in terms of well depth and degree of anisotropy. However, unlike the symmetric He-O_2 potential, the He-CO potential differs slightly from one end of the rotor molecule ($\theta = 0^o$) to the other ($\theta = 180^o$). Furthermore, the He-CO well is slightly shallower than for He-O_2 ($D_e \approx 23$ versus 26 cm^{-1}). The He-CO_2 potential differs from the other two by its significantly greater anisotropy and much deeper well ($D_e \approx 41$ cm^{-1}).

While the He-rotor *inter*molecular potentials may or may not prove critically important to the collisional dynamics, it is reasonable to assume that the dynamics are less sensitive to rotor *intra*molecular potentials. For this reason, we approximate the rotor intramolecular degree of freedom as harmonic oscillator(s), with parameters given in Table 4.1. Furthermore, the O_2 and CO vibrational frequencies are reduced by roughly threefold to expedite longer time steps in the numerical integration.

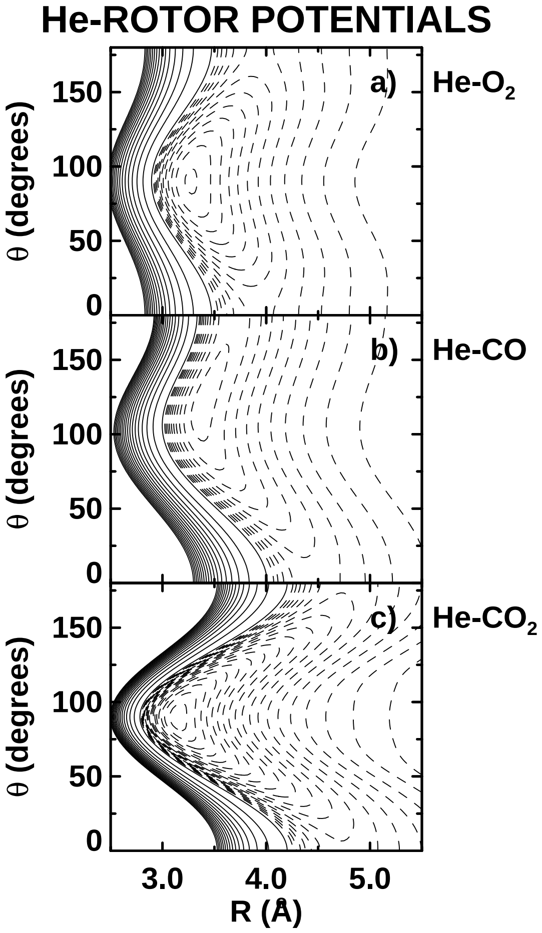

Figure 4.2. Contour plots of the potential energy surfaces for a) He-O_2, b) He-CO, and c) He-CO_2. R represents the distance between the He atom and the center of mass of the rotor, while θ represents the angle between the rotor axis and the position of the He atom. θ equal to 0^o or 180^o corresponds to a collinear configuration, while θ equal to 90^o corresponds to a T-shaped configuration (for He-CO, the C points toward the He at 0^o). The solid contours represent 20-cm^{-1} increments in the positive region of the potential, while the dashed contours represent 2-cm^{-1} increments in the negative region. The well depths are approximately a) 26 cm^{-1} for He-O_2, b) 23 cm^{-1} for He-CO, and c) 41 cm^{-1} for He-CO_2.

Table 4.1. Intramolecular harmonic potential parameters and effective "hard sphere" He + rotor cross sections, used to normalize the number of collisions (see text for details).

	Potential Parameters					$\sigma(\text{Å}^2)$		
	μ(amu)	r_e (Å)	ω_1 (cm^{-1})	ω_2 (cm^{-1})	ω_3 (cm^{-1})	266 cm^{-1}	89 cm^{-1}	18 cm^{-1}
O_2	32	1.207	600			21	25	28
CO	28	1.128	600			24	29	33
CO_2	44	1.16	1351.2	672.2	2396.4	26	29	31

Since these vibrational spacings are still more than twofold larger than the highest collision energies sampled, translational-vibrational (T-V) energy transfer effects are still anticipated (and numerically verified) to be insignificant. However, since the low-frequency bending mode of CO_2 ($\nu_2 \approx 667$ cm^{-1}) is already close to this limit, the known experimental harmonic frequencies are used for each CO_2 vibrational frequency.[67] In all cases, vibrational excitation from a single collision is verified to be ≤ 2% and more typically ≈ 0.1% of the zero-point energy for the lowest-frequency vibration.

Initial conditions for the He and rotor are selected following the procedure of Raff and Thompson.[68] For each expansion region, we select a single collision energy corresponding to $\frac{1}{2}\mu\langle v_{rel}^2\rangle$, where $\sqrt{\langle v_{rel}^2\rangle}$ is the rms relative speed of the rotor and He gas at the characteristic temperature, placed entirely in He atom velocity towards a stationary rotor atom. This temperature is also used for Boltzmann sampling of initial rotational states, so that the collisions do not significantly heat up or cool the ensemble. The initial coordinates of the rotor are obtained by random selection of its orientation in the rotational plane. The result is monoenergetic collisions with an isotropic, Boltzmann distribution of rotors at the given temperature with no initial alignment. Trajectories are initiated at sufficiently large He-rotor distances so that intermolecular interactions are negligible (≤0.1% of the well depth), with the He placed at a random distance (10-20 Å for O_2 and CO, 15-30 Å for CO_2) “upstream” of the rotor along the collision axis. Initial impact parameters for the collision are also randomly sampled from a uniform distribution (i.e., weighted by $2\pi b db$), with a maximum value (b_{max}) of 5 Å for He + CO and He + O_2 and 7 Å for He + CO_2. Convergence with respect to maximum impact parameter is explicitly verified for each collision system. In the He + O_2 system, for example, trajectory ensembles have been studied with b_{max} ranging from 2.0 Å to 10.0 Å; the resulting collisional alignment grows rapidly with b_{max} up to ≈2.8 Å, then grows by ≤10% for a 3.6-fold further increase in b_{max} from 2.8 Å to 10 Å. For multiple collisions with a single rotor molecule, the rotor’s center-of-mass translation is reset to zero at the end of each collision, while its rotational speed and angle with respect to the collision axis are retained.

The trajectories are calculated by integrating Hamilton's equations of motion in Cartesian coordinates with a variable-order, variable-stepsize, Adams-method numerical integrator.[69] To ensure that a collision has had the opportunity to occur, each trajectory is run for a minimum time period $\tau = 2R_o/v_o$, where R_o is the initial

He-rotor distance and v_o is the initial relative velocity. The trajectory terminates when the He-rotor interaction potential is negligible, i.e., less than 10^{-4} of the total kinetic energy. Step size constraints are chosen to maintain conservation of energy better than 10^{-4} and typically 10^{-5} for a single-collision trajectory. This permits sufficient computational speed without significantly affecting the predicted alignments: for example, a test ensemble of 100 multicollision simulations of He-O_2 at 266 cm^{-1} calculated with 100-fold tighter constraints yields asymptotic alignments differing by less than the statistical uncertainty (<3%). For every collisional event in a multicollision simulation, we record the impact parameter (b), the magnitude of the classical initial and final rotor angular momenta (j_i, j_f), the initial and final projections of **j** along the collision axis $\{(m_j)_i, (m_j)_f\}$, and the final rotor velocity along that axis. These values provide the necessary information for analysis of alignment as a function of number of collisions, collision energy, angular momentum, and final rotor velocity for comparison with experimental results. In particular, this enables the alignment formation to be examined on a collision-by-collision basis.

Once a trajectory in an ensemble has been generated, the final alignment is calculated as follows. For a given m_j state, the classical angle between the rotor angular momentum vector, **j**, and the collision axis is obtained from $\theta = \cos^{-1}(m_j/j)$. For a distribution of final m_j/j states and hence values of θ, the alignment can be described by an expansion in even-order Legendre polynomials,

$$\rho(\cos\theta) = \tfrac{1}{2}[1 + a_2P_2(\cos\theta) + a_4P_4(\cos\theta) + \ldots], \qquad (4.3)$$

where ρ is the probability density of molecules with **j** pointing at an angle θ with respect to the collision axis. For this normalized probability distribution, i.e., $\int\rho(\cos\theta)\, d(\cos\theta) = 1$, the coefficients are obtained simply from $a_n = (2n+1)\langle P_n(\cos\theta)\rangle$. Although higher order (n = 4, 6, …) alignment information in these distributions is clearly available, only the lowest (n = 2) term can be determined experimentally from a one-photon absorption study. Thus, we focus on the a_2 alignment values, calculated from the expectation value of $P_2(\cos\theta)$, i.e.,

$$a_2 = 5\langle P_2(\cos\theta)\rangle = [5/N_{sim}]\sum_{i=1}^{N_{sim}} P_2(\cos\theta_i) \qquad (4.4)$$

where $N_{sim} \approx 2000\text{-}5000$ represents the number of trajectories averaged. As expected, all odd moments of the Legendre expansion explicitly vanish within statistical uncertainty for all multicollision simulations. Since each rotor in a simulation has undergone multiple collisions with He, the net a_2 alignment of the ensemble is obtained by calculating $\langle P_2\rangle$ over all of the multicollision simulations at that collision number. The net result is the a_2 alignment as a function of number of collisions for each ensemble of trajectories. For comparison with experimental results, the quantum mechanical quantity $A_0^{(2)}$ approaches $\frac{2}{5}a_2$ in the high-j, semiclassical limit.[2]

4.3 Results

4.3.1 Multicollision alignment

In this subsection, the results of the multicollision simulations are presented, with a focus on i) the rate with which the alignment develops with collision number, and ii) how the magnitude of this alignment depends on collision energy and potential. To make things simpler, we focus initially on the He + O_2 simulations, which provide the least computationally intensive system for sampling and testing various parameters. As described in Sect. 4.2, the a_2 alignment parameter can be calculated as a function of the number of collisions (N_{coll}) by averaging $P_2(\cos\theta)$ for each collision over all simulations within a given ensemble. It is more meaningful to renormalize N_{coll} to the effective number of hard-sphere collisions by

$$Z_{eff} = N_{coll}\,\sigma/(\pi b_{max}^2) \tag{4.5}$$

where σ represents the effective hard-sphere collision cross section at each collision energy as determined from the potential (see Table 4.1) and b_{max} is the maximum impact parameter sampled.

A plot of a_2 for the three collision energies (266 cm^{-1}, 89 cm^{-1}, and 18 cm^{-1}) is presented in Fig. 4.3 as a function of Z_{eff}. First of all, within statistical error, the alignment parameter decreases more or less smoothly from isotropic (i.e., $a_2 \approx 0$) to an asymptotic value near $a_2 \approx -0.4$. The negative sign of this asymptotic alignment is in good agreement with experiment and indeed confirms that more molecules are

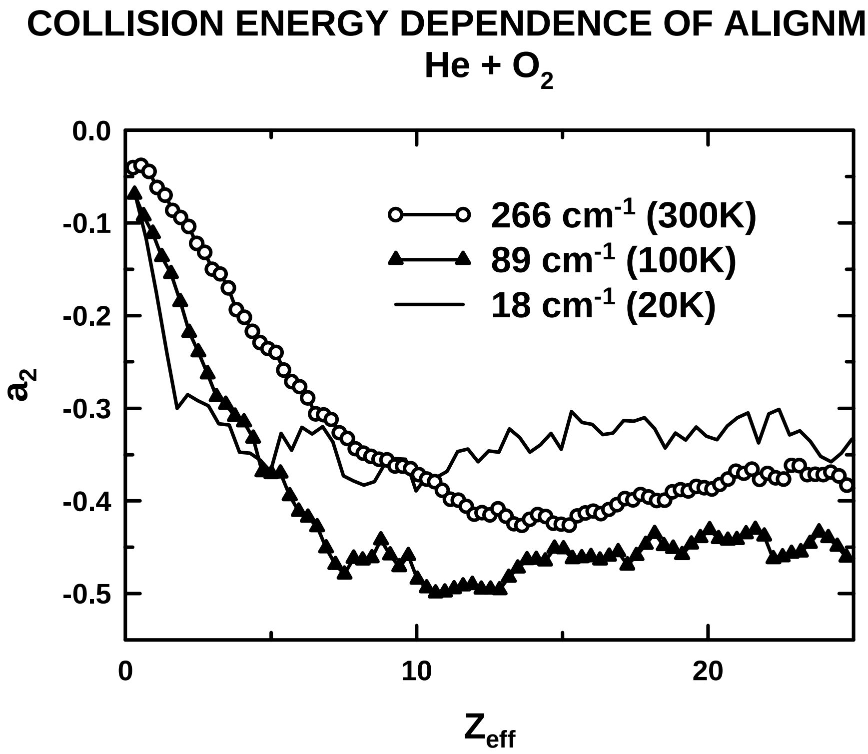

Figure 4.3. A plot of the alignment of He + O_2 versus effective collision number (Z_{eff}) at three collision energies: 266 cm^{-1}, 89 cm^{-1}, and 18 cm^{-1}. The three traces demonstrate a remarkable insensitivity to collision energy: all three reach asymptotic alignments within 30% of each other, despite a 15-fold variation in collision energy.

aligned with **j** perpendicular than **j** parallel to the collision axis. Secondly, this asymptotic behavior is typically achieved in ≤10 effective hard sphere collisions. Finally, even though the final rotational distributions vary dramatically for the three collision energies, the asymptotic alignments are within ≈ 30%. In other words, the classical magnitude of the final rotor alignment is rather insensitive to collision energy.

For a quantitative comparison of these He + O_2 alignment results with the other potentials, the alignment versus collision number has been fit to a rising exponential of the form $a_2 = a_2^{\infty} [1-e^{-Z_{eff}/\beta}]$, where a_2^{∞} corresponds to the asymptotic value of a_2 and β corresponds to the number of collisions to achieve $(1-1/e) \approx 63\%$ of this asymptotic alignment. The results of these fits for simulations on all three potentials are summarized in Figs. 4.4a and b. As expected, $a_2^{\infty} < 0$ for all potentials, indicating a net excess of rotors with **j** perpendicular versus parallel to the expansion axis. Moreover, the asymptotic alignments obtained for all three potentials (but most especially He + O_2 and He + CO) reflect a surprising insensitivity to a nearly 15-fold change in collision energy. However, significant variations are observed when comparing results *between* different potentials, specifically in i) the magnitude of asymptotic alignment (a_2^{∞}) and ii) β, the 1/e number of collisions required to reach this alignment. For example, $|a_2^{\infty}|$ increases substantially from to O_2 to CO to CO_2. Furthermore, roughly an order of magnitude as many collisions are required to reach these asymptotic alignment values for CO versus O_2 and CO_2.

Closer inspection of the three collision potentials indicates angular anisotropy to be the source of these effects, i.e., the variation in R on a given isoenergy contour for a full revolution of the rotor (see Fig. 4.2). In particular, this angular anisotropy increases from He-O_2 to He-CO to He-CO_2: the zero-energy contour for He-O_2 varies by only $\Delta R \approx 0.4$ Å, which should be compared with the much larger anisotropy values of ≈ 0.8 Å and 1.0 Å exhibited for He-CO and He-CO_2 potentials, respectively. Since this angular anisotropy is the only way the dynamics distinguish side versus

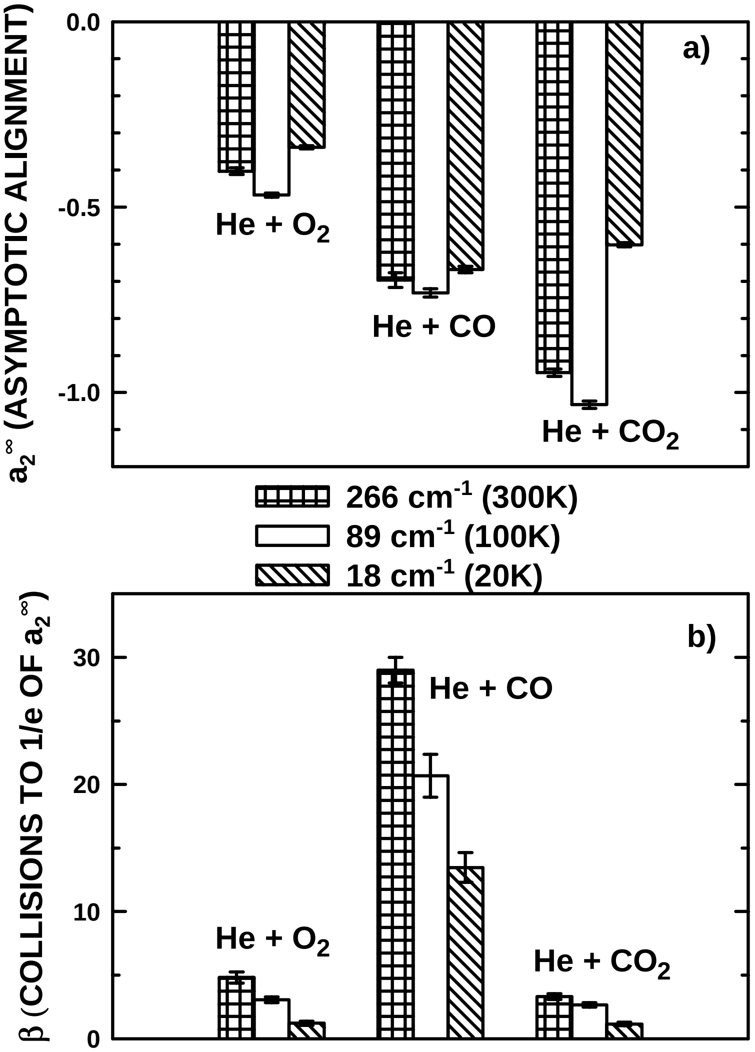

Figure 4.4. Results of fitting the alignment versus collision number data for He + O_2, CO_2, and CO to $a_2 = a_2^\infty\,[1-e^{-Z_{eff}/\beta}]$. Errors bars correspond to ±2σ in the fit. a) The asymptotic alignment, a_2^∞, is insensitive to collision energy for all three potentials and increases from O_2 to CO to CO_2, reflecting the increased anisotropy of the potentials (see Fig. 4.2). b) β, the number of collisions to achieve (1-1/e) ≈ 63% of this asymptotic alignment, increases dramatically from He + O_2/CO_2 to He + CO, reflecting presence of odd terms in addition to even terms of a Legendre expansion of the He + CO potential.

end-on collisions, one therefore expects and observes the net alignment to increase from He + O_2 to He + CO/CO_2.

Also notable is the substantial *decrease* in alignment for the lowest energy collisions of He + CO_2 versus the relatively energy independent alignments observed for He + CO and He + O_2 (see Fig. 4.4a). This effect can be attributed to the greater well depth for He-CO_2.[64-66] Since 18-cm^{-1} collision energies correspond to less than half the depth of the He-CO_2 well, one expects far more long-lived collisions than observed for He-O_2 and He-CO. The presence of such “sticky” collision trajectories ultimately results in memory loss of the initial direction of the relative velocity vector, thereby diminishing the net alignment.[63] Indeed, additional He + O_2 trajectories have been performed at $E_{com} = 9$ cm^{-1} (i.e., less than half the He-O_2 well depth) that indicate resulting O_2 alignments to be similarly reduced at these lower collision energies. In general, however, these results indicate a remarkably low sensitivity to collision energy, which motivates our focus on trajectory ensembles at a single collision energy in the following sections.

More striking is the large difference in rates at which these three systems come to the asymptotic alignment value, as seen in Fig. 4.4b. While the asymptotic alignment magnitudes can be rationalized by anisotropy differences in the potentials, the reason for the larger number of collisions needed to align CO is less apparent. However, one feature of the CO potential that distinguishes it from the others is the asymmetry of the two rotor ends, which contributes additional odd versus even terms in the Legendre expansion of the potential. As a result, the potential is significantly asymmetric with respect to He-CO and He-OC configurations, with a well closer to the C end. In addition, the shift between the bond midpoint and center of mass makes the CO rotational axis asymmetric with respect to hard-sphere potential edges of the O and C atoms. A slowly approaching He atom therefore preferentially collides with the C end of the rotor, sampling the potential well region non-uniformly. This asymmetric sampling consequently requires a much larger number of collisions for CO to reach asymptotic alignment than for either CO_2 or O_2.

4.3.2 Dependence on Rotor Angular Momentum

As mentioned in Sect. 4.1, several experimental studies indicate a dependence of alignment on final rotational quantum state. Both Hefter *et al.*[49] and Weida and Nesbitt[56] have found alignment to increase with j; interestingly, this alignment appears to vanish when extrapolated to j = 0, which has led to the suggestion that this j-dependence might result from the 2j + 1 quantum mechanical degeneracy of the rotational level. Indeed, a simple geometric model based on these ideas qualitatively predicts a monotonic increase in $A_0^{(2)}$ to an asymptotic value with j.[56] This makes it especially intriguing to see if these j-dependent trends are reproduced from a purely classical perspective.

To illustrate how the alignment depends on the rotor angular momentum, j, we again focus on the He + O_2 ensemble data at a single collision energy (266 cm^{-1}), though similar trends at all other collision energies are observed as well. As described previously, a_2 is calculated after each collision by averaging P_2 over all of the multicollision simulations. However, prior to the calculation of a_2, each rotor is first sorted into a bin according to its postcollision angular momentum, j. Three bin ranges are chosen to examine the alignment behavior at "low," "intermediate," and "high" j values relative to a 300 K distribution. These bins are j/<j> = 0.0-0.4, 0.8-1.2, and 1.6-2.0 (where <j> ≈ 10.2 for O_2 at 300 K) and correspond to the darkened regions shown in Fig. 4.5. At each collision number in a multicollision ensemble, the j-dependent alignment is extracted from $<P_2>$ for all the rotors in a given j bin.

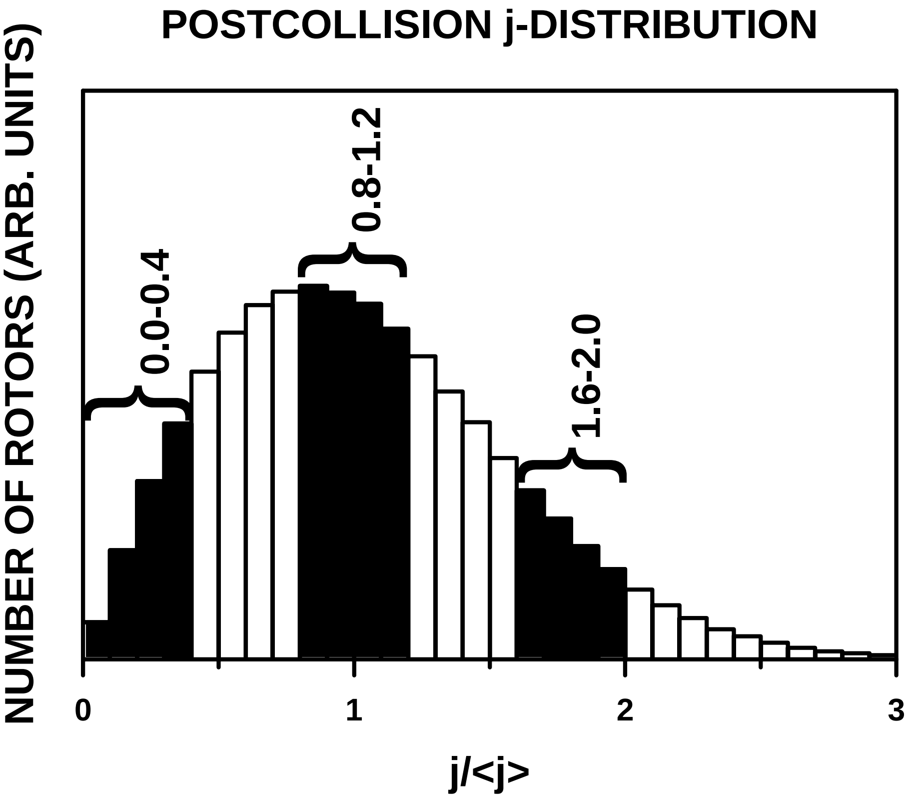

Figure 4.5. The distribution of rotor angular momenta (j) after a single collision at 266 cm^{-1} (300 K). This is divided into "low" (j/<j> = 0.0-0.4), "intermediate" (j/<j> = 0.8-1.2), and "high" (j/<j> = 1.6-2.0) angular momentum bins for calculating the alignment dependence on j.

A plot of this j-dependent alignment of O_2 as a function of collision number is given in Fig. 4.6. Notably, the asymptotic alignment depends quite strongly on j, starting at essentially zero (within uncertainty) for the lowest range of j values and becoming increasingly negative with increasing j. This result is consistent with the work of Weida and Nesbitt in He + CO_2 coexpansions,[56] as well as the work of Hefter *et al.* in Na + Na_2 expansions.[49] This is a particularly interesting result to obtain from purely classical calculations, since vanishing alignment at low j has previously been rationalized in terms of j-dependent degeneracies.[56] However, there is a similar j-dependence in the semiclassical density of rotational states, which also vanishes in the limit of j = 0. Thus, while it is not surprising that such alignment trends can be reproduced by purely classical trajectory calculations, this will necessitate further discussion in Sect. 4.4 of alternative, non-quantum mechanical explanations for this j-dependence.

With the j-dependent alignments corroborated by He + O_2 simulations, we extend our study to the other two potentials. Specifically, the distributions of a_2 versus collision number are sorted into the same j/<j> bins for the multicollision ensembles of He + CO and He + CO_2 at 266 cm^{-1} (with <j> = 8.8 and 20.0 at 300 K for CO and CO_2, respectively) and fit to a rising exponential. The results of this fit, given in Fig. 4.7, show that the trends are the same for all three potentials, with the alignment monotonically increasing with rotor angular momentum. The variation in magnitude among potentials within each j/<j> range simply reflects the variation in overall alignment noted previously in Fig. 4.4a.

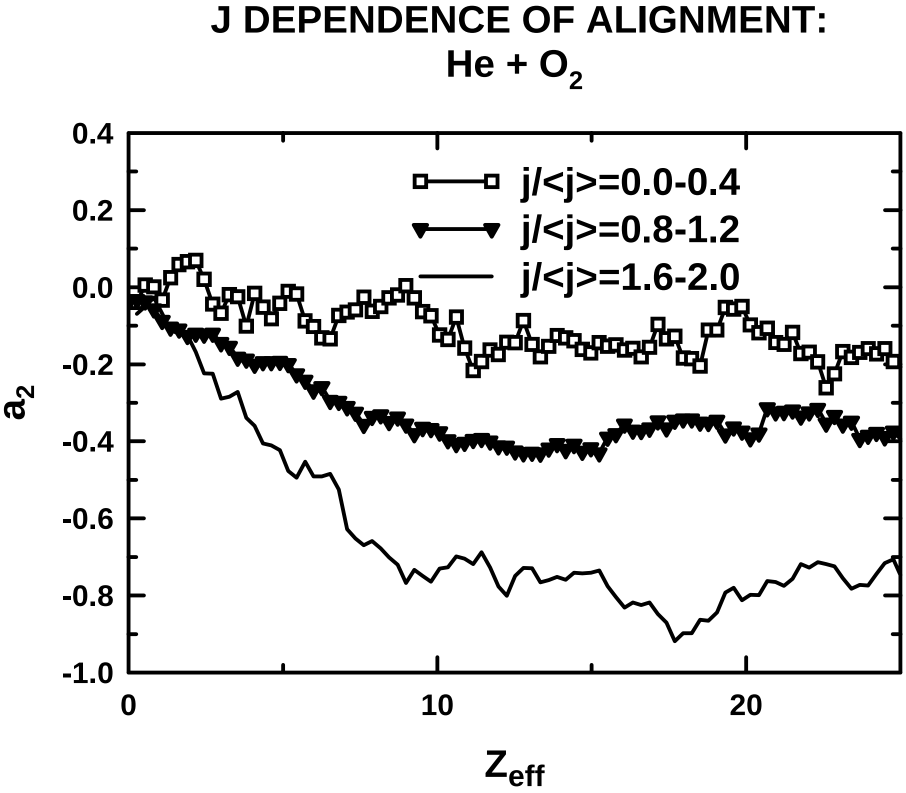

Figure 4.6. Alignment (a_2) as a function of effective collision number (Z_{eff}) for low (j/<j> = 0-0.4), intermediate (j/<j> = 0.8-1.2), and high (j/<j> = 1.6-2.0) angular momentum values for the He + O_2 collision system. The magnitude of the asymptotic alignment increases with j in this system.

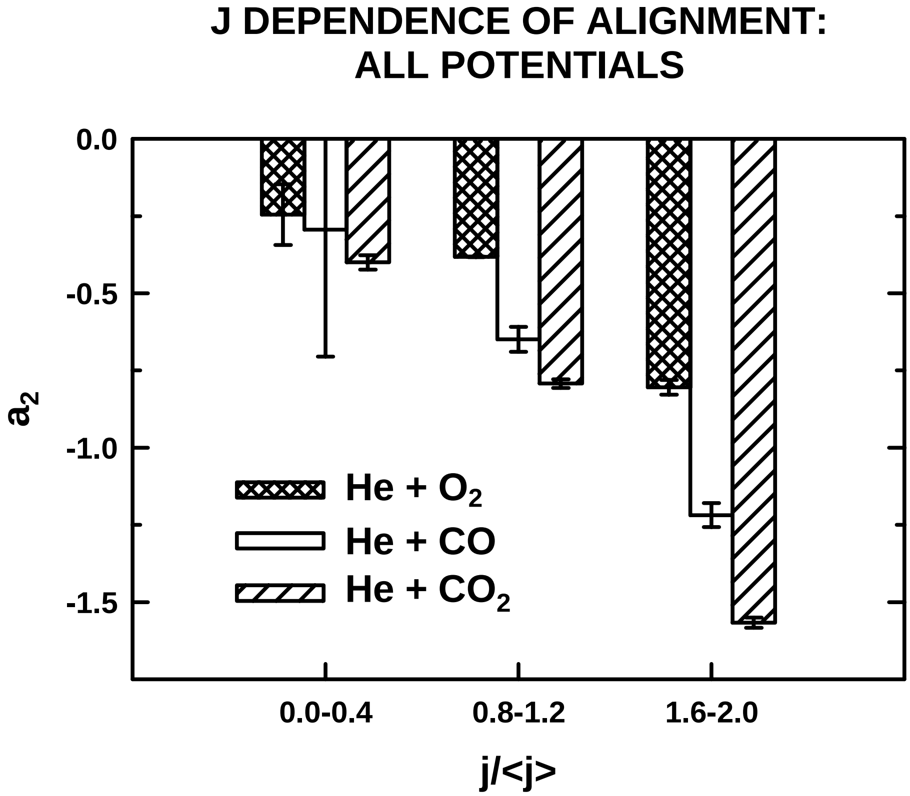

Figure 4.7. Asymptotic alignment (a_2^{∞}) for He + O_2, CO, and CO_2 for low (j/<j> = 0-0.4), intermediate (j/<j> = 0.8-1.2), and high (j/<j> = 1.6-2.0) angular momentum values. Error bars represent ±2σ in the exponential fit. While the magnitudes of the alignments vary among the potentials, the trend for all three potentials is that alignment increases with j.

The next step is to investigate how this alignment is created, specifically by identifying correlations between initial and final states in the production of an aligned distribution. One important observation in this regard is evident in Fig. 4.4b, i.e., the alignment grows in gradually over several collisions. Thus, one plausible mechanism is that the incoming alignment of a rotor molecule (i.e., classically m_j/j) influences the probability of a given final alignment. From this perspective, the rotor alignment is formed by a series of m_j/j-changing collisions that ultimately funnel the angular momentum states into an aligned distribution. To explore this possibility, the individual collision trajectories are analyzed to obtain a probability map for all $(m_j/j)_i \rightarrow (m_j/j)_f$ transitions. In order to improve the statistics, approximately 500,000 single-collision simulations are included for each of the potentials. Furthermore, the single-collision $(m_j/j)_i \rightarrow (m_j/j)_f$ distributions are additionally split into the same j/<j> bins used above, but where j now refers to the angular momentum state prior to the collision.

Sample He + O_2 probability maps of $(m_j/j)_f$ versus $(m_j/j)_i$ for the three ranges of j/<j> are presented in Fig. 4.8 and indicate several features worth noting. First of all, for the lowest values of j/<j> (Fig. 4.8a), single collisions from each $(m_j/j)_i$ produce a large spread in $(m_j/j)_f$, i.e., little correlation exists between the initial alignment of an O_2 molecule and its final alignment after a collision. However, as j increases from Fig. 4.8a to c, this spread in $(m_j/j)_f$ for a given $(m_j/j)_i$ narrows dramatically, collapsing into a tight band along $(m_j/j)_f \approx (m_j/j)_i$. Thus, the rotor's initial alignment with respect to the collision axis is largely conserved for high j.

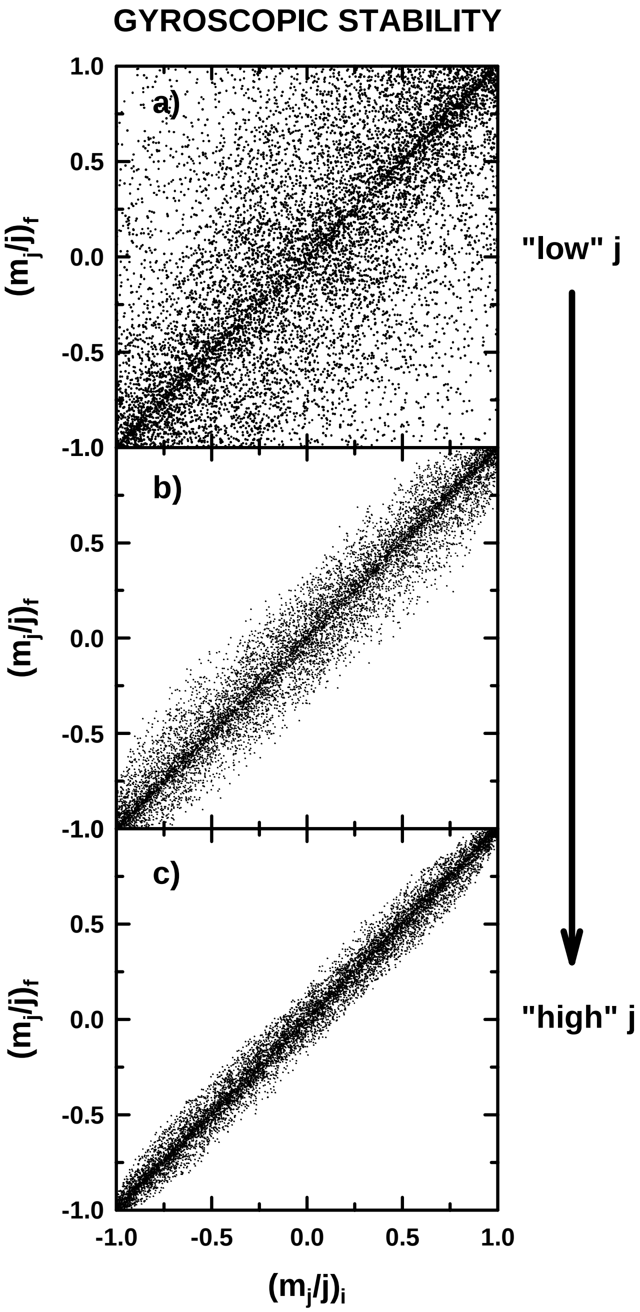

Figure 4.8. Plot of initial m_j/j versus final m_j/j for an ensemble of 500,000 He + O_2 collisions at 266 cm^{-1} for a) low (j/<j> = 0-0.4), b) intermediate (j/<j> = 0.8-1.2), and c) high (j/<j> = 1.6-2.0) angular momentum values. As j/<j> increases, the spread in $(m_j/j)_f$ for each $(m_j/j)_i$ narrows considerably, reflecting the increased gyroscopic stability of higher j states.

This result is not limited to the He + O_2 system: He + CO and He + CO_2 studies also demonstrate that the spread in $(m_j/j)_f$ decreases by roughly an order of magnitude from the lowest to the highest j range. Simply stated, single collisions are far less effective at scrambling molecular alignment at high j than low j; this physically reflects the increased gyroscopic stability of more rapidly spinning rotor molecules. This also begins to explain the strong j dependence of the asymptotic alignments observed, since any alignment created by a series of collisions is far more easily erased by additional collisions for low j than for high j rotors.

The next stage in investigating how alignment is created is to determine the types of collisions that change m_j/j, i.e., to explore whether m_j- or j-changing collisions predominate. To this end, the single-collision He + O_2 trajectories are sorted by size of the collisional change in m_j (i.e., Δm_j) and in j (i.e., Δj); the resulting distributions can be analyzed by i) what fraction of collisions produce significant changes in m_j or j and ii) the magnitude of these changes. To facilitate this comparison, “non-collisional” events are excluded by limiting the maximum impact parameter to be the average hard-sphere collision radius of O_2 (2.9 Å), and both Δm_j and Δj are scaled by $\langle j \rangle$. Figure 4.9 reports histograms of the resulting distributions. Notably, >70% of the collisions produce non-negligible changes for both m_j and j (i.e., greater than 5% of $\langle j \rangle$). More importantly, the Δm_j and Δj distributions are quite similar, implying that neither type of collision predominates in developing the rotor alignment. The relevance of this finding to previous studies will be explored in Sect. 4.4.

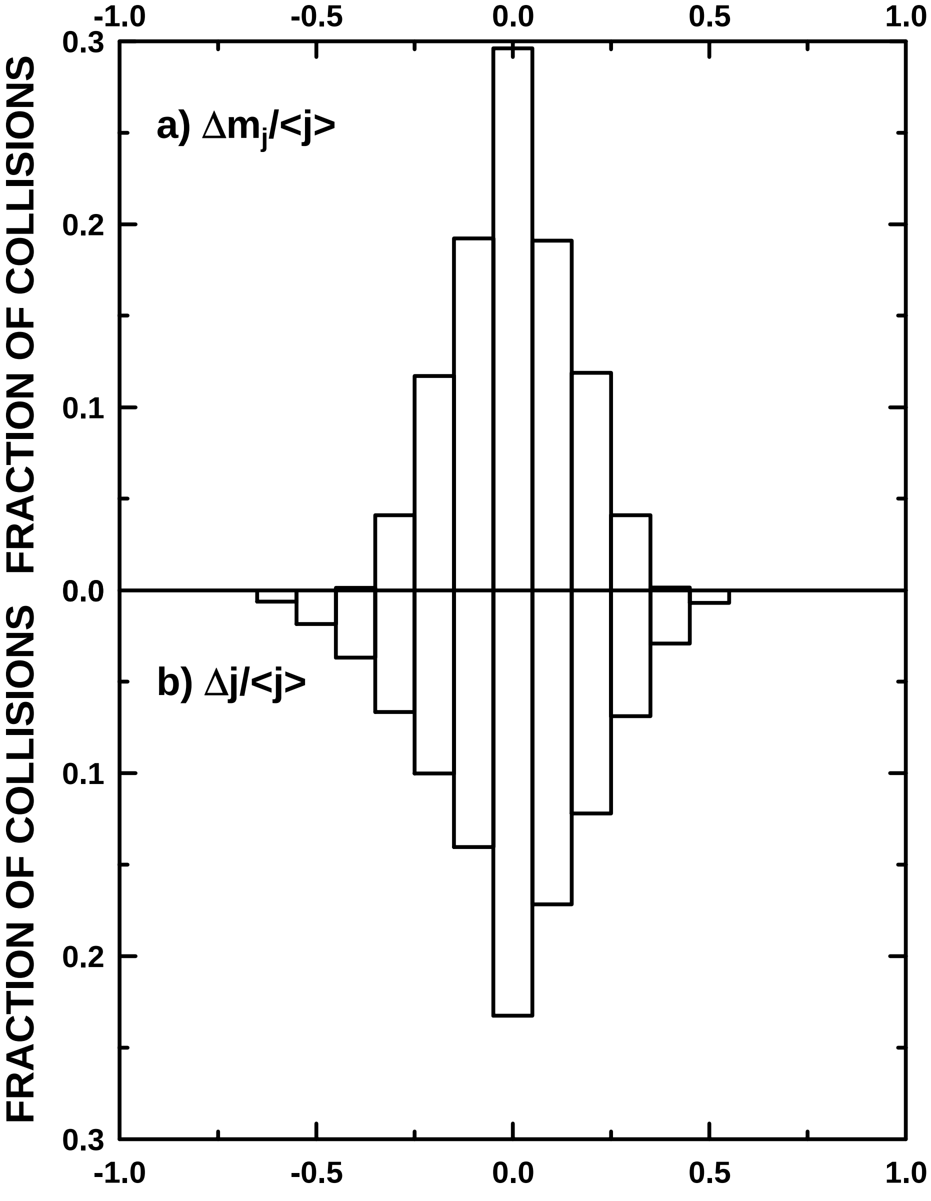

Figure 4.9. Distributions of a) $\Delta m_j/<j>$ and b) $\Delta j/<j>$ for an ensemble of 500,000 He + O_2 collisions at 266 cm^{-1}. The similarity in these distributions indicates that both $\Delta m_j \neq 0$ and $\Delta j \neq 0$ collisions are significant in creating alignment.

4.3.3 Velocity dependence

In addition to providing insight into j-dependent alignment, the single-collision regime can be used to examine the dependence of the alignment on the final rotor velocity. Indeed, discrepancies between the studies of Aquilanti *et al.*[58] and Harich and Wodtke[57] on this velocity dependence provided the initial incentive for these calculations, specifically to address whether subtle differences in the two intermolecular surfaces could be responsible for such clear differences in experimental results.

Since the multicollision simulations demonstrate the alignment to be insensitive to collision energy, we simply consider the 500,000-trajectory, single-collision ensembles at 266 cm^{-1} (300 K) for each potential. To carry out this comparison, the change in rotor velocity component along the expansion axis (i.e., from zero initially to its post-collision value) is recorded for each trajectory. The average final velocity (normalized to the velocity predicted for a head-on elastic collision) is then calculated for each bin of $(m_j/j)_f$. In order to prevent statistical skewing by non-collisions at large impact parameter, we exclude events with a final velocity ≤10% of the elastic upper limit. To examine the results for a possible j-dependence, the single-collision data are separated into j bins defined previously.

Fig. 4.10 contains a plot of the post-collision rotor velocity versus final m_j/j state, with the velocity expressed as a percent difference from the average final velocity integrated over all alignments, i.e., $\Delta v/\langle v\rangle$. The upward curvature at the ends of this distribution clearly demonstrates that on average, molecules with $|m_j/j| \approx 1$ are faster than $|m_j/j| \approx 0$. Stated explicitly, molecules with **j** *parallel* to the

ALIGNMENT DEPENDENCE ON FINAL ROTOR VELOCITY

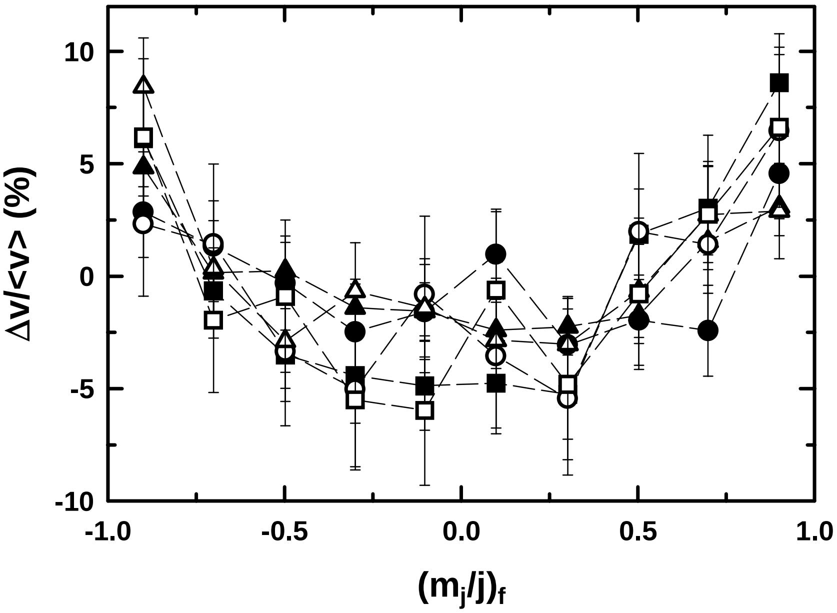

Figure 4.10. The percent difference of the final rotor velocity from the alignment–averaged final rotor velocity, $\Delta v/\langle v\rangle$ versus $(m_j/j)_f$. The data are binned by $j/\langle j\rangle$ and He + rotor potential as follows: ● = 0.0-0.4, He + O_2; ▲ = 0.8-1.2, He + O_2; ■ = 1.6-2.0, He + O_2; O = 0.0-0.4, He + CO; Δ = 0.8-1.2, He + CO; □ = 1.6-2.0, He + CO. Error bars represent $\pm 2\sigma$ of the mean. The upward curvature of this data indicates that, on average, molecules with $|m_j|/j_f \approx 1$ (i.e., **j** parallel to the collision axis) are faster than those with $|m_j|/j_f \approx 0$ (i.e., **j** perpendicular). This trend is the same for all potentials and ranges of j shown.

expansion axis are on average moving *faster* than those with **j** perpendicular, with a roughly 15% spread in velocity around the average velocity after a single collision. In addition, this velocity-dependent alignment is virtually identical for He + O_2 and He + CO, thus ruling out any major dependence on subtle differences in the two intermolecular potentials. Furthermore, this trend is robustly independent of angular momentum, i.e., the data for all j ranges in Fig. 4.10 overlap within statistical uncertainties. In summary, these calculations predict the faster (slower) rotor molecules to exhibit a more positive (negative) alignment, i.e., **j** preferentially parallel (perpendicular) to the expansion axis, with little sensitivity to the interaction potential or rotational quantum number.

These velocity-dependent trends are most consistent with the results of Harich and Wodtke. To quantify the comparison between theory and experiment, Harich and Wodtke's velocity dependent alignment data for He + CO(j=6) have been reanalyzed as a classical distribution of m_j/j states as a function of final velocity. For each m_j/j, an average final rotor velocity is calculated and plotted in Fig. 4.11 as $\Delta v/\langle v\rangle$. Superimposed on this line is the final velocity distribution of rotor molecules obtained from our calculations, averaging over all j values and both potentials. The trends in the experimental and calculated data are clearly quite similar: molecules aligned with **j** perpendicular to the collision axis ($|m_j/j| \approx 0$) travel more slowly than those with **j** parallel ($|m_j/j| \approx 1$). The implications of these results will be further developed below.

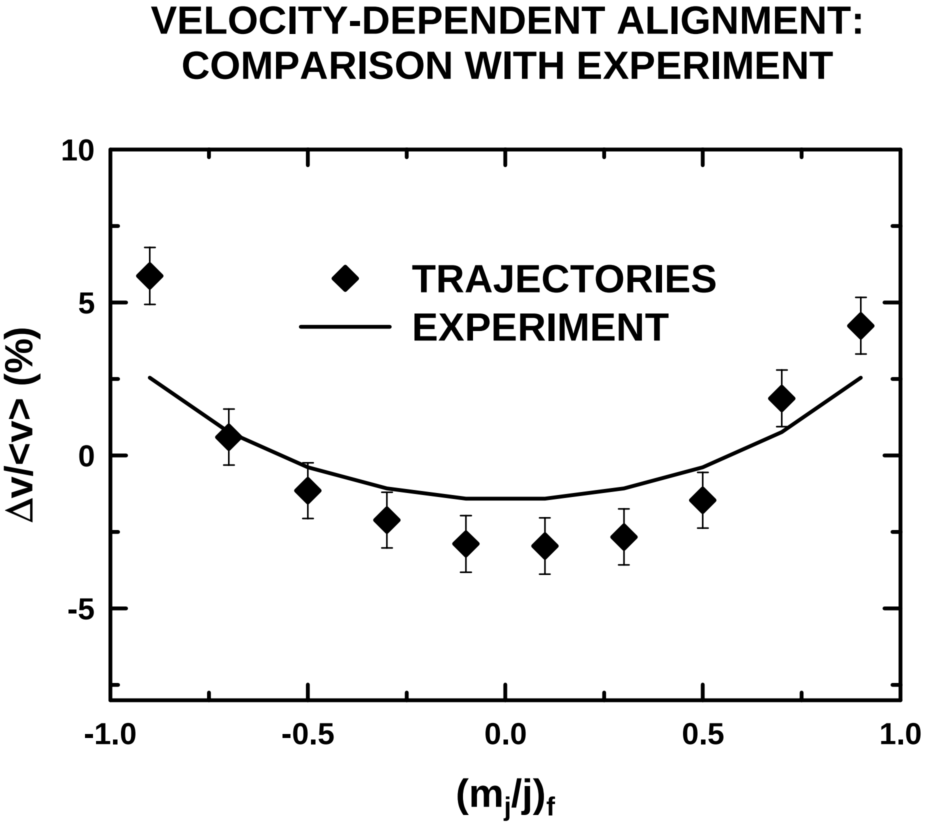

Figure 4.11. Comparison of the experimental jet-expansion data of Harich and Wodtke to the overall average Δv/<v> versus $(m_j/j)_f$ obtained by averaging the classical-trajectory data in Fig. 4.11 over all j and both potentials. Both the multicollision experimental results and the single-collision classical trajectories demonstrate the same trend: on average, molecules with $|m_j|/j_f \approx 1$ are faster than those with $|m_j|/j_f \approx 0$.

4.4 Discussion

Several of the results obtained in this study warrant further discussion. First of all, the overall trends in the theoretical alignments are in excellent agreement with experiment. The multicollision simulations predict $a_2 < 0$ for all potentials, supporting the simple picture that rotor molecules with **j** parallel to the expansion axis present a larger cross section to the colliding He diluent and thus are more likely to experience realigning collisions. Somewhat more surprisingly, this alignment appears to be quite insensitive to collision energy. Specifically, the asymptotic alignments indicate less than 40% changes over an order of magnitude range in E_{com} for all three collision systems tested. Indeed, only at energies significantly lower than the well depth for each collision system do the alignments decrease noticeably, a trend that can be ascribed to increased probability of long-lived versus direct collision trajectories. This indicates that high velocity slip conditions (e.g., at the throat of the expansion) or much slower collisions (e.g., further downstream) can both contribute to the rotor alignment, provided that the relative velocities are sufficiently well aligned with respect to the expansion axis. This is especially relevant to comparisons between experimental results, where different expansion conditions yield different final jet temperatures, velocity slips, and thus relative scalar speeds of the diluent gas and rotor species.

In the multicollision ensembles, the maximum alignments ranged from a lower limit of $a_2 \approx -0.46(1)$ (for He + O_2), to $a_2 \approx -0.73(1)$ (for He + CO), to the highest value of $a_2 \approx -1.03(1)$ (for He + CO_2). By way of contrast, experimental studies for He + CO_2 indicate maximum CO_2 alignment of $A_0^{(2)} \approx -0.115$,[56] which in the classical limit corresponds to a_2 = -0.29, i.e., ≈ threefold smaller than obtained from the current work. Similarly, the experimental CO alignment (integrated over all velocities) for He + CO studies is $A_0^{(2)}$ = -0.08;[57] this corresponds classically to a_2 ≈ -0.2, which is also roughly threefold smaller than suggested by the multicollision simulations. In essence, despite excellent qualitative agreement for alignment trends as a function of both velocity and rotor angular momentum, the maximum alignment values theoretically predicted are quantitatively much higher than those measured experimentally.

These discrepancies reflect the different nature of collisions in the simulations versus the jet expansions. In the theoretical simulations, all collisions occur at the same center of mass energy and are directed initially along the expansion axis. In contrast, the collisions in a supersonic expansion take place over a range of relative energies as the molecules cool and, more importantly, over a wider range of collision angles. The distribution of relative energies is not responsible for these differences, since the alignment results are quite insensitive to collision energy. Likely to be much more relevant is the subsequent influence of this cooling on the distribution of collision velocities in the expansion. At large values of velocity slip, most diluent gas-seed gas collisions are strongly aligned along the expansion axis; however, as this velocity slip approaches zero, collisions with the seed gas molecule will be far less aligned. For example, the studies of Weida and Nesbitt indicate that velocity slip for CO_2 in the late stages of a He + CO_2 expansion is as low as a few percent; thus, most collisions are essentially isotropic with respect to the laboratory-frame expansion axis. This excess of non-directional collisions can lead to efficient scrambling of the rotational alignment produced up to that stage; indeed, Halpern *et al.*[70] and Schade *et al.*[71] have demonstrated such collisional loss of alignment for acetylene and NO, respectively. This effect has been explicitly noted in the He + CO_2 studies: as a function of distance downstream, the net CO_2 alignment reaches a maximum and then steadily decreases due to nominally unaligned collisions late in the expansion. The neglect of velocity slip/angular effects in the current theoretical studies clearly leads to an overestimation of the asymptotic alignment values, i.e., in the direction consistent with the observed differences.

Despite these quantitative differences between the magnitudes of theoretical and experimental alignments, the agreement is qualitatively quite good and provides support for a closer examination of the underlying alignment mechanism. For example, when alignment is further partitioned by rotor angular momentum, the classical trajectory simulations demonstrate that the asymptotic values increase monotonically with j for each of the three intermolecular potentials. Contrary to previous interpretations, this j-dependent alignment can not be ascribed entirely to quantum effects contributing at low j, since the same trends are clearly evident also in classical trajectory calculations. This j dependence is most likely due to increased gyroscopic stability, i.e., the faster a classical rotor is spinning, the more stability it exhibits toward collisional torques changing the alignment. This point is most dramatically made in Figs. 4.6a-c, which indicate a significant decrease in the distribution of m_j/j with increase in j after a single collision. As a result, once high-j molecules become aligned, they are less likely to be tilted away from this alignment by subsequent collisions. This concept of the stability of higher j states against m_j/j-changing collisions is supported by studies of pressure-broadening coefficients, which generally indicate a rapid decrease with increasing j state.[72-76] Furthermore, Hulsman and Korving report that cross sections for reorienting collisions between Ar and Na_2 decrease strongly with angular momentum, with a dependence nearly proportional to $1/j^2$.[50]

This discussion of j-dependent alignments would seem to suggest that multiple, m_j-changing collisions are the primary mechanism for alignment in supersonic expansions. Indeed, previous work by Weida and Nesbitt[56] demonstrates that alignment of CO_2 in a supersonic expansion becomes increasingly negative with j, a phenomenon they attribute to m_j-changing collisions. Likewise, a quantum close-coupled calculation by Werner and coworkers[77] on collisional alignment of N_2^+ ions with He demonstrate cross sections for m_j-changing collisions (at fixed j) that are significantly larger than j-changing collisions (at fixed m_j). Consequently, the alignment observed by Dressler *et al.*[78] in the corresponding He drift tube experiment has been attributed to m_j-changing collisions at more or less fixed j. More recent work by Anthony *et al.* on these He-N_2^+ drift tube experiments demonstrates that the most negative alignments occur at high j.[79]

Herschbach and coworkers have developed an alternate explanation of the collisional alignment involving j-changing collisions. Experimentally, they monitor alignment of I_2 as a function of final jet temperature, observing that as the final temperature decreases, the negative alignment of a given j state reaches a maximum and begins to decrease again, eventually becoming positive under certain expansion conditions.[54] They ascribe this phenomenon to a contribution from *anisotropic* *rotational cooling*: molecules with **j** perpendicular to the collision axis experience a greater torque than those with **j** parallel and are thus cooled more rapidly. Consequently, this would predict an excess of rotors with **j** predominantly perpendicular to the expansion axis at low j (i.e., cooler temperatures) and relatively fewer molecules with **j** perpendicular in the high j states, and thus a net a_2 alignment that becomes more *positive* with *increasing* j. Since the collision energy used in each of our calculations is the mean temperature used to sample the rotational distribution (i.e., the two are roughly equivalent), these studies cannot directly assess the validity of the anisotropic rotational cooling model relative to the other models. However, it is clear from Fig. 4.9 that both m_j- and j-changing collisions are occurring at similar frequencies and contribute to the m_j/j alignment.

The velocity-dependent alignments presented in Fig. 4.10 demonstrate several interesting points. First of all, the sign of the resulting velocity-averaged alignment is correctly predicted to be negative, irrespective of the magnitude of the velocity slip. However, when one investigates alignment as a function of deviations *away from* the average speed, the results are more subtle. Specifically, the rotor molecules moving faster than the average ($\Delta v > 0$) have a greater propensity for **j** perpendicular to the expansion axis than the more slowly moving velocity groups ($\Delta v < 0$). Most importantly, this behavior is exhibited for all values of j for both He + CO and He + O_2 collision systems and so does not appear to be sensitive to the detailed shape of the intermolecular potential. Over multiple collisions in a supersonic expansion, this effect predicts a net negative alignment ($a_2 < 0$) for the slower rotor molecules and positive alignment ($a_2 > 0$) for the faster molecules, i.e., exactly the same trend reported by Harich and Wodtke in supersonic expansions of He + CO. Such behavior supports the simple physical picture discussed by Harich and Wodtke that rotor molecules with **j** parallel to the expansion axis present a larger collisional cross section to the diluent gas, preferentially experiencing more directed collisions and hence more forward acceleration with respect to the average rotor speed.

In further support of this interpretation, both the computational results and the work of Harich and Wodtke can be compared with the work of Anthony *et al.* on velocity-resolved collision-induced alignment of N_2^+ in a He drift tube.[79,80] Interestingly, these studies reveal that *faster* N_2^+ drift velocities are associated with more negative alignment (the alignment even becomes positive at the lowest velocities for the lowest j values). At first glance, this greater propensity for **j** *perpendicular* versus **j** parallel to the drift axis at the highest ion velocities would appear to be in disagreement with both the supersonic jet He + CO studies and the current theoretical results. However, as pointed out by Harich and Wodtke, the rotor molecules in supersonic expansions are *accelerated* by collisions with the faster-moving diluent gas, while the ions in a drift tube, pulled through the buffer gas by an external electric field, are *decelerated* by collisions with the buffer. As a result, the fast end of the velocity distribution reflects those ions which have suffered fewer collisions, which is therefore consistent with the more negative alignments (i.e., **j** perpendicular preferred over **j** parallel) observed experimentally at higher velocities.

By way of contrast, experiments on He + O_2 and He + N_2 by Aquilanti and coworkers indicate that alignment in a supersonic expansion becomes more negative for the higher velocity molecules, i.e., the concentration of rotors with **j** perpendicular to the expansion axis increases with $\Delta v > 0$. This is qualitatively different from the He + CO results of Harich and Wodtke, the He + N_2^+ ion alignment studies of Anthony *et al.*, and the theoretical predictions from the current work. There are at least two factors that should be considered as possible sources for this discrepancy. First of all, not all the experiments of Aquilanti and coworkers have been performed on collision systems (e.g., He + N_2) sampled in other studies. However, the theoretical results obtained in this work are robustly independent of the intermolecular potential for all three systems (He + CO, He + O_2, He + CO_2); it would be quite surprising if the behavior for He + N_2 were somehow significantly different. Furthermore, the theoretical trends observed in the current study for the two systems investigated by Harich and Wodtke and Aquilanti and coworkers, i.e., He + CO and He + O_2, are essentially identical.

Secondly, the experiments on He + O_2 by Aquilanti and coworkers have been performed under much stronger expansion conditions, thus sampling lower j values than in the He + CO experiments. In this regard, it is worth noting that calculations in this work have been carried out over nearly a 15-fold range of jet temperatures, though none as low as Aquilanti and coworkers. Indeed, quantum cross section calculations have been performed by Aquilanti and coworkers for the He-O_2 collision system[81] in which authors attribute the quite different velocity effects between their studies and those of Harich and Wodtke to differences in expansion conditions. Specifically, Aquilanti and coworkers probe in only a very small solid angle along the forward-/backward-scattered direction while Harich and Wodtke necessarily average over a broader range of angles. Therefore, one possible explanation might be that the different scattering angles sampled in the two experiments produce different velocity-dependent alignments. However, this would also suggest a strong dependence of these velocity effects on impact parameter, whereas our calculations indicate essentially identical alignment trends (i.e., **j** perpendicular faster than **j** parallel) for all impact parameters, with b_{max} as low as 0.1 Å. In essence, these classical trajectory calculations do not provide a satisfactory explanation for the experimental discrepancies in velocity dependent alignments but do indicate that differences in scattering for the two intermolecular potentials (He + O_2 vs. He + CO) are not sufficient to resolve this issue.

4.5 Summary

Classical trajectory calculations have been carried out on experimentally determined potentials for He-O_2, He-CO, and He-CO_2 to explore the collisional mechanism for rotational alignment and to facilitate comparison with previous experimental studies. These calculations demonstrate that for multiple collisions between a light "diluent" gas, He, and a heavy "seed" rotor, the rotor molecules become anisotropically aligned with a clear propensity towards **j** perpendicular to the expansion axis. This alignment grows in with an approximately exponential dependence on the number of collisions and a 1/e collision number that varies from ≈ 2 to 30. The sign and magnitude of this asymptotic alignment are found to be remarkably insensitive to collision energy over more than an order of magnitude dynamic range, as well as to the detailed shape of the interaction potential.

In addition to this examination of the overall alignment from multiple-collision simulations, j-dependent effects have also been explored. These simulations reveal the asymptotic alignment to depend strongly on rotor angular momentum, increasing in magnitude with j for all three potentials studied and conversely vanishing as j tends toward zero. The evidence of this behavior in a purely classical simulation indicates that experimental trends of vanishing alignment for low j states cannot be simply ascribed to quantum effects near j = 0. Investigated on a collision-by-collision basis, the higher j states appear to be far more stable with respect to collisional destruction of the alignment. Specifically, the statistical spread in the final alignment $(m_j/j)_f$ for a given initial alignment $(m_j/j)_i$ narrows dramatically with j, consistent with the simple physical picture of greater classical gyroscopic stability for more rapidly spinning rotors.

With regard to velocity dependent alignments, the calculations indicate that molecules moving faster than the average velocity have their angular momenta preferentially aligned parallel to the expansion axis, in agreement with the experimental observations of He + CO collisions by Harich and Wodtke. This provides theoretical support for this physical picture of the alignment process: rotor molecules with **j** parallel to the relative velocity axis are struck from behind more often by seed gas molecules than rotors with **j** perpendicular to this axis and thus are preferentially accelerated ahead of the average rotor velocity distribution. These simple models are also consistent with the velocity dependent He + N_2^+ ion drift experiments of Anthony *et al.* but as yet do not appear to be consistent with the behavior reported by Aquilanti for He + O_2 and He + N_2 collision dynamics.

References for Chapter 4

1. See, for example, A. J. Orr-Ewing and R. N. Zare, Annu. Rev. Phys. Chem. **45**, 315 (1994); H. J. Loesch, Annu. Rev. Phys. Chem. **46**, 555 (1995); A. J. Orr-Ewing, J. Chem. Soc. Faraday Trans. **92**, 881 (1996).

2. C. H. Greene and R. N. Zare, *Ann. Rev. Phys. Chem.* **33,** 119 (1982).

3. R. J. Beuhler, Jr., R. B. Bernstein, and K. H. Kramer, *J. Am. Chem. Soc.* **88,** 5331 (1966).

4. P. R. Brooks and E. M. Jones, *J. Chem. Phys.* **45,** 3449 (1966).

5. P. R. Brooks, *Science* **193,** 11 (1976).

6. S. Stolte, *Ber. Bunsenges. Phys. Chem.* **86,** 413 (1982).

7. D. H. Parker, H. Jalink, and S. Stolte, *J. Phys. Chem.* **91,** 5427 (1987).

8. D. H. Parker and R. B. Bernstein, *Ann. Rev. Phys. Chem.* **40,** 561 (1989).

9. H. G. Bennewitz, K. H. Kramer, W. Paul, and J. P. Toennies, *Z. Phys.* **177,** 84 (1964).

10. J. P. Toennies, *Z. Phys.* **182,** 257 (1965).

11. A. Lubbert, G. Rotzoll, and F. Gunther, *J. Chem. Phys.* **69,** 5174 (1978).

12. H. J. Loesch and A. Remscheid, *J. Chem. Phys.* **93,** 4779 (1990).

13. H. J. Loesch and A. Remscheid, *J. Phys. Chem.* **95,** 8194 (1991).

14. H. J. Loesch and J. Moller, *J. Chem. Phys.* **97,** 9016 (1992).

15. B. Friedrich and D. R. Herschbach, *Nature* **353,** 412 (1991).

16. B. Friedrich, H.-G. Rubahn, and N. Sathyamurthy, *Phys. Rev. Lett.* **69,** 2487 (1992).

17. P. A. Block, E. J. Bohac, and R. E. Miller, *Phys. Rev. Lett.* **68,** 1303 (1992).

18. R. J. Bemish, M. Wu, and R. E. Miller, *Faraday Discussions* **97,** 57 (1994).

19. M. Yang, M. H. Alexander, C.-C. Chuang, R. W. Randall, and M. I. Lester, *J. Chem. Phys.* **103,** 905 (1995).

20. R. J. Bemish, M. C. Chan, and R. E. Miller, *Chem. Phys. Lett.* **251,** 182 (1996).

21. D. T. Moore, L. Oudejans, and R. E. Miller, *J. Chem. Phys.* **110,** 197 (1999).

22. B. Friedrich and D. R. Herschbach, *Z. Phys. D* **24,** 25 (1992).

23. A. Slenczka, B. Friedrich, and D. Herschbach, *Phys. Rev. Lett.* **72,** 1806 (1994).

24. M. Hoffmeister, R. Schleysing, and H. J. Loesch, *J. Phys. Chem.* **91,** 5441 (1987).

25. Z. Karny, R. C. Estler, and R. N. Zare, *J. Chem. Phys.* **69,** 5199 (1978).

26. R. C. Estler and R. N. Zare, *J. Am. Chem. Soc.* **100,** 1323 (1978).

27. W. R. Simpson, T. P. Rakitzis, S. A. Kandel, A. J. Orr-Ewing, and R. N. Zare, *J. Chem. Phys.* **103,** 7313 (1995).

28. W. Kim and P. M. Felker, *J. Chem. Phys.* **104,** 1147 (1996).

29. W. Kim and P. M. Felker, *J. Chem. Phys.* **107,** 2193 (1997).

30. M. J. Weida and C. S. Parmenter, *J. Phys. Chem. A* **101,** 9594 (1997).

31. H. G. Dehmelt and K. B. Jefferts, *Phys. Rev.* **125,** 1318 (1962).

32. M. S. deVries, G. W. Tyndall, C. L. Cobb, and R. M. Martin, *J. Chem. Phys.* **86,** 2653 (1987).

33. G. Ravindra Kumar, P. Gross, C. P. Safvan, F. A. Rajgara, and D. Mathur, *Phys. Rev. A* **53,** 3098 (1996).

34. Y. B. Band and P. S. Julienne, *J. Chem. Phys.* **96,** 3339 (1992).

35. R. Dopheide and H. Zacharias, *J. Chem. Phys.* **99,** 4864 (1993).

36. A. F. Linskens, N. Dam, J. Reuss, and B. Sartakov, *J. Chem. Phys.* **101,** 9385 (1994).

37. A. D. Rudert, J. Martin, H. Zacharias, and J. B. Halpern, *Chem. Phys. Lett.* **294,** 381 (1998).

38. B. Friedrich and D. Herschbach, *Phys. Rev. Lett.* **74,** 4623 (1995).

39. B. Friedrich and D. Herschbach, *J. Phys. Chem.* **99,** 15686 (1995).

40. B. Friedrich and D. Herschbach, *Chem. Phys. Lett.* **262,** 41 (1996).

41. R. N. Zare, *Ber. Bunsenges. Phys. Chem.* **86,** 422 (1982).

42. A. C. Kummel, G. O. Sitz, and R. N. Zare, *J. Chem. Phys.* **85,** 6874 (1986).

43. A. C. Kummel, G. O. Sitz, and R. N. Zare, *J. Chem. Phys.* **88,** 6707 (1988).

44. A. C. Kummel, G. O. Sitz, and R. N. Zare, *J. Chem. Phys.* **88,** 7357 (1988).

45. H. Meyer, *Chem. Phys. Lett.* **230,** 510 (1994).

46. M. J. Weida and C. S. Parmenter, *J. Chem. Phys.* **107,** 7138 (1997).

47. M. P. Sinha, C. D. Caldwell, and R. N. Zare, *J. Chem. Phys.* **61,** 491 (1974).

48. C. J. Gorter, *Z. Phys.* **26,** 140 (1938).

49. U. Hefter, G. Ziegler, A. Mattheus, A. Fischer, and K. Bergmann, *J. Chem. Phys.* **85,** 286 (1986).

50. H. Hulsman and J. Korving, *J. Chem. Phys.* **95,** 5719 (1991).

51. W. R. Sanders and J. B. Anderson, *J. Phys. Chem.* **88,** 4479 (1984).

52. D. P. Pullman and D. R. Herschbach, *J. Chem. Phys.* **90,** 3881 (1988).

53. D. P. Pullman, B. Friedrich, and D. R. Herschbach, *J. Chem. Phys.* **93,** 3224 (1990).

54. B. Friedrich, D. P. Pullman, and D. R. Herschbach, *J. Phys. Chem.* **95,** 8118 (1991).

55. H. J. Saleh and A. J. McCaffery, *J. Chem. Soc. Faraday Trans.* **89,** 3217 (1993).

56. M. J. Weida and D. J. Nesbitt, *J. Chem. Phys.* **100,** 6372 (1994).

57. S. Harich and A. M. Wodtke, *J. Chem. Phys.* **107,** 5983 (1997).

58. V. Aquilanti, D. Ascenzi, D. Cappelletti, and F. Pirani, *Nature* **371,** 399 (1994).

59. V. Aquilanti, D. Ascenzi, D. Cappelletti, S. Franceschini, and F. Pirani, *Phys. Rev. Lett.* **74,** 2929 (1995).

60. V. Aquilanti, D. Ascenzi, D. Cappelletti, M. de Castro, and F. Pirani, *J. Chem. Phys.* **109,** 3898 (1998).

61. V. Aquilanti, D. Ascenzi, D. Cappelletti, R. Fedeli, and F. Pirani, *J. Phys. Chem. A* **101,** 7648 (1997).

62. W. R. Sanders and J. B. Anderson, *Chem. Phys. Lett.* **47,** 283 (1977).

63. D. P. Pullman, B. Friedrich, and D. R. Herschbach, *J. Phys. Chem.* **99,** 7407 (1995).

64. L. Beneventi, P. Casavecchia, and G. G. Volpi, *J. Chem. Phys.* **85,** 7011 (1986).

65. C. Chuaqui, R. J. Le Roy, and A. R. W. McKellar, *J. Chem. Phys.* **101,** 39 (1994).

66. L. Beneventi, P. Casavecchia, F. Vecchiocattivi, G. G. Volpi, U. Buck, C. Lauenstein, and R. Schinke, *J. Chem. Phys.* **89,** 4671 (1988).

67. G. Herzberg, *Infrared and Raman Spectra of Polyatomic Molecules* (Krieger, Malabar, 1991).

68. L. M. Raff and D. L. Thompson, in *Theory of Chemical Reaction Dynamics*, Vol. III, edited by M. Baer (CRC Press, Boca Raton, 1985), pp. 1.

69. NAG Fortran Library (Oxford University: Oxford, 1997)

70. J. B. Halpern, R. Dopheide, and H. Zacharias, *J. Phys. Chem.* **99,** 13611 (1995).

71. W. Schade, J. Walewski, A. Offt, and A. Knaack, *Phys. Rev. A* **53,** 2921 (1996).

72. J. P. Houdeau, M. Larvor, and C. Haeusler, *Can. J. Phys.* **58,** 318 (1980).

73. A. M. Smith, K. K. Lehmann, and W. Klemperer, *J. Chem. Phys.* **85,** 4958 (1986).

74. B. E. Grossmann and E. V. Browell, *J. Mol. Spec.* **138,** 562 (1989).

75. A. S. Pine, *J. Chem. Phys.* **91,** 2002 (1989).

76. A. Schiffman and D. J. Nesbitt, *J. Chem. Phys.* **100,** 2677 (1994).

77. B. Follmeg, P. Rosmus, and H.-J. Werner, *J. Chem. Phys.* **93,** 4687 (1990).

78. R. A. Dressler, H. Meyer, and S. R. Leone, *J. Chem. Phys.* **87,** 6029 (1987).

79. E. B. Anthony, Ph.D. thesis, University of Colorado, 1998.

80. E. B. Anthony, W. Schade, M. J. Bastian, V. M. Bierbaum, and S. R. Leone, *J. Chem. Phys.* **106,** 5413 (1997).

81. Aquilanti, V., private communication

CHAPTER 5

EXPLORING THE ROLE OF VIBRATIONAL NONADIABATIC EFFECTS IN VIBRATIONALLY MEDIATED CHEMICAL REACTIONS

5.1 Introduction

Over the past decade, the possibility of influencing chemical reactions by vibrationally mediated chemistry has enjoyed a great deal of interest and success. Originally pioneered by Crim and coworkers and Zare and coworkers for the reaction of H with water and its isotopes, it has since been extend to variety of reactive atoms (H, Cl, O) and molecular reaction partners (H_2O/HOD,[1-7] HCN,[8-10] CH_4[11-13]). Such systems provide the tantalizing possibility of pre-excitation of a particular bond in a molecule leading to selective reaction.

One means of exploring the degree of selectivity imparted by vibrational excitation has been to examine the branching ratios among possible products. For example, in the reaction of H with vibrationally excited HOD, Bronikowski showed that the relative branching ratio for OD/OH production was at least 25 from $v_{OH}=1$, while the branching ratio for OH/OD was at least 8 from $v_{OD}=1$.[1] Similar effects have been demonstrated for the reaction of HOD with other atoms and at other levels of vibrational excitation, both experimentally[2-7] and theoretically.[14-20] In addition, the Crim group's studies of nearly isoenergetic vibrational states of H_2O containing differing amounts of local-mode stretch and bend excitation demonstrated increased reactivity with H atoms when all quanta were placed in the stretch excitation.[2,3]

Another approach to determining vibrational selectivity has been to monitor how excitation in the nonreactive bond translates into product-state excitation. For example, the Crim group monitored the OH vibrational states resulting from reaction of H and Cl atoms with H_2O in two states, $|04^{-}>$ and $|13^{-}>$, where $|nm^{(+/-)}>$ denotes symmetric and antisymmetric combinations, respectively, of local mode stretches with n quanta in one bond and m quanta in the other.[3,4] These studies revealed a marked propensity toward production of OH in v=0 in the first case and OH in v=1 in the second.

From these demonstrations of mode-specific reaction a "spectator bond" paradigm has emerged, i.e., the concept that the nonreactive bond does not participate in the reaction dynamics, and any initial excitation in that bond should be retained in the final product distribution. Underlying this paradigm is an assumption of vibrational adiabaticity in the reactive species, i.e., that the initial vibrational state prepared in the reactive molecule is essentially unaffected by the approach of the reactive atom. This view of these reaction systems has increased in popularity such that reduced-dimensionality 4-atom reactive scattering calculations often fix the length of the nonreactive bond.[21]

However, a significant amount of experimental and theoretical evidence demonstrates that the nonreactive bond may not always play the role of a spectator in mode-specific reactions. Such an effect is quite dramatically demonstrated in recent experiments by the Crim group on Cl + HCN, which produced similar excitation of the product CN stretch from both Cl + HCN(004) and Cl + HCN(302),[3] where the first quantum number corresponds to a normal mode of predominately CN stretch character, and the third to a normal mode of predominantly CN character. Their initial explanation for this phenomenon was that the Cl + HCN reaction proceeds via a complex, resulting in intramolecular vibrational redistribution (IVR) prior to reaction. However, Schatz and coworkers have carried out quantum scattering calculations on the related H + HCN reaction which allow the CN bond to vibrate while constraining HHC to be collinear, a geometry that removes the possibility of complex formation.[22] They determine that excitation to HCN(100), i.e., one quantum of mostly CN stretch character, significantly enhances reaction cross section to H_2 + CN and lowers the threshold energy relative to H + HCN(000); in fact, this threshold decreases by nearly 100% of input vibrational energy.

Similar effects, albeit on a smaller scale, can be observed in the earlier studies of the reactivity of water and its isotopes mentioned previously. For example, Crim and coworkers noted a decrease in relative OH v=1/v=0 production from Cl + $H_2O|13^->$ versus H + $H_2O|13^->$.[4] Similarly, Schatz and coworkers noted in an early quasiclassical trajectory study that excitation of the OD bond in HOD or of highly excited bend states of H_2O (5-7 quanta) provides some enhancement of the H reactivity above the ground state.[14] A later study by this group, examining lower levels of vibrational excitation in HOD, again demonstrated that excitation of the OD stretch, in addition to enhancing the reaction probability of the D atom, increases H reactivity to a lesser extent.[15] More recent 6D quantum calculations of H + HOD by Zhang and Light also indicate that excitation of the OD bond does cause a slight enhancement of reaction probability for the OH bond.[20]

At the heart of these studies is the apparent breakdown of the local mode nature of the initial excitation of the reactant. The approach of the reactive atom must cause a redistribution of vibrational energy in the reactant molecule, occurring on the timescale of a chemical reaction. Correspondingly, the question emerges: what happens to the excited vibration as the atom approaches? In each of the previous studies, the primary focus has been on examining the product distribution rather than the details of the interaction of the atom with the molecular vibrations.

To address these issues, we explore vibrationally nonadiabatic effects in chemical reactions, focusing on a model system for the collinear reaction of Cl with reduced-dimensionality, linear water isotopes. Our first goal will be to determine in a time-*independent* fashion how the vibrational eigenfunctions of this model water system are affected as the Cl atom distance is parametrically decreased, focusing primarily on the v=1 stretch polyad in water. Our second goal will then be to follow the dynamics of the reaction in a time-*dependent* fashion via wavepacket propagation. In doing so, we hope to demonstrate the insight that can be gained from such a time-dependent approach.

5.2 Computational Approach

To study the reaction dynamics of Cl with water isotopes in various vibrational levels, the computational process can be divided up into three major steps.

For simplicity, these computations are primarily described for Cl + H_2O but can be applied to the other systems to be studied, i.e., Cl + D_2O and Cl + HOD (with the approach of the Cl atom along the OH bond). First, we calculate the eigenstates and eigenenergies of the water molecule as a parametric function of the Cl-H_2O internuclear distance. In doing so, we assume that the vibrational motion is separable from the relative Cl + H_2O motion, similar to the Born-Oppenheimer separation of nuclear and electronic motion,[23] in order to calculate an adiabatic basis of vibrational eigenfunctions. Thus, the total wavefunction is composed of vibrational and internuclear parts,

$$\Psi^{\mathrm{total}} = \sum_{n} \psi_n \chi_n \tag{5.1}$$

where Ψ represents the total wavefunction, ψ represents the internuclear part, and χ represents the vibrational part. The vibrational eigenstates, χ_n, are determined by solving the time-independent Schrödinger equation for the OH bonds with parametric dependence on the Cl-H_2O distance:

$$\mathbf{H}(r_1, r_2; R)\, \chi_n^{\mathrm{vib}}(r_1, r_2; R) = E_n(R)^*\, \chi_n^{\mathrm{vib}}(r_1, r_2; R) \tag{5.2}$$

where r_1 is the distance between the O atom and the H atom *proximal* to the Cl, r_2 is the distance between the O atom and the H atom *distal* to the Cl, and R is the distance from the Cl to the center of mass of the water. A plot of this coordinate system is given in Fig. 5.1. The changes in these eigenfunctions with R provide insight into

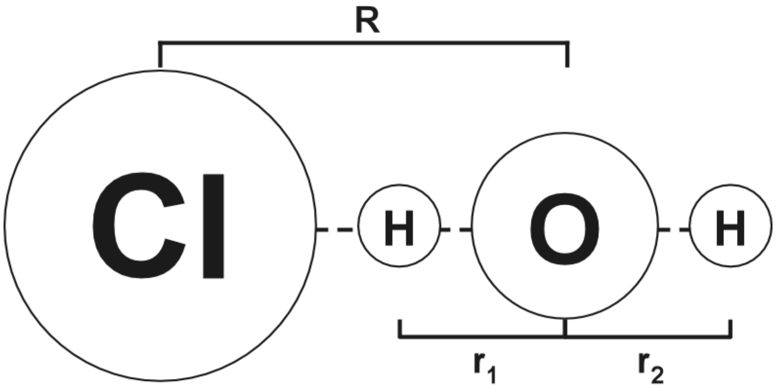

Figure 5.1. Coordinate system for Cl + HOH reactive scattering calculations. R represents the distance from the Cl atom to the center of mass of water, while r_1 is the length of the proximal OH bond (i.e., closest to the Cl), and r_2 is the length of the distal OH bond. With appropriate isotopic substitutions, this coordinate system is also used for Cl + DOD and Cl + HOD (replacing H with D on the distal OH bond).

how the water vibrations are affected by the approach of Cl. In addition, the E_n's provide one-dimensional (1D) adiabatic potential surfaces for relative Cl-H_2O motion. Accordingly, along an *uncoupled* adiabatic potential curve, the Schrödinger equation describing the intermolecular Cl-H_2O motion can be exactly written as

$$\left[\frac{-\hbar^2}{2\mu_{\mathrm{Cl,HOH}}}\frac{\partial^2}{\partial R^2}+E_n(R)\right]\psi_n(R)=E\psi_n(R) \qquad (5.3)$$

In the second step of the computational process, we must be able to transfer probability among the adiabatic curves in order to allow for inelastic or reactive scattering. These curve-crossing probabilities are governed by the nonadiabatic terms in the intramolecular Hamiltonian, essentially, a breakdown in the separation between vibrational and intermolecular motions. In this adiabatic basis, the couplings between the curves depend on the rate of change of the vibrational eigenstates as a function of R, thus depending on the velocity of approach of the Cl atom in a classical interpretation. The transition probabilities can therefore be used to estimate a characteristic curve-crossing velocity for the transition between low-velocity, adiabatic behavior and high-velocity, diabatic behavior.

In the final step of the computational process, we carry out time-dependent wavepacket propagation for the relative Cl-H_2O motion, starting with an initial entrance channel (e.g. the symmetric or antisymmetric vibration of H_2O), following the dynamics, and probing the products. These three steps are described in detail below.

5.2.1. Calculating vibrational wavefunctions at each Cl-water distance

This calculation first requires a potential surface describing the interactions of the four atoms, as well as means of representing and calculating the eigenfunctions.

The potential surface used to describe the Cl + H_2O interaction is based on the triatomic O + HCl London-Eyring-Polanyi-Sato (LEPS) potential surface given by Persky and Broida,[24] with parameters given in Table 5.1. This surface is used to describe the interaction of one OH stretch with the approaching Cl; this stretch is designated the “proximal” OH stretch, r_1. The other OH stretch is solely described the Morse potential part of the LEPS surface and is designated the “distal” OH stretch, r_2. Thus, in the subsequent calculations, the Cl atom is only allowed to approach the proximal end of the molecule. Physically, this potential surface does not accurately describe the Cl + H_2O interaction because products and reactants are nearly isoenergetic, while Cl + H_2O should be endothermic by 5640 cm^{-1}.[25] The surface was rather designed to lower artificially lower the reactive channels so that the reactive channels were more accessible at the v=1 level, simplifying our computations by limiting the number of vibrational eigenfunctions calculated. Clearly, this feature of the potential surface, as well as the linear configuration chosen for water, indicates that no quantitative comparison with experiment will be made. Rather, this system will provide a simple model for the dynamics of reaction with a heavy-light-heavy molecule; in addition, we will discuss which conclusions are valid more universally.

Table 5.1. LEPS parameters for the Cl + H_2O potential surface.

		Bond	
Parameter	O-H	H-Cl	O-Cl
$\beta(Å^{-1})$	2.295	1.868	2.290
$D_e(cm^{-1})$	37,230	37,250	23,600
$r_e(Å)$	0.970	1.275	1.570
k	0.170	0.158	-0.250
$r^‡$	1.154	1.453	

After choosing the potential surface for the four-atom interaction, a representation for the vibrational eigenfunctions, χ_n, must be designated. For this purpose, we use a Fourier expansion of the wavefunction on an evenly spaced grid, such that the expansion coefficients are equivalent to the amplitude of the wavefunction in momentum space.[26] The momentum wavefunction can thus be obtained via a Fourier transform of the coordinate wavefunction; with FFT techniques, the length of this computation scales as $N_g \log N_g$ (N_g is the number of grid points). Such a representation takes advantage of the local nature of the kinetic energy operator in momentum space, where calculation of the kinetic energy operation requires only a simple multiplication step and scales as N_g. The complete Hamiltonian operation thus scales approximately as $N_g \log N_g$, rather than the N_g^2 typically necessary for calculating derivatives of the wavefunction in position space. Altogether, the Hamiltonian in the COM frame of H_2O for the vibrational eigenfunctions, with parametric dependence on the distance between the Cl and H_2O center of mass, is exactly given by

$$
\begin{aligned}
&H = T + V \\
&V = V(r_1, r_2, R) \\
&T = \hbar^2 \left[\frac{-\partial^2}{2\mu_{OH}\partial r_1^2} + \frac{-\partial^2}{2\mu_{OH}\partial r_2^2} + \frac{\partial^2}{m_O \partial r_1 \partial r_2} \right]
\end{aligned}
\qquad (5.4)
$$

where V is the potential energy from the LEPS potential, T is the kinetic energy of the OH stretches, and r_1, r_2, and R are as defined previously. The size of the grid chosen to represent these eigenfunctions is 16×128 points, with spacings $(\Delta r_1, \Delta r_2)$ = (0.079, 0.057) Å. The larger number of points in r_1 is designed to encompass both product and reactant wells; the spatial extent represented is thus (r_1, r_2) = ([0.63, 7.94], [0.63, 1.90]) Å.

With this representation of vibrational eigenfunctions, we use a relaxation method to determine the ground-state vibrational eigenfunction,[27,28] propagating an initial trial wavefunction via the time-propagation operator in imaginary time, $\tau = it$:

$$\chi_{\mathrm{trial}}(\tau) = e^{-\mathbf{H}\tau/\hbar}\chi_{\mathrm{trial}}(0) \tag{5.5}$$

Since any trial wavefunction represents a superposition of all the eigenstates of the Hamiltonian, each eigenstate will be damped out exponentially at a rate proportional to its energy; thus, the ground-state eigenfunction will die out most slowly. Accordingly, as $\tau \rightarrow \infty$, χ_{trial} will collapse to the ground-state eigenfunction. Thus, obtaining the ground state eigenfunction requires repeated application of the propagation operator $e^{-\mathbf{H}\tau/\hbar}$ to the trial wavefunction. Since the relaxation process does not preserve the norm of the wavefunction, the length of the timestep is limited by the need to renormalize χ_{trial} repeatedly to avoid reaching machine precision.

Next, the excited-state eigenfunctions are calculated via the same relaxation method. However, for each excited state, all previously determined lower eigenstates are first projected out from the trial wavefunction, so that an expansion of the trial wavefunction in the eigenfunctions of the system contains only excited-state wavefunctions. Accordingly, propagation in imaginary time will collapse the wavefunction to the lowest excited state included, i.e., the next-higher state in energy.

In practice, all lower eigenstates are projected out at each imaginary timestep to avoid collapsing to a lower state via numerical instabilities.

To employ this relaxation technique for determining the eigenstates, we expand the propagation operator in imaginary time in a series of Chebychev polynomials, i.e.,

$$e^{-\mathbf{H}\tau/\hbar} \cong \sum_{n=0}^{N} a_n(\tau)\, T_n(-\mathbf{H}\tau/\hbar) \tag{5.6}$$

where the T_n are real Chebychev polynomials and the a_n are the expansion coefficients described below.[27] Because Chebychev polynomials are exponentially convergent on [-1, 1], the Hamiltonian must be renormalized such that its eigenvalues span that range, with

$$\Delta E = E_{max} - E_{min} = (T_{max} + V_{max}) - V_{min} \tag{5.7}$$

$$E_{avg} = (E_{max} + E_{min})/2, \tag{5.8}$$

where T_{max} and T_{min} are the upper and lower limits on kinetic energy, and V_{min} is the minimum potential energy. Eqn. 5.6 is then rewritten as

$$e^{-\mathbf{H}\tau/\hbar} \cong e^{E_{avg}\tau/\hbar} \sum_{n=0}^{N} a_n\left(\frac{\Delta E\tau}{2\hbar}\right) T_n\left(\frac{-2[\mathbf{H} - E_{avg}]}{\Delta E}\right) \tag{5.9}$$

the multiplicative factor preceding the expansion is a phase factor resulting from the renormalization of the Hamiltonian. The expansion coefficients a_n are from modified Bessel functions, I_n,

$$a_n = (2-\delta_{0n})I_n(\Delta E\tau/2\hbar) \ , \tag{5.10}$$

and the Chebychev expansion is calculated from the recursion relation

$$T_n(\mathbf{X}) = 2\mathbf{X}\, T_{n-1}(\mathbf{X}) - T_{n-2}(\mathbf{X}) \ , \tag{5.11}$$

where $\mathbf{X} = -2(\mathbf{H}-E_{avg})/\Delta E$, $T_0(\mathbf{X}) = 1$, and $T_1(\mathbf{X}) = \mathbf{X}$. This series exponentially converges for $N > (\Delta E\tau/2\hbar)^{½}$. Since ΔE increases as the range of eigenvalues increases, more polynomials must be included for exponential convergence. Consequently, we truncate the potential and kinetic energies so that the upper limit is two times the estimated maximum eigenenergy (set to be ~20,000 cm^{-1} above the potential minimum).

Once an eigenstate has been calculated, its quality can be estimated by computing the energy dispersion[29]

$$D(\tau) = \sqrt{<\chi(\tau)\,|\,\mathbf{H}^2\,|\,\chi(\tau)> - <\chi(\tau)\,|\,\mathbf{H}\,|\,\chi(\tau)>^2} \tag{5.12}$$

which equals zero for a pure eigenstate.

We first employ the Chebychev propagation to calculate the vibrational eigenstates at a Cl-H_2O separation of 7.94 Å, i.e., in a region where coupling caused by the Cl atom among vibrational states of water should be negligible. Eigenstates from both the Cl + H_2O and HCl + OH wells are included. Subsequently, we incrementally vary the Cl-H_2O distance from 7.94 to 2.12 Å on a uniform spatial grid of 512 points in R. For efficient convergence, we use the eigenstate calculated at the previous R as the initial guess for the calculation at the next R. The convergence of these eigenstates is verified for each R to approach machine precision (limited from 16 digits to 8 digits by the square root in Eqn. 5.12), with $D < 0.008$ cm^{-1}. This process generates adiabatic potential curves as a function of R, with one curve for each vibrational wavefunction. These vibrational potential energy surfaces, $E_n(R)$, thus govern the Cl-H_2O intramolecular motion. In additional calculations, similar surfaces are obtained for Cl + D_2O and Cl + HOD on the same Cl + H_2O potential surface, i.e., varying only the mass of the isotope.

5.2.2. Adiabatic coupling terms

To calculate the coupling elements between adiabatic curves, an assumption of separate timescales for vibrational and nuclear motion is no longer valid. Thus, terms involving the derivative of the vibrational motion with respect to the nuclear coordinate must be added back into the nuclear Schrödinger equation given in Eqn. 5.3, which can now be written as[30]

$$\begin{aligned}&\left[\frac{-\hbar^2}{2\mu_{\mathrm{Cl-HOH}}}\frac{\partial^2}{\partial \mathrm{R}^2}+\mathrm{E}_{\mathrm{n}}(\mathrm{R})-\mathrm{E}\right]\psi_{\mathrm{n}}(\mathrm{R})=\\&\sum_{\mathrm{m}}\left[\tau_{\mathrm{nm}}(\mathrm{R})\frac{\partial}{\partial \mathrm{R}}+\rho_{\mathrm{nm}}(\mathrm{R})\right]\psi_{\mathrm{m}}(\mathrm{R})\quad ,\end{aligned}\tag{5.13}$$

where $\mathrm{E}_{\mathrm{n}}(\mathrm{R})$ is an adiabatic vibrational potential energy surface calculated as above, E is the total energy of the system, and τ_{nm} and ρ_{nm} are the coupling terms

$$\tau_{\mathrm{nm}}(\mathrm{R})=\frac{\hbar^2}{\mu_{\mathrm{Cl-HOH}}}\left\langle\chi_{\mathrm{n}}\left|\frac{\partial}{\partial \mathrm{R}}\right|\chi_{\mathrm{m}}\right\rangle\tag{5.14}$$

$$\rho_{\mathrm{nm}}(\mathrm{R})=\frac{\hbar^2}{2\mu_{\mathrm{Cl-HOH}}}\left\langle\chi_{\mathrm{n}}\left|\frac{\partial^2}{\partial \mathrm{R}^2}\right|\chi_{\mathrm{m}}\right\rangle\quad .\tag{5.15}$$

Operationally, we follow the method of Tuvi and Band[31] to symmetrize these coupling terms to preserve the hermiticity of the Hamiltonian. This process requires rewriting the Schrödinger equation as

$$\begin{aligned}&\left[\frac{-\hbar^2}{2\mu_{\mathrm{Cl-HOH}}}\frac{\partial^2}{\partial \mathrm{R}^2}+\mathrm{E}_{\mathrm{n}}(\mathrm{R})-\mathrm{E}\right]\psi_{\mathrm{n}}(\mathrm{R})=\\&\sum_{\mathrm{m}}\left[\tau_{\mathrm{nm}}(\mathrm{R})\frac{\partial}{\partial \mathrm{R}}+\frac{\partial}{\partial \mathrm{R}}\tau_{\mathrm{nm}}(\mathrm{R})+\tilde{\rho}_{\mathrm{nm}}(\mathrm{R})\right]\psi_{\mathrm{m}}(\mathrm{R})\end{aligned}\tag{5.16}$$

where

$$\begin{aligned}\tilde{\rho}_{\mathrm{nm}}(\mathrm{R})&=\rho_{\mathrm{nm}}(\mathrm{R})-\frac{\partial}{\partial \mathrm{R}}\left[\tau_{\mathrm{nm}}(\mathrm{R})\right]\\&=\frac{-\hbar^2}{2\mu_{\mathrm{Cl-HOH}}}\left\langle\frac{\partial}{\partial \mathrm{R}}\chi_{\mathrm{n}}\left|\frac{\partial}{\partial \mathrm{R}}\chi_{\mathrm{m}}\right.\right\rangle\end{aligned}\tag{5.17}$$

Equation 5.16 is analytically equivalent to 5.13; however, all derivatives of the vibrational eigenfunctions with respect to R in τ_{nm} and $\tilde{\rho}_{nm}$ are now first derivatives, facilitating numerical computation. We calculate these derivatives to second order, additionally taking advantage of the hermiticity of $\tilde{\rho}_{nm}$ and anti-hermiticity of τ_{nm} to average each element with its transpose or the complex conjugate of its transpose, respectively.

In addition to using the coupling terms for calculating the wavepacket dynamics, we can estimate relative curve-crossing velocities in the following way. The most significant coupling term is typically τ_{nm}; as described by Child,[30] $\partial/\partial R$ is related to the momentum operator, such that $|\tau_{nm}\partial/\partial R|$ is related semiclassically to equal $|\mu_{Cl-HOH} v_{rel}(R)/\hbar|$, where $v_{rel}(R)$ is the relative Cl-H_2O velocity at a given R. $|\tau_{nm}\partial/\partial R|$ becomes most significant as it approaches the magnitude of the energy spacings between nearest adiabats, i.e., $|E_n(R)-E_m(R)|$. We can thus *estimate* the characteristic transition velocity by setting these two terms equal to each other and solving for $v_{rel}(R)$ to obtain a characteristic transition velocity, $v_{nm}(R)$:

$$v_{nm}(R) = \frac{|E_m(R) - E_n(R)|}{\left\langle \chi_n \left| \frac{\partial}{\partial R} \right| \chi_m \right\rangle} \tag{5.18}$$

$v_{nm}(R)$ is thus the characteristic v_{rel} for the transition between the n^th and m^th adiabats, similar to a Landau-Zener velocity for crossing between diabats; its minima (i.e., the most likely crossing points) occur at values of R corresponding to avoided crossings between adiabats. At relative Cl-H_2O velocities smaller than the minimum in $v_{nm}(R)$

at a crossing region, we would thus expect the system to proceed adiabatically. Correspondingly, these velocities should aid in our predictions for the curve-crossing dynamics.

5.2.3. Wavepacket propagation

The final step in this process is determining how the choice of initial H_2O vibrational state and relative Cl-H_2O velocity influence the dynamics of the Cl + H_2O collision by performing time-dependent wavepacket scattering calculations. In brief, our approach is to begin a Gaussian wavepacket on one of the adiabats at a large Cl-H_2O separation and propagate forward in real time, using a Chebychev expansion of the propagation operator. When the wavepacket reaches the Cl-H_2O interaction region, the coupling terms between the adiabats allow for transfer of probability to other states. The flux in each output channel is calculated as the wavepacket exits the interaction region to determine the relative amounts of each product state. After the region of flux calculation, an appropriately scaled damping operator is placed on each of the output channels so that the wavefunction does not reflect or transmit at the end of the grid. The details of this phase of the computation are given below.

The time-dependent technique resembles time-independent methods by permitting determination of the branching ratios among elastic, inelastic and reactive scattering channels after the wavepacket has entered and exited the interaction region. Unlike time-independent methods, this technique has the important advantage of following the flow of probability among channels as a function of time to determine how the wavepacket makes transitions at crossing regions. The disadvantage of this technique is that rather than providing monoenergetic scattering probabilities, the wavepacket must (by the Heisenberg uncertainty principle) contain some spread in momentum. While the energy-dependent scattering can nevertheless technically be recovered, it requires calculating the outgoing flux for extended periods of time (i.e., without damping). For our purposes, this difficulty can more simply be overcome by making the wavepacket appropriately broad in coordinate space and thus narrow in momentum space. Thus, the initial conditions for the wavepacket propagation are selected in the following way.

For each of the three reaction systems, the initial Gaussian wavepackets have center momenta at a near-thermal velocity, with additional momenta explored for Cl + H_2O. For Cl + H_2O, Cl + D_2O, and Cl + HOD, initial momenta are 10.0, 10.4, and 10.2 au, respectively, scaled to have equivalent kinetic energy in all three collision systems. The additional momenta selected for Cl + H_2O are 15.0 and 20.0 au; thus, the three Cl + H_2O momenta correspond to relative energies of 510, 1100, and 2000 cm^{-1} and speeds of 101,000, 152,000, and 202,000 cm/s (for comparison, the mean relative speed of Cl and H_2O at 300 K is 73,000 cm/s). The spatial extent of all wavepackets is chosen to be 0.26 Å; for Cl + H_2O, the Gaussian width in momentum space ($\Delta p = 2.0$ au) is less than the spacing between the three momenta (5.0 au). These wavepackets are then centered at R = 6.9 Å, away from the interaction region. Convergence of the calculation with respect to this choice of distance is explicitly verified for each momentum and mass combination by comparison with the output flux from wavepackets begun at 6.35 Å; the flux in each channel varies by $\leq 1\%$ of its own value.

As with the eigenfunction relaxation method described above, a Chebychev expansion is used for the propagation operator. However, since the wavepacket propagation is in real time, the expansion is modified in this way:

$$e^{-i\mathbf{H}\tau/\hbar} \cong e^{iE_{avg}t/\hbar} \sum_{n=0}^{N} a_n\left(\frac{\Delta Et}{2\hbar}\right) \phi_n\left(\frac{-2[\mathbf{H} - E_{avg}]}{\Delta E}\right) \qquad (5.19)$$

where the ϕ_n are imaginary Chebychev polynomials defined on [-i,i]. The expansion coefficients, a_n, are calculated from Bessel functions, J_n, via[26]

$$a_n = (2-\delta_{0n})i^n J_n(\Delta Et/2\hbar) \qquad (5.20)$$

The recursion relation for the Chebychev polynomials is similar to the one given in Eqn. 5.11, with modifications for damping out the wavefunction in the exit channel described below; however, this expansion converges exponentially for $N > (\Delta E\tau/2\hbar)$ (note the lack of square root). The Chebychev propagator preserves the norm of the wavepacket, and in principle, the timestep can be of unlimited size, at the cost of additional terms in the expansion. However, in order to be able to monitor the flux and observe the wavepacket propagation, the timestep is chosen to be 12.5 fs; correspondingly, the typical size of the Chebychev expansion is on the order of 300-400 polynomials. With this expansion, preservation of the total norm of the wavepacket is verified to be better than one part in 10^8 per timestep, with approximately 100 timesteps required for each propagation.

After the wavefunction exits the interaction region, the flux out of each exit channel is averaged over a series of points prior to the absorbing boundary. The accumulated flux at each point in a given channel is thus obtained from[32]

$$\mathrm{F} = \sum_{\Delta \mathrm{t}} \mathrm{J(t)}\Delta \mathrm{t} = \frac{\Delta \mathrm{t}}{\mu_{\mathrm{Cl-HOH}}} \sum_{\Lambda \mathrm{t}} \mathrm{Re}\left[\psi^{*}(\mathrm{R},\mathrm{t}) \frac{\hbar}{i} \frac{\partial}{\partial \mathrm{R}} \psi(\mathrm{R},\mathrm{t}) \right] \quad , \qquad (5.21)$$

where Δt is the size of the timestep. Since the initial norm of the wavepacket equals 1, the accumulated flux summed over all channels should also equal 1; we thus explicit verify that this accumulated flux agrees to $\leq$ 1% with the wavepacket probability lost by the end of the calculation.

After the wavepacket passes through the region in which the flux is calculated, a damping operator is applied at each time propagation step to absorb the wavepacket, preventing reflection from or transmission through the end of the grid. Following Mandelshtam and Taylor,[33,34] this damping operator has the form

$$e^{-\gamma(R)}, \qquad (5.22)$$

where

$$\begin{aligned} \gamma(\mathrm{R}) &= \mathrm{c}(\mathrm{R}-\mathrm{R}_0)/(\mathrm{R}_{\mathrm{max}}-\mathrm{R}_0), \ \ \mathrm{R} \geq \mathrm{R}_0 \\ &= 0, \ \mathrm{R} < \mathrm{R}_0 \qquad (5.23) \end{aligned}$$

with R_{max} equal to the largest Cl-H_2O radius (7.94 Å), and c and R_0 as adjustable parameters such that the damping operator decreases from $\exp\{-\gamma(R_0)\} = 1$ to $\exp\{-\gamma(R_{max})] = \exp(-c)$. The operator is incorporated into the Chebychev expansion of the propagation operator by

$$\phi_n(\mathbf{X}) = e^{-\gamma(R)}[2\mathbf{X}\phi_{n-1}(\mathbf{X}) - e^{-\gamma(R)}\phi_{n-2}(\mathbf{X})], \qquad (5.24)$$

where $\mathbf{X} = -2(\mathbf{H}-E_{avg})/\Delta E$, $\phi_0(\mathbf{X}) = 1$, and $\phi_1(\mathbf{X}) = \exp\{-\gamma(R)\}\mathbf{X}$. The operator thus acts on the wavepacket via multiplication by $\exp\{-\gamma(R)\}$ in the region $[R_0,R_{max}]$.

We determine the optimal parameters for this operator by fixing R_0 such that $(R_{max} - R_0) = 1.32$ Å, i.e., significantly larger than the deBroglie wavelength of the lowest input momentum (for p = 10 au, $\lambda_{deBroglie} = 0.32$ Å), and varying c. Trial wavepackets with one center momentum are propagated towards this absorbing boundary on a single potential curve (with all couplings turned off); c is optimized by minimizing the survival probability for this wavepacket (i.e., reflection plus transmission). This procedure is repeated for a range of center momenta; in all cases, the survival probability is robustly insensitive to ~20-30% changes in c. Accordingly, the optimal choice of c for any center momentum can be estimated from a quadratic least-squares fit of these data points. The parameters from this least-squares fit are given in Table 5.2.

Table 5.2. Table of parameters from quadratic fit of optimal damping parameters, c, for Cl + H_2O: c = Ax^2+Bx+C.

	Parameter
A	1.47E-6
B	9.23E-4
C	3.46E-3

To dampen the elastically scattered output wavepacket, the c parameter used corresponds to the initial center momentum. However, the portions of the wavepacket that make transitions to other states (via the adiabatic coupling terms), will not have the same center momentum. Rather, the kinetic energy of the fraction of the wavepacket on a different output channel should approximately equal the input channel kinetic energy *plus* the difference in the asymptotic potential energies of the two states. Based on this difference, the output momentum on any other state can be estimated and the damping parameters selected accordingly. In addition, since the wavepackets are typically started near the damping region, the damping operator is initially fixed to 1 (i.e., no damping) across its entire range for sufficient time (typically 250-500 fs) for the wavepacket to propagate out of that region.

5.3 Results

The results of these calculations are divided into two parts. In Section 5.3.1, we examine the static picture, i.e., the vibrational eigenstates calculated as a function of R, the resulting adiabatic potential curves, and the couplings between these curves, focusing on developing predictions for the subsequent dynamics calculations. In

Section 5.3.2, we discuss the wavepacket propagation on these potential curves, determining how the dynamics proceed and how the initial vibrational state influences the subsequent dynamics. In these, we primarily focus on the results for Cl + H_2O, comparing with Cl + D_2O and Cl + HOD when appropriate.

5.3.1. Vibrational eigenfunctions, adiabats, and coupling elements

As described in Section 5.2.2, we have calculated the H_2O and OH/HCl vibrational eigenfunctions as a function of parametric Cl + H_2O distance. We first calculate the asymptotic eigenfunctions (i.e., at large Cl-H_2O separation), including eigenstates up to the sixth excited state, to serve as an initial basis for our subsequent parametric variation of R. The eigenenergies calculated at each step in R thus generate the adiabatic potential curves for Cl + H_2O shown in Fig. 5.2.

We can determine the states represented by adiabatic curves by examining the asymptotic eigenstates, which can then used to label each of the curves. These eigenstates encompass the ground vibrational state, the lowest (v=1) stretching manifold in Cl + H_2O and OH + HCl, and the next excited state (corresponding to HCl(v=2) + OH(v=0) asymptotically) to ensure the availability of a higher energy output channel. These adiabatic curves by definition always follow the lowest seven eigenstates; thus, these labels may not accurately represent the nature of the wavefunction in the Cl + H_2O interaction region. However, asymptotically, the fourth excited state corresponds to the symmetric stretch of water, and the fifth excited state, the antisymmetric stretch; the adiabats corresponding to these states will thus serve as the input channels for the dynamics calculations.

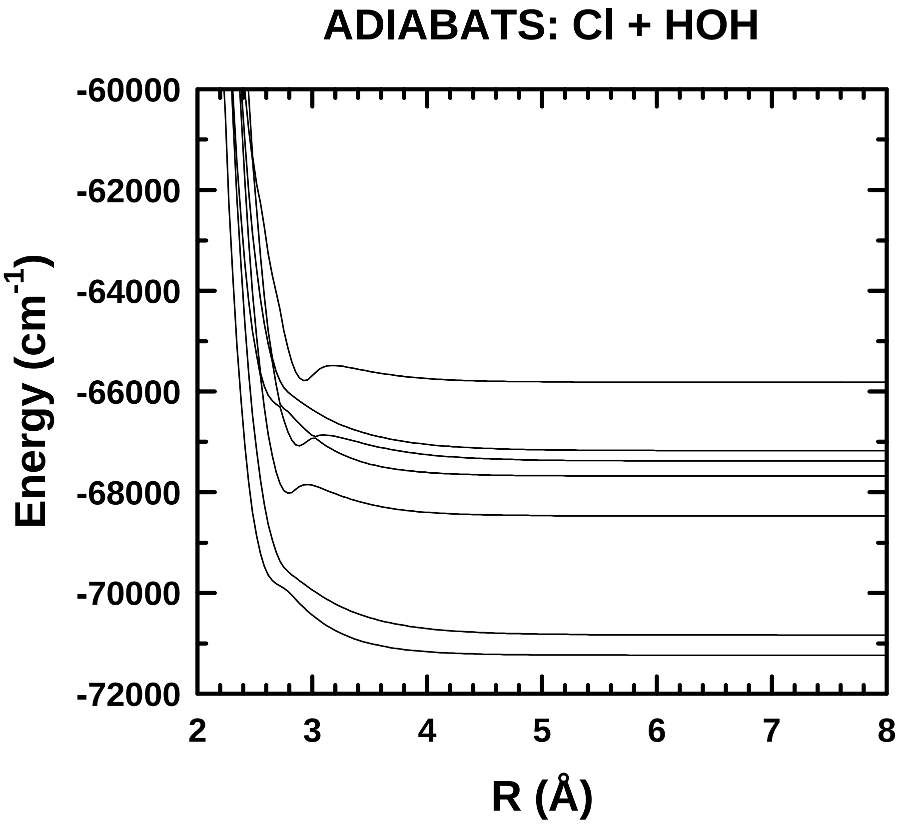

Figure 5.2. Adiabatic potential energy curves for Cl + HOH reactive scattering, generated by calculating the H_2O and OH/HCl vibrational eigenfunctions as a function of parametric R. Asymptotic eigenfunctions (at large Cl-HOH separation) serve as an initial basis for the parametric variation.

As seen in Fig. 5.2, the adiabats begin to vary in energy as R approaches 3.5 Å, indicating that they have reached the region where the couplings among various states should become quite significant. Accordingly, we re-examine the character of the vibrational eigenstates in this region. In Fig. 5.3a-d, we focus in particular on the symmetric and antisymmetric stretch eigenstates at two Cl-H_2O distances: outside the interaction region (R = 4.23 Å, Fig. 5.3a-b), where the eigenstates resemble the asymptotic eigenstates, and near the interaction region (R = 2.8 Å, Fig. 5.3c-d). As mentioned previously, the "proximal" OH bond, r_1, points toward the Cl, the "distal" bond, r_2, is on the opposite side of the molecule; thus, eigenstates at short r_1 correspond to Cl + H_2O states, and at long r_1, to HCl + OH states.

Intriguingly, the eigenfunction that corresponds asymptotically to the symmetric stretch (Cl + H_2O(s=1), the fourth excited state) becomes directed primarily along the *proximal* OH bond (r_1) with the Cl approach, i.e., it has rotated *toward* the Cl. Thus, the vibrational excitation is now pointed toward the reactive atom. In contrast, the antisymmetric stretch (Cl + H_2O(a=1), the fifth excited state) rotates to localize primarily along the *distal* OH bond (r_2), i.e., away from the reactive Cl atom. Thus, the approach of the Cl atom breaks the symmetry of the potential to convert *normal*-mode states into *local*-mode stretches. The localization of the symmetric stretch excitation toward the Cl might lead us to predict this state to be more reactive than the antisymmetric stretch. To further explore how the changing character of these eigenstates will affect reactivity, we next examine the adiabatic curves in more detail, looking at all three systems studied (Cl + H_2O/D_2O/HOD).

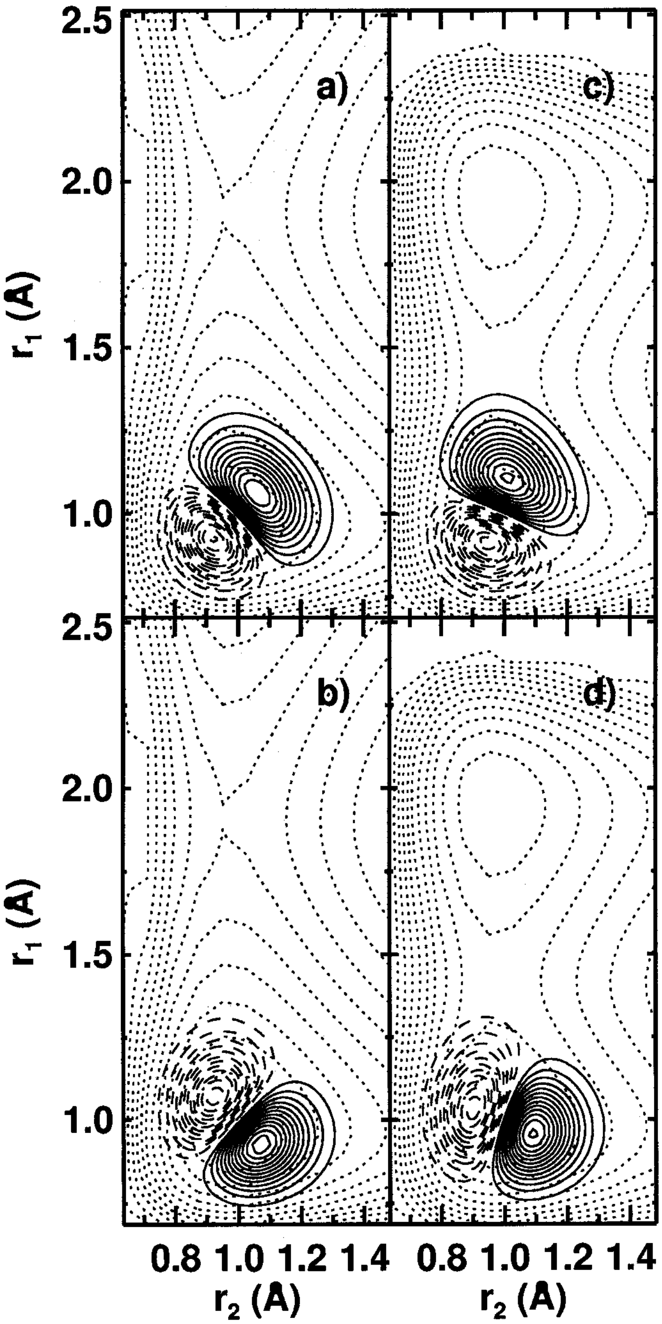

Figure 5.3. Fourth and fifth excited-state vibrational eigenfunctions for Cl + HOH outside the interaction region (R = 4.23 Å, Fig. 5.3a and b, respectively) and near the interaction region (R = 2.8 Å, Fig. 5.3c and d, respectively). The fourth excited-state eigenfunction, which corresponds asymptotically to the symmetric stretch (5.3a), becomes directed primarily along the *proximal* OH bond (r_1) with Cl approach (5.3c), so that the vibrational excitation points toward the reactive atom. In contrast, the fifth excited-state wavefunction, which corresponds asymptotically to the antisymmetric stretch (5.3b), rotates to localize primarily along the *distal* OH bond (r_2) (5.3d).

Figure 5.4a-c contains plots of the adiabats in the interaction region for these three systems, with the corresponding asymptotic states labeled (although not shown here, all curves are calculated to R = 7.94 Å for use in the dynamics calculations). Avoided crossings are numbered, with the characteristic minimum velocity for each crossing (calculated from Eqn. 5.18) given in Table 5.3. For convenience, the classical turning points for the low (designated p_{lo}, momentum = 10 au, $v_{rel} \sim 1\times10^5$ cm/s) and high (p_{hi} = 20 au, $v_{rel} \sim 2\times10^5$ cm/s) momenta used in subsequent dynamics calculations are also designated. First, we focus on the general shape and trends in the curves, as well as discussing the locations of the turning points for the lowest momentum relative to the interaction region.

For Cl + H_2O (Fig. 5.4a), there are numerous avoided crossings between states; thus, it is not surprising that the character of the adiabatic wavefunctions changes dramatically. Notably, since the symmetric stretch on this surface is ~200 cm^{-1} lower in energy than the antisymmetric stretch, it is correspondingly closer in energy to the HCl + OH product states in the v=1 manifold. In addition, the symmetric stretch also becomes even closer in energy to the ground state with decreasing R, resulting in two narrowly avoided crossings between s=1 and OH(v=1) + HCl(v=0) in the region of R = 3.0 and 2.7 Å; this behavior is not exhibited by the antisymmetric stretch adiabat.

By examining the avoided crossings in more detail, we can predict the accessibility of each transition based on its characteristic velocity and distance from the classical turning point of the central wavepacket velocity. Nearly all of the avoided crossings for Cl + H_2O have lower characteristic crossing velocities than

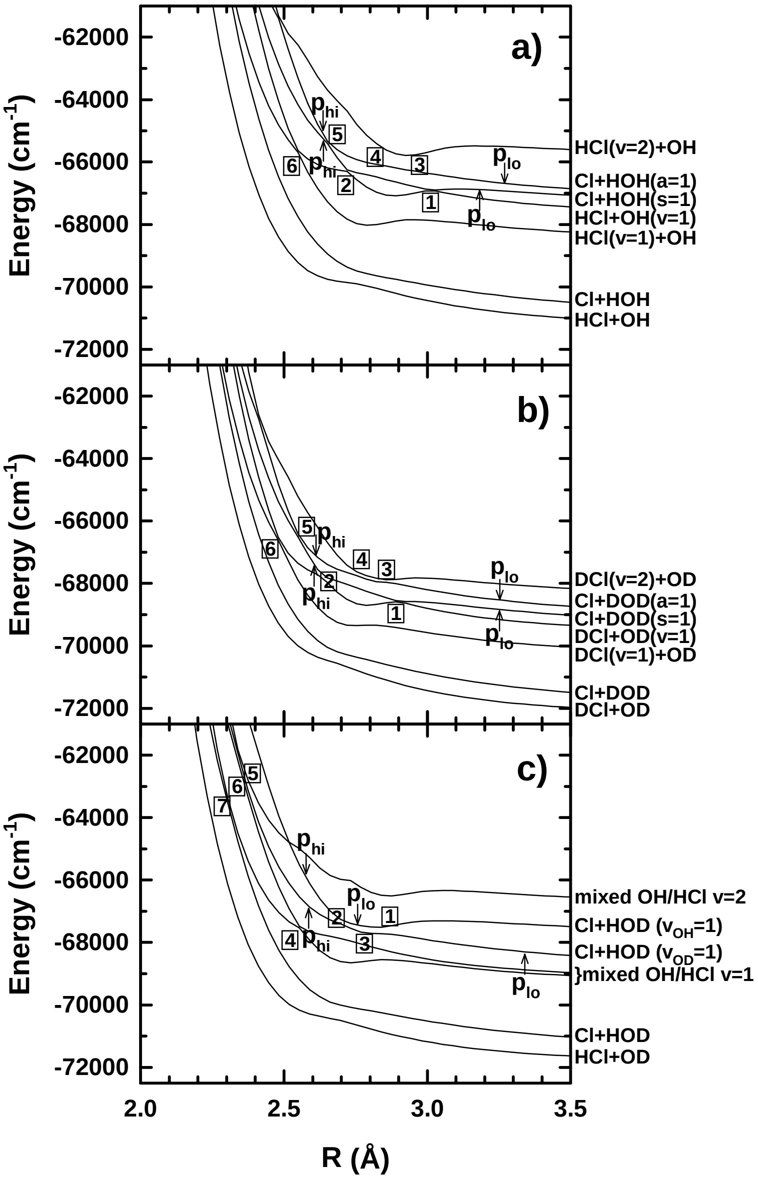

Figure 5.4. Adiabatic potential energy curves for a) Cl + HOH, b) Cl + DOD, and c) Cl + HOD near the interaction region. Each number designates an avoided crossing between two curves, with the characteristic velocities (calculated from Eqn. 5.16) given in Table 5.3. The asymptotic eigenstates to which each curve corresponds are shown on the right side of the figure. For convenience, the arrows designate classical turning points for the low (designated p_{lo}, momentum = 10 au, $v_{rel} \sim 1\times10^5$ cm/s) and high (p_{hi} = 20 au, $v_{rel} \sim 2\times10^5$ cm/s) momenta used in subsequent dynamics calculations on the fourth and fifth excited states.

Table 5.3. v_{nm}, curve-crossing velocities from Eqn. 5.16, in cm/s (see Fig. 5.4a-c for designation of crossing points).

Crossing	Cl + HOH	Cl + DOD	Cl + HOD
1	<50	100	42,000
2	800	2300	16,000
3	>1E6	9000	180,000
4	>1E6	18,000	2000
5	3200	5600	6000
6	1000	2500	22,000
7			15,000

the asymptotic value of the central velocity (see Table 5.3). However, the classical turning points for the p = 10 au wavepacket occur *before* the primary interaction region, thus only the leading fringes of the wavepacket in momentum space will reach those crossings. The strongest coupling links s=1 to OH(v=1) + HCl(v=0), with the first crossing between these states occurring just outside the reach of the central wavepacket velocity; from this, we would expect some possibility of reaction from s=1. In contrast, the only apparent reactive path for the a=1 state requires two transitions, first crossing near R = 2.6 Å into the symmetric stretch, then crossing through one (not both) of the avoided crossings between this state and OH(v=1). In light of these differences, the symmetric stretch should be the more reactive mode at low collision velocities because it ultimately places the vibrational excitation along the reaction coordinate and thus couples into product states.

For the Cl + D_2O adiabats (Fig. 5.4b), a picture emerges with subtle yet important differences. While the adiabatic potential curves have the same general shapes as those of Cl + H_2O, the curve-crossing velocities are generally 2-3 times higher (see Table 5.3). These velocities reflects the larger energy separations between neighboring states in the same stretch manifold (e.g., the asymptotic energy difference for s=1 and a=1 is 287 cm^{-1} versus 204 cm^{-1} for H_2O), and slightly smaller coupling terms (i.e., the wavefunctions vary more slowly with R). The major exception to this observation is the coupling to the DCl(v=2) state. The heavier mass of D versus H lowers the DCl(v=2) stretch relative to the v=1 manifold so that it approaches the antisymmetric stretch; consequently, the coupling velocities between the antisymmetric stretch and DCl(v=2) are approximately two orders of magnitude *smaller* than the equivalent velocities for H_2O. For this reason, we might expect to see an increase in the reactive scattering relative to inelastic scattering from Cl + D_2O over Cl + H_2O. In general, however, the velocity turning points on a=1 and s=1 in Cl + D_2O are further away from the interaction region, because 1) they occur at larger R, and 2) the crossing points among curves occur at smaller R. Consequently, the overall reactive and inelastic scattering for D_2O should be less than H_2O at the same energy.

For Cl + HOD (with the Cl approaching from the H side of the molecule), the adiabatic curves no longer resemble those of H_2O/D_2O and as such should produce substantially different dynamics. One important distinction between HOD and H_2O/D_2O is that the asymptotic product states in HOD do not correspond to localized vibration in HCl or OD and are simply designated by their total vibrational quanta.

Although they cannot be treated as uncoupled product states, this designation allows for distinguishing among elastic, inelastic, and reactive scattering. Of the two input stretches (v_{OD} and v_{OH}), the v_{OD} is lower in energy and thus closer to the product states below. However, the approaching Cl atom lowers the energy of v_{OH} (relative to the ground state) because the path of the Cl lies along the OH bond. As a result, the classical turning point for v_{OH} (p_{lo}) is much further into the interaction region than the turning points for either stretch in H_2O, and crossings with other states are more accessible. Correspondingly, we expect the total product in Cl + HOD to be larger than in Cl + H_2O for the low-momentum wavepacket.

For further comparison of Cl + HOD with Cl + H_2O, we examine the wavefunctions at the approach to the interaction region (see Fig. 5.5a-b). First, at the same R = 4.23 Å as examined for Cl + H_2O (i.e., corresponding to the asymptotic wavefunctions), the symmetric and antisymmetric stretches seen for Cl + H_2O are instead local-mode OH and OD stretches. While the symmetric stretch of H_2O rotates towards the Cl as it approaches, the OH stretch is localized towards the Cl axis for the entire approach of the reactive atom. However, the OH and OD stretches are not completely uncoupled. The adiabats demonstrate a very strong avoided crossing between these two states at R = 2.8 Å, indicating that the nature of the adiabatic wavefunctions changes rapidly with R. Accordingly, at that Cl-HOD distance, we have examined the fourth and fifth excited state wavefunctions (Fig. 5.5c-d), which correspond asymptotically to $v_{OD} = 1$ and $v_{OH} = 1$, respectively. Intriguingly, the character of the wavefunctions nearly *reverses* at this point: while both have probability in the product well, the fourth state resembles $v_{OH} = 1$ in the reactant well,

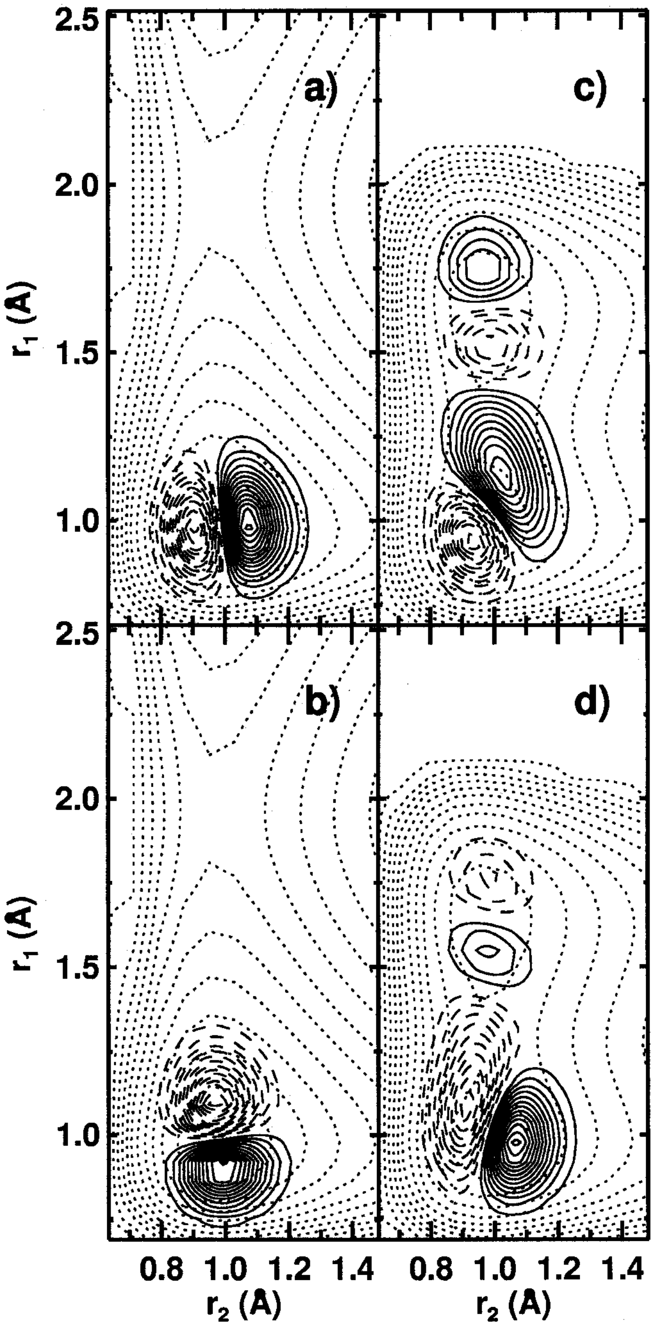

Figure 5.5. Fourth and fifth excited-state vibrational eigenfunctions for Cl + HOD outside the interaction region (R = 4.23 Å, Fig. 5.5a and b, respectively) and near a very strongly avoided crossing (R = 2.8 Å, Fig. 5.5c and d, respectively). The asymptotic eigenfunctions correspond to local-mode OH (Fig. 5.3a) and OD (Fig. 5.5b) stretches. However, at the strongly avoided crossing, the character of the wavefunctions nearly *reverses*: in the reactant well, the fourth state (Fig. 5.5c) resembles v_{OH} = 1, while the fifth state (Fig. 5.5d) resembles v_{OD} = 1.

while the fifth state resembles $v_{OD} = 1$. Correspondingly, we might expect some transfer between those states, with greater transfer from $v_{OH} = 1$ to $v_{OD} = 1$ because v_{OH} is higher in energy.

5.3.2. Cl + H_2O/D_2O/HOD wavepacket propagation

Having calculated the vibrationally adiabatic potential energy curves and the coupling elements between those curves, we probe the dynamics by propagating wavepackets on each incoming state of interest. As detailed in Section 5.2.3, Gaussian wavepackets at relative velocities of approximately 10,000, 15,000, and 20,000 cm/s are employed to explore the dynamics and branching ratios among elastic, inelastic, and reactive scattering. This analysis focuses first on Cl + H_2O dynamics, primarily at the lowest collision energy, then on additional energies and collision systems.

We first examine a sample wavepacket propagation into the Cl + H_2O interaction region, monitoring transfer into other channels. Figure 5.6a follows the course of a wavepacket initiated on the Cl + H_2O(a=1) state, with t = 0 at the bottom of the graph and each step higher indicating an additional 100-fs step. Most noticeably, the majority of the wavepacket probability remains on this curve for the duration of the interaction region, disappearing only when it is absorbed at the end of the grid by the damping operator. Thus, the dominant output channel is elastic collision between Cl and the antisymmetric stretch of H_2O with no effect on the vibrational eigenstate.

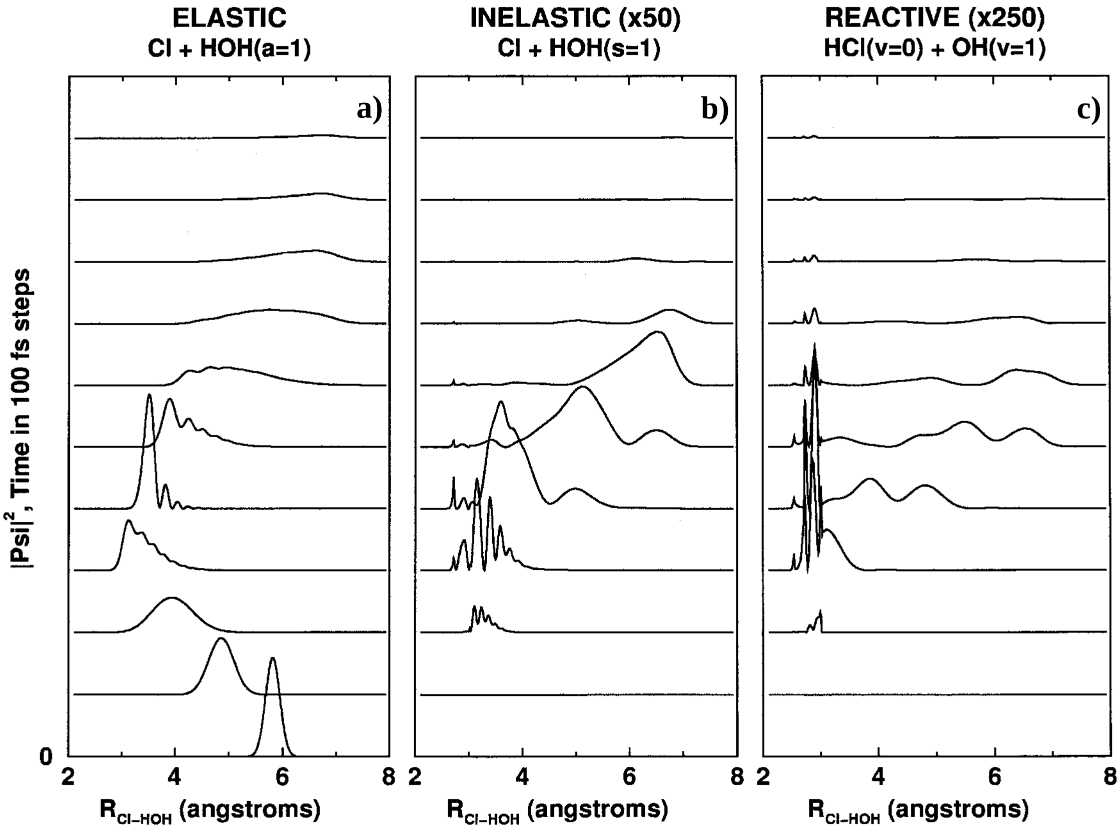

Figure 5.6. Sample wavepacket propagation for Cl + H_2O(a=1), monitoring the scattering into a) Cl + HOH(a=1), b) Cl + HOH(s=1), and c) HCl(v=0) + OH(v=1). The initial wavepacket is given at the bottom of the graph; each incremental step higher indicates an additional 100-fs step. For visual clarity, the wavepackets in 5.6b and c are increased in amplitude by factors of 50 and 250, respectively, relative to 5.6a. Most of the wavepacket probability remains in the elastic Cl + HOH(a=1) state; however, this sufficiently couples with other states to transfer probability into inelastic (5.6b) and reactive (5.6b) scattering.

While this vibrationally adiabatic picture describes the majority of the reaction probability for Cl + H_2O(a=1) at this low collision energy, the wavepacket experiences some coupling with other states, with a small amount of transfer to other curves. For example, Fig. 5.6b demonstrates the growth of probability on the Cl + H_2O(s=1) state, with the magnitude increased by 50 times relative to the elastically scattered wavepacket for visual clarity. This figure illustrates that as the initial wavepacket reaches the potential well, the state that asymptotically correlates to the *antisymmetric* stretch sufficiently couples to the asymptotic *symmetric* stretch state to produce a redistribution of vibrational energy. Similarly, Fig. 5.6c shows the transfer of probability to the reactive HCl(v=0) + OH(v=1) state, magnified by a factor of 250. Interestingly, at this energy, vibrational redistribution (Fig. 5.6b) is more likely to occur than chemical reaction (Fig 5.6c). While these pictures do not provide quantitative information about the product distributions, they do provide a first glimpse into the dynamics of this system.

In order to provide quantitative determinations of probability in each exit channel, the fluxes as a function of time are monitored as described in Sect. 5.2, terminating when the remaining wavepacket probability is less than 0.01. Fig. 5.7a-b gives the accumulated fluxes versus time for the p = 10 au calculations of Cl + H_2O(s=1) and Cl + H_2O(a=1), respectively. Both figures demonstrate that these are predominantly direct reactions, i.e., without long-lived resonance states; the near-exponential rise in flux likely results from the spread in the Gaussian wavepacket. Notably, this direct behavior is similar among all input states and momenta calculated for each of the water isotopes. In addition, for both states of Cl + H_2O at this input

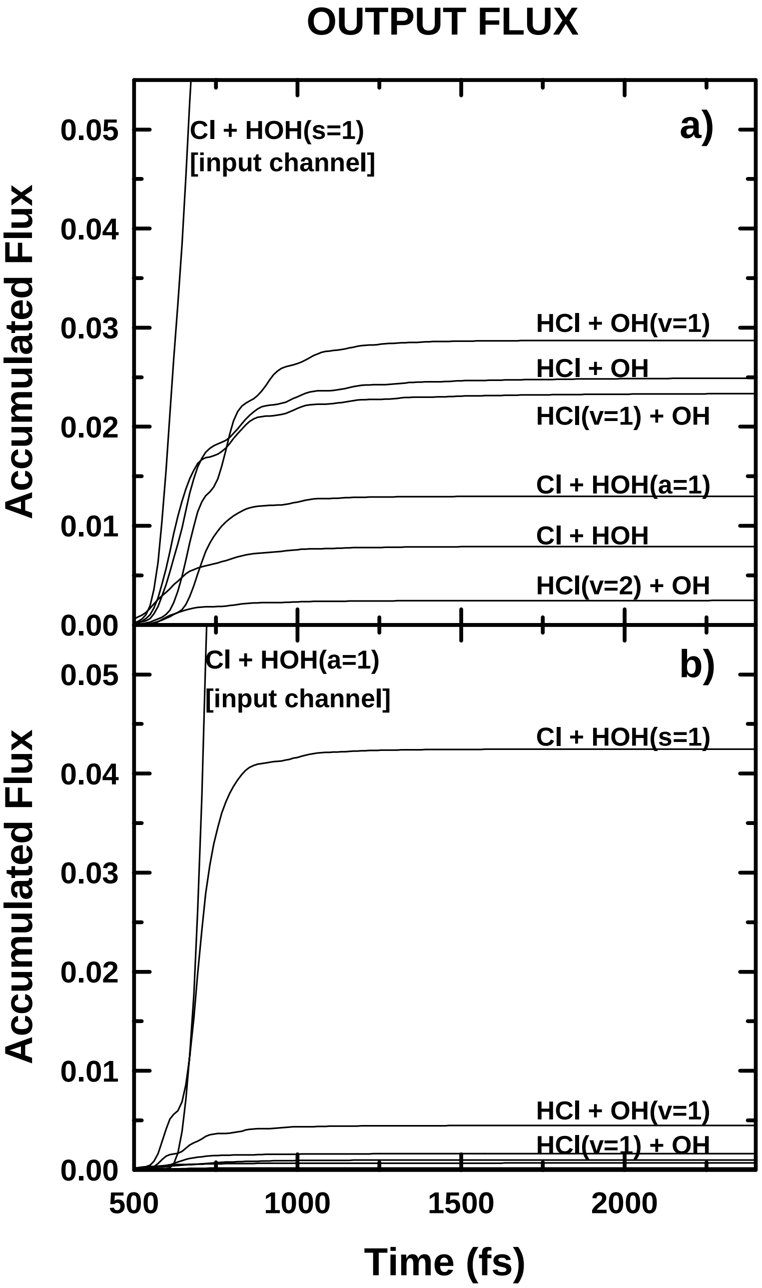

Figure 5.7. Accumulated fluxes versus time for the scattering from a) Cl + H_2O(s=1) and b) Cl + H_2O(a=1) for p = 10 au (510 cm^{-1} collision energy, and 101,000 cm/s relative Cl-H_2O speeds). These plots indicate that at these energies, the interactions are predominantly elastic (i.e., >90% probability of exiting on the entrance channel). Of the remaining channels, reaction dominates over inelastic scattering from H_2O(s=1) to H_2O(a=1) (Fig. 5.7a); in contrast, inelastic scattering from H_2O(a=1) to H_2O(s=1) dominates over reaction (Fig. 5.7b).

momentum, the elastic channel dominates, with a total probability near 0.95 of exiting on the input channel. Among those channels which alter Cl + H_2O state, reactive channels dominate over inelastic scattering from H_2O(s=1) to H_2O(a=1) (Fig. 5.7a); in contrast, inelastic scattering from H_2O(a=1) to H_2O(s=1) dominates over reactive scattering (Fig. 5.7b). Thus, as predicted from the adiabatic potentials, the symmetric stretch is more reactive than the antisymmetric stretch of H_2O.

Monitoring the accumulated flux out of each channel in this fashion allows a comparison of the products of the Cl + H_2O reaction with the other collision systems studied, namely, Cl + D_2O and Cl + HOD (each calculated for p ~ 10 au). The flux out of each channel is summed over reactive and inelastic product states and plotted in Fig. 5.8. Overall, these data support the predictions made from the adiabatic curves, as discussed in Section 5.3.2. First, as predicted from the rotation of the symmetric stretch wavefunction toward the Cl atom, the symmetric stretches of both H_2O and D_2O are more reactive than the antisymmetric stretches. In addition, the overall amount of inelastic and reactive scattering from H_2O is larger than from D_2O, consistent with the larger coupling velocities between states of D_2O and the greater distance of the classical turning points from the interaction region. Finally, the OH vibrational excitation of HOD is the most reactive of all states of H_2O/D_2O/HOD and, indeed, is more reactive than v_{OD} by nearly an order of magnitude, consistent with a local-mode picture of this reaction.

However, two more subtle comparisons of reactive and inelastic flux warrant additional investigation. First, despite the apparent similarity in adiabatic potential curves between H_2O and D_2O, the antisymmetric stretch states of these two molecules

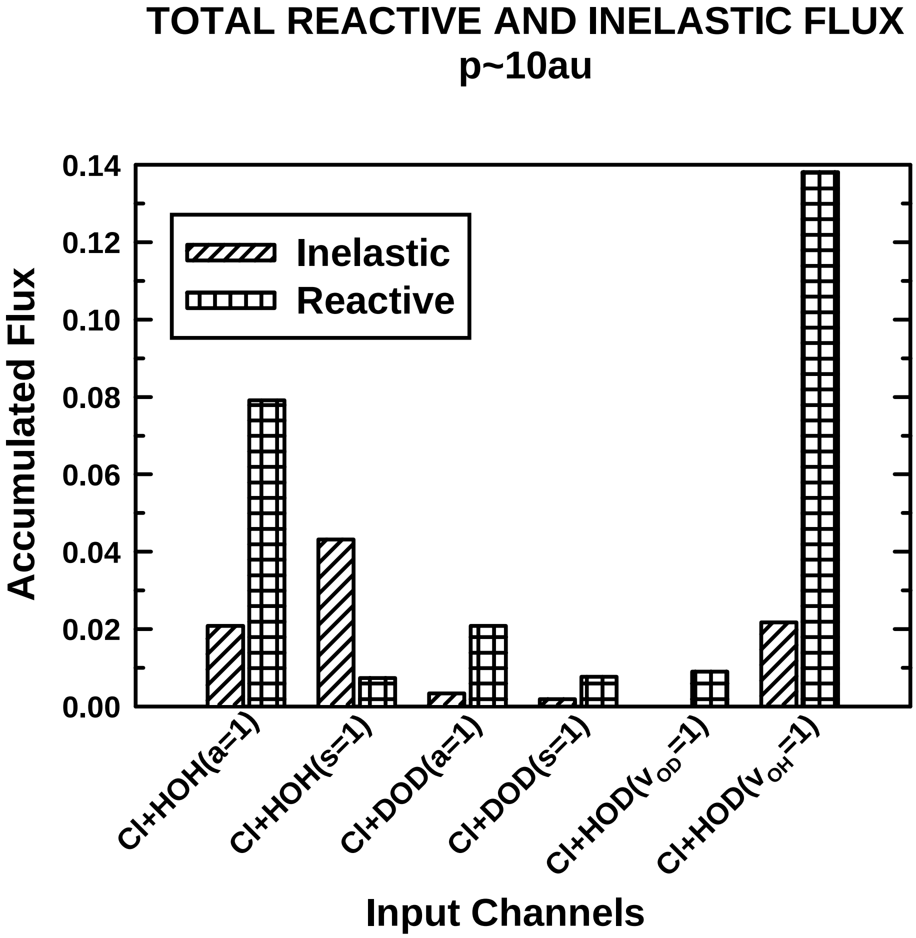

Figure 5.8. Accumulated flux for p ~ 10 au wavepackets into non-elastic channels for Cl + HOH, Cl + DOD, and Cl + HOD, summed separately over inelastic and reactive channels. The symmetric stretches of both H_2O and D_2O are more reactive than the antisymmetric stretches, with overall amount non-elastic scattering from H_2O greater than from D_2O, while the OH vibrational excitation of HOD is the most reactive state.

produce opposite relative amounts of inelastic and reactive products. Second, despite the excitation of the “wrong” bond in HOD, reactive scattering from $v_{OD} = 1$ is significantly larger than inelastic scattering. This is somewhat surprising, in part because the curve-crossing velocity with Cl + HOD(v_{OH}=1) given in Table 5.3 is *smaller* than the velocity for coupling with the highest mixed v=1 wavefunction, thus one might expect that inelastic channel to dominate.

Fortunately, time-dependent wavepacket propagation allows for monitoring of probability in each channel as a function of time, i.e., for directly observing transfers between states. Accordingly, we examine the probability in each channel as a function of time for several initial states, plotted in Fig. 5.9a-b and 5.10a-b. Importantly, the diminution of the total probability at the end of the reactive encounter results from application of the damping operator near the end of the grid.

For Cl + H_2O(s=1) and (a=1), comparisons of the dynamics can be made between Fig. 5.9a-b. For the input channel Cl + H_2O(s=1) (Fig. 5.9a), three major pathways (i.e., HCl(v=0) + OH(v=1), HCl(v=1) + OH(v=0), and Cl + H_2O(a=1)) remove probability nearly simultaneously from that state, indicating that probability transfers *directly* to each of the dominant product states. In comparison, for the initial state Cl + H_2O(a=1) (Fig. 5.9a), probability first transfers from a=1 to s=1, as evidenced by the growth of probability in s=1. This transfer must occur as the tail of the wavepacket reaches the avoided crossing between these two states (designated as avoided crossing 5 on the adiabatic potential curves in Fig. 5.3a). As the probability in s=1 subsequently drops near 500 fs, the probability in HCl(v=0) grows, indicating

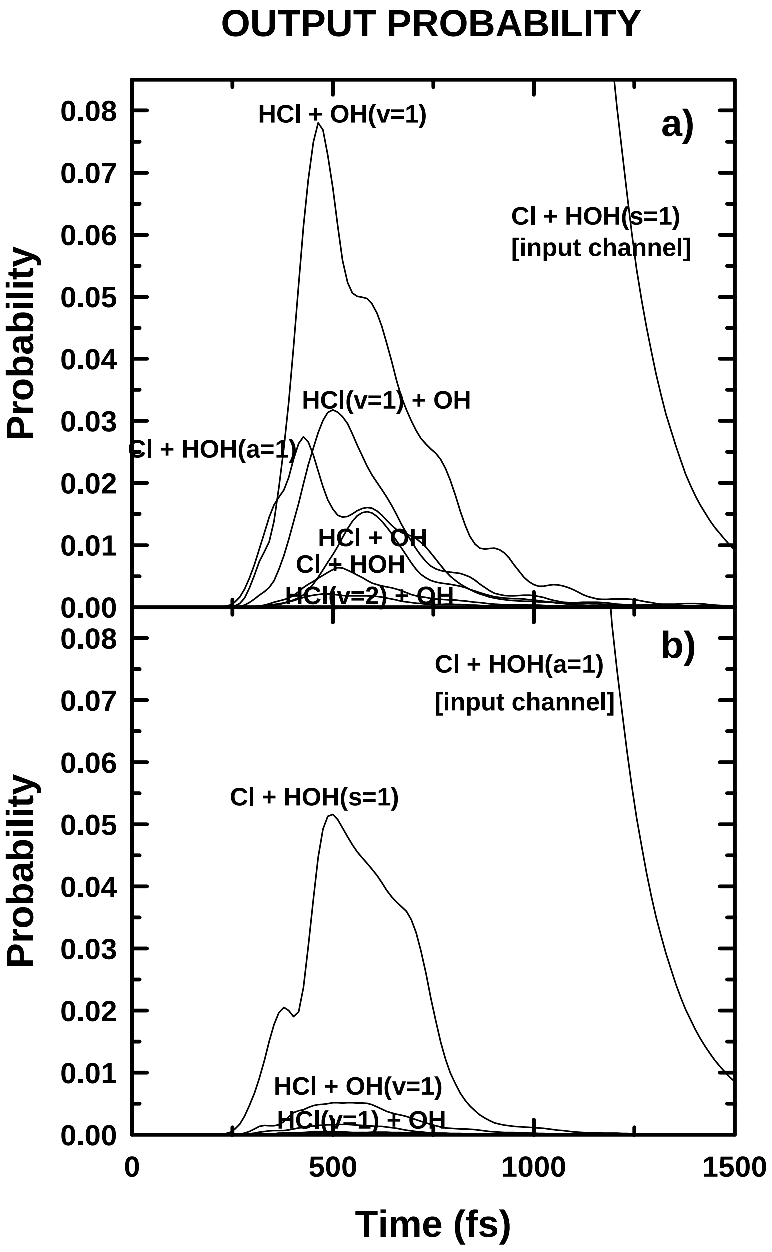

Figure 5.9. Wavepacket probability in each channel as a function of time for a) Cl + HOH(s=1) and b) Cl + HOH(a=1) at p ~ 10 au. At the end of the timescale, the probability in each channel approaches zero due to damping of the wavefunction outside the interaction region. For Cl + HOH(s=1) (Fig. 5.9a), probability transfers directly into the asymmetric stretch and two HCl/OH product states, while for Cl + H_2O(a=1) (Fig. 5.9b) probability first transfers into the symmetric stretch, then to HCl(v=0).

that the path from the input antisymmetric stretch state to reaction must pass through the symmetric stretch.

As predicted in Sect. 5.3.2, the dynamics of Cl + D_2O(a=1) are altered from those of Cl + H_2O(a=1) by the presence of a low-lying state from the v=2 manifold. Fig. 5.10a demonstrates that as with H_2O(a=1), some probability transfers from a=1 to s=1 and subsequently into the DCl + OD v=1 product states. However, more probability flows directly from D_2O(a=1) into DCl(v=2) via avoided crossings 3 and 4 shown on Fig. 5.3b. This behavior indicates that the lowering of the v=2 manifold relative to v=1 by isotopic substitution effectively opens an additional product channel unavailable to H_2O.

For Cl + HOD, the probabilities as a function of time from the v_{OD} input channel are given in Fig. 5.10b. This probability plot shows amplitude oscillating out of v_{OH}=1 as the wavepacket passes through the couplings at crossings 1 and 2 (Fig. 5.3c). Since the probability for the v=1 reactive product grows in between those two peaks, it must result from the coupling at crossing 3. This result is intriguing, since that coupling velocity is quite larger than most of the other coupling velocities yet clearly contributes to the formation of the product channels.

The last part of this analysis is to examine how a greater collision momentum affects the probability distribution in each product channel, focusing on Cl + H_2O. Figure 5.11a-b plots the output fluxes from Cl + H_2O(s=1) and Cl + H_2O(a=1), respectively, as a function of increasing momentum. Three major points can be gleaned from a comparison of these two figures. First of all, not surprisingly, the total amount of inelastic/reactive scattering increases with increasing momentum in

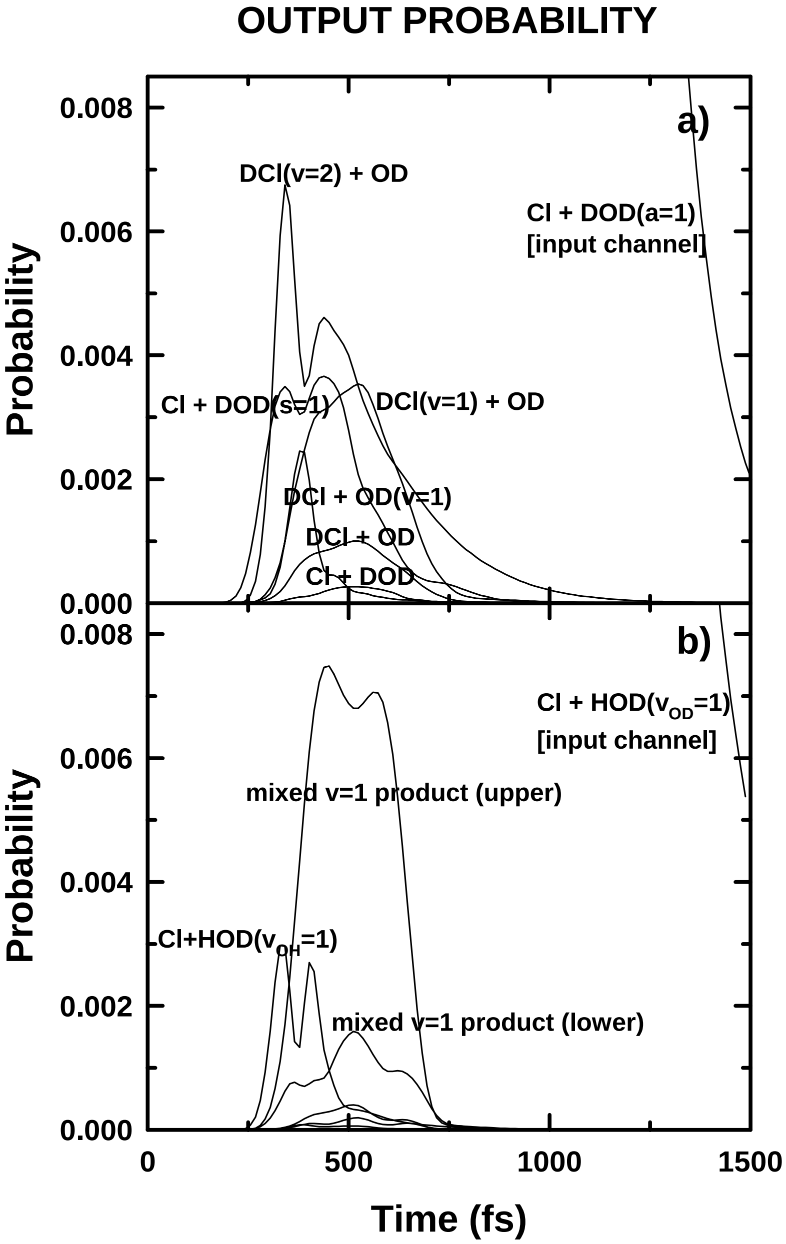

Figure 5.10. Wavepacket probability in each channel as a function of time for a) Cl + DOD(a=1) and b) Cl + HOD(v_{OD}=1), damped to zero after leaving the interaction region. For D_2O (5.10a), as with H_2O(a=1), some probability transfers from a=1 to s=1 to products; however, more probability flows directly from D_2O(a=1) into DCl(v=2) due the lowering of the v=2 manifold relative to v=1 by isotopic substitution. For Cl + HOD (5.10b), amplitude leaves v_{OH}=1 and transfers to the v=1 reactive product as the wavepacket passes through the avoided crossings 1 and 2.

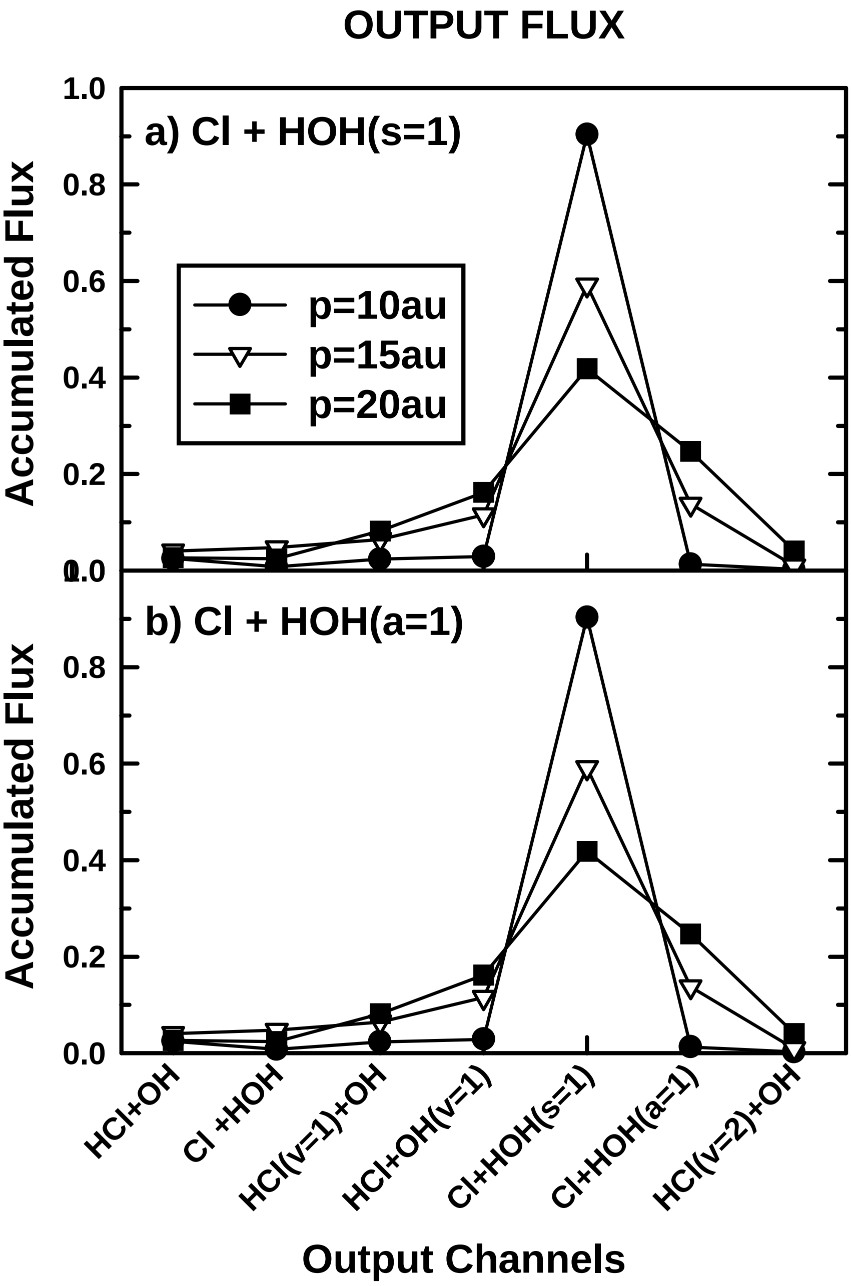

Figure 5.11. Momentum dependence of output fluxes in each channel from a) Cl + H_2O(s=1) and b) Cl + H_2O(a=1). In both cases, total inelastic and reactive scattering increase with increasing momentum; for H_2O(s=1), inelastic scattering grows larger than reactive, while for Cl + H_2O(a=1), reactive grows larger than inelastic. As a result, at high collision momenta, excitation of the antisymmetric stretch forms more HCl + OH product than does the symmetric stretch.

both cases. This increase reflects the greater number of avoided crossings accessed by wavepackets at the higher momentum, as evidenced by the location of the classical turning points further into the interaction region (denoted p_{hi} in Fig. 5.4a).

Second, the relative amounts of inelastic and reactive scattering *reverse* between low and high momentum: for scattering from s=1, inelastic grows larger than reactive, while for scattering from a=1, reactive grows larger than inelastic. The adiabatic curves for this system (Fig. 5.4a) provide an explanation for this phenomenon. As mentioned previously, as R decreases, the s=1 adiabatic state begins to resemble a local-mode OH stretch directed toward the Cl atom, while the a=1 adiabat becomes a local-mode stretch away from the Cl. Correspondingly, the transition between these two adiabats represents a transition between local-mode stretches. For high-momentum scattering from s=1 and a=1, the classical turning point lies directly on the avoided crossing between these two states (avoided crossing 5); accordingly, a larger amount of wavepacket probability transfers than at low momentum. For input on Cl + H_2O(s=1) (Fig. 5.11a), this diabatic transfer to the local-mode stretch *away from* the Cl leaves probability “stuck” in the a=1 exit channel, which has no subsequent crossings into reactive states as the wavepacket exits the interaction region. For input on Cl + H_2O(a=1) (Fig. 5.11b), the opposite occurs: more probability transfers into the local-mode stretch *toward* the Cl and can subsequently transfer into the HCl(v=0) + OH(v=1) product state. The higher momentum also produces an increased probability of this transfer to the reactive channel such that probability in the product channel grows.

Third, as a result of these high-momentum inversions in inelastic versus reactive channels for both input states, the relative amounts of reaction product from the two input channels also inverts: excitation of the *antisymmetric* stretch now forms *more* HCl + OH product than does excitation of the symmetric stretch. In other words, the antisymmetric stretch becomes more reactive than the symmetric stretch with increased collision velocity. The implications of this result are discussed in the next section.

5.4 Discussion

The preceding section outlines the key results of the Cl + H_2O/D_2O/HOD reactive scattering calculations, exploring in detail how the adiabatic curves generated for this prototypical set of reaction systems can be used to predict the subsequent dynamics. Our final step is to reexamine the specifics of this model system to determine what insights can be formed that are independent from the details of the potential surface and the collinear water geometry.

Perhaps the most intriguing outcome of these calculations is the rotation of the symmetric-stretch eigenstate of H_2O towards the approaching Cl atom and the corresponding rotation of the antisymmetric stretch away from the Cl. This result indicates that, adiabatically, the antisymmetric stretch correlates with vibrational excitation in the non-reacting bond. This concept is not new; indeed, Schatz[35] postulated that this correlation should generally exist in systems with symmetric and antisymmetric stretches for the following reason. The local-mode, reactive bond stretch is lowered in energy relative to the unreactive bond by the approaching reactant; it thus adiabatically couples to the lower-energy symmetric stretch, thereby increasing the reactivity of the symmetric stretch relative to the antisymmetric stretch.

This principle was demonstrated by Schatz with classical trajectory calculations for O + CS_2: vibrational adiabaticity in this reaction yields more OS + CS product from the CS_2 symmetric stretch than the antisymmetric stretch.[35] This result is consistent with our results for Cl + linear H_2O: at the lowest translational energy calculated, the symmetric stretch of H_2O is more reactive. It is intriguing that this effect appears in both O + CS_2, in which O-S-C is a light-heavy-light atom combination, and in Cl + H_2O, with a Cl-H-O as a light-heavy-light combination, in calculations at comparable collision energies. Since the vibrational energies of the symmetric and antisymmetric stretch in CS_2 are much more widely separated than in H_2O, the adiabaticity in that system should persist to higher collision velocities. In contrast, the adiabaticity of our model H_2O breaks down at a collision velocity only three times higher than the average thermal velocity, indicative of a transition to diabatic behavior. Notably, the spacing between the experimental symmetric and antisymmetric stretch energies in water is approximately half that spacing in our model.[36] Correspondingly, we anticipate that the vibrational adiabaticity of water should break down at even lower, i.e., near-thermal, collision velocities.

A related result, observed in all three collision systems, is that the local-mode stretch in the reactive bond is lowered in energy with respect to the ground state as the reactive atom approaches. In H_2O and D_2O, this lowers the energy of the proximal OH stretch (which corresponds asymptotically to the symmetric stretch) toward the reactive channels. In Cl + HOD, however, this lowers the higher-energy

OH stretch toward the OD stretch, producing a strong mixing between v_{OH} and v_{OD} character in the HOD well region. While the magnitude of this mixing will vary for different systems, the trend should be the same for any high-frequency vibration approached by a reactive atom.

Finally, the lowering of the next excited vibrational manifold (v=2) in D_2O relative to D_2O(v=1) opens up a higher-energy product channel for the antisymmetric stretch of D_2O, one which is unavailable to H_2O. This emphasizes that isotopic substitution affects not only the vibrations within a single manifold, but also the positioning of those vibrational manifolds with respect to one another.

5.5 Conclusions

The role of intramolecular vibrational redistribution (IVR) on the timescale of a reactive encounter is explored via time-dependent quantum reactive scattering on a linear model system with isotopic variations. In these studies, the vibrational eigenstates of $Cl + H_2O \rightarrow HCl + OH$ are calculated as a function of Cl-H_2O center-of-mass separation using a Chebychev expansion of the time-dependent propagation operator in imaginary time. This calculation generates adiabatic potential energy curves, as well as the coupling matrix elements for transitions between these curves, for use in time-dependent dynamics calculations. For the vibrational eigenfunctions, the near-resonance of the H_2O symmetric and antisymmetric stretch causes these states to couple strongly as the Cl atom approaches. These couplings rotate the symmetric stretch of H_2O into a local-mode excitation pointing *towards* the Cl, and the antisymmetric stretch *away from* the Cl. Scattering calculations from the symmetric and antisymmetric stretch thus indicate greater probability for product formation from the symmetric stretch than the antisymmetric stretch at low collision velocities. This vibrational adiabaticity breaks down at higher velocities, so that the antisymmetric stretch becomes more reactive than the symmetric stretch. For the similar Cl + D_2O simulation, the reduced stretching vibrational frequencies provide less energy towards reaction, hence the reaction probability decreases for both modes, while the lowering of the DCl(v=2) product state relative to the antisymmetric stretch states increases reactive scattering over inelastic scattering from the symmetric stretch. For Cl + HOD, vibrational excitation in OH enhances HCl + OD reaction probability by an order of magnitude more than excitation in OD.

References for Chapter 5

1. M. J. Bronikowski, W. R. Simpson, B. Girard, and R. N. Zare, *J. Chem. Phys.* **95,** 8647 (1991).

2. A. Sinha, M. C. Hsiao, and F. F. Crim, *J. Chem. Phys.* **92,** 6333 (1990).

3. A. Sinha, M. C. Hsiao, and F. F. Crim, *J. Chem. Phys.* **94,** 4928 (1991).

4. A. Sinha, J. D. Thoemke, and F. F. Crim, *J. Chem. Phys.* **96,** 372 (1992).

5. R. B. Metz, J. D. Thoemke, J. M. Pfeiffer, and F. F. Crim, *J. Chem. Phys.* **99,** 1744 (1993).

6. J. D. Thoemke, J. M. Pfeiffer, R. B. Metz, and F. F. Crim, *J. Phys. Chem.* **99,** 13748 (1995).

7. G. Hawthorne, P. Sharkey, and I. W. M. Smith, *J. Chem. Phys.* **108,** 4693 (1998).

8. R. B. Metz, J. M. Pfeiffer, J. D. Thoemke, and F. F. Crim, *Chem. Phys. Lett.* **221,** 347 (1994).

9. J. M. Pfeiffer, R. B. Metz, J. D. Thoemke, E. Woods, III, and F. F. Crim, *J. Chem. Phys.* **104,** 4490 (1996).

10. C. Kreher, R. Theinl, and K.-H. Gericke, *J. Chem. Phys.* **104,** 1996 (1996).

11. W. R. Simpson, A. J. Orr-Ewing, and R. N. Zare, *Chem. Phys. Lett.* **212,** 163 (1993).

12. W. R. Simpson, T. P. Rakitzis, S. A. Kandel, A. J. Orr-Ewing, and R. N. Zare, *J. Chem. Phys.* **103,** 7313 (1995).

13. W. R. Simpson, A. J. Orr-Ewing, S. A. Kandel, T. P. Rakitzis, and R. N. Zare, *J. Chem. Phys.* **103,** 7299 (1995).

14. G. C. Schatz, M. C. Colton, and J. L. Grant, *J. Phys. Chem.* **88,** 2971 (1984).

15. K. Kudla and G. C. Schatz, *Chem. Phys. Lett.* **193,** 507 (1992).

16. D. C. Clary, *Chem. Phys. Lett.* **192,** 34 (1992).

17. G. Nyman and D. C. Clary, *J. Chem. Phys.* **100,** 3556 (1994).

18. D. Wang and J. M. Bowman, *J. Chem. Phys.* **98,** 6235 (1992).

19. D. H. Zhang and J. C. Light, *J. Chem. Phys.* **104,** 4544 (1996).

20. D. H. Zhang and J. C. Light, *J. Chem. Soc., Faraday Trans.* **93,** 691 (1997).

21. J. Echave and D. C. Clary, *J. Chem. Phys.* **100,** 402 (1994).

22. T. Takayanagi and G. C. Schatz, *J. Chem. Phys.* **106,** 3227 (1997).

23. M. S. Child, in *Atom-Molecule Collision Theory,* edited by R. B. Bernstein (Plenum Press, New York, 1979).

24. A. Persky and A. Broida, *J. Chem. Phys.* **81,** 4352 (1984).

25. D. L. Baulch, R. A. Cox, R. F. Hampson, J. A. Kerr, J. Troe, and R. T. Watson, *J. Phys. Chem. Ref. Data* **13,** 1259 (1984).

26. R. Kosloff, in *Dyn. Mol. Chem. React.*, edited by R. E. Wyatt (Dekker, New York, N, 1996), pp. 185.

27. R. Kosloff, *Annu. Rev. Phys. Chem.* **45,** 145 (1994).

28. R. Kosloff and H. Tal-Ezer, *Chem. Phys. Lett.* **127,** 223 (1986).

29. O. Dulieu, R. Kosloff, F. Masnou-Seeuws, and G. Pichler, *J. Chem. Phys.* **107,** 10633 (1997).

30. M. S. Child, *Semiclassical Mechanics with Molecular Applications* (Clarendon Press, Oxford, 1991).

31. I. Tuvi and Y. B. Band, *J. Chem. Phys.* **107,** 9079 (1997).

32. C. Cohen-Tannoudji, B. Diu, and F. Laloe, *Quantum Mechanics* (Hermann, Paris, 1977).

33. V. A. Mandelshtam and H. S. Taylor, *J. Chem. Phys.* **102,** 7390 (1995).

34. V. A. Mandelshtam and H. S. Taylor, *J. Chem. Phys.* **103,** 2903 (1995).

35. G. C. Schatz, *J. Chem. Phys.* **71,** 542 (1979).

36. W. S. Benedict, N. Gailar, and E. K. Plyler, *J. Chem. Phys.* **24,** 1139 (1956).

BIBLIOGRAPHY

S. F. Adams and T. A. Miller, *Chem. Phys. Lett.* **295,** 305 (1998).

E. B. Anthony, W. Schade, M. J. Bastian, V. M. Bierbaum, and S. R. Leone, *J. Chem. Phys.* **106,** 5413 (1997).

E. B. Anthony, Ph. D. thesis, University of Colorado, 1998.

V. Aquilanti, D. Ascenzi, D. Cappelletti, and F. Pirani, *Nature* **371,** 399 (1994).

V. Aquilanti, D. Ascenzi, D. Cappelletti, S. Franceschini, and F. Pirani, *Phys. Rev. Lett.* **74,** 2929 (1995).

V. Aquilanti, D. Ascenzi, D. Cappelletti, R. Fedeli, and F. Pirani, *J. Phys. Chem. A* **101,** 7648 (1997).

V. Aquilanti, D. Ascenzi, D. Cappelletti, M. de Castro, and F. Pirani, *J. Chem. Phys.* **109,** 3898 (1998).

V. Aquilanti, private communication

R. A. Aziz and H. H. Chen, *J. Chem. Phys.* **67,** 5719 (1977).

Y. B. Band and P. S. Julienne, *J. Chem. Phys.* **96,** 3339 (1992).

I. Bar, Y. Cohen, D. David, S. Rosenwaks, and J. J. Valentini, *J. Chem. Phys.* **93,** 2146 (1990).

I. Bar, Y. Cohen, D. David, T. Arusi-Parpar, S. Rosenwaks, and J. J. Valentini, *J. Chem. Phys.* **95,** 3341 (1991).

D. L. Baulch, R. A. Cox, R. F. Hampson, J. A. Kerr, J. Troe, and R. T. Watson, *J. Phys. Chem. Ref. Data* **13,** 1259 (1984).

R. J. Bemish, M. Wu, and R. E. Miller, *Faraday Discussions* **97,** 57 (1994).

R. J. Bemish, M. C. Chan, and R. E. Miller, *Chem. Phys. Lett.* **251,** 182 (1996).

W. S. Benedict, N. Gailar, and E. K. Plyler, *J. Chem. Phys.* **24,** 1139 (1956).

L. Beneventi, P. Casavecchia, and G. G. Volpi, *J. Chem. Phys.* **85,** 7011 (1986).

L. Beneventi, P. Casavecchia, F. Vecchiocattivi, G. G. Volpi, U. Buck, C. Lauenstein, and R. Schinke, *J. Chem. Phys.* **89,** 4671 (1988).

H. G. Bennewitz, K. H. Kramer, W. Paul, and J. P. Toennies, *Z. Phys.* **177,** 84 (1964).

M. T. Berry, M. R. Brustein, and M. I. Lester, *Chem. Phys. Lett.* **153,** 17 (1988).

M. T. Berry, M. R. Brustein, J. R. Adamo, and M. I. Lester, *J. Phys. Chem.* **92,** 5551 (1988).

M. T. Berry, M. R. Brustein, and M. I. Lester, *J. Chem. Phys.* **90,** 5878 (1989).

M. T. Berry, M. R. Brustein, and M. I. Lester, *J. Chem. Phys.* **92,** 6469 (1990).

M. T. Berry, R. A. Loomis, L. C. Giancarlo, and M. I. Lester, *J. Chem. Phys.* **96,** 7890 (1992).

R. J. Beuhler, Jr., R. B. Bernstein, and K. H. Kramer, *J. Am. Chem. Soc.* **88,** 5331 (1966).

P. A. Block, E. J. Bohac, and R. E. Miller, *Phys. Rev. Lett.* **68,** 1303 (1992).

U. Borkenhagen, H. Malthan, and J. P. Toennies, *J. Chem. Phys.* **71,** 1722 (1979).

S. K. Bramble and P. A. Hamilton, *Chem. Phys. Lett.* **170,** 107 (1990).

P. Brechignac, A. Picard-Bersellini, and R. Charneau, *J. Phys. B* **13,** 135 (1980).

M. J. Bronikowski, W. R. Simpson, B. Girard, and R. N. Zare, *J. Chem. Phys.* **95,** 8647 (1991).

P. R. Brooks and E. M. Jones, *J. Chem. Phys.* **45,** 3449 (1966).

P. R. Brooks, *Science* **193,** 11 (1976).

M. Brouard and S. R. Langford, *J. Chem. Phys.* **106,** 6354 (1997).

A. D. Bykov, V. A. Kapitanov, O. V. Naumenko, T. M. Petrova, V. I. Serdyukov, and L. N. Sinitsa, *J. Mol. Spec.* **153,** 197 (1992).

C. C. Carter and T. A. Miller, *J. Chem. Phys.* **107,** 3447 (1997).

C. C. Carter, T. A. Miller, H.-S. Lee, A. B. McCoy, and E. F. Hayes, *J. Chem. Phys.* **110,** 5065 (1999).

C. C. Carter, T. A. Miller, H.-S. Lee, P. P. Korambath, A. B. McCoy, and E. F. Hayes, *J. Chem. Phys.* **110,** 1508 (1999).

B. C. Chang, L. Yu, D. Cullin, B. Rehfuss, J. Williamson, T. A. Miller, W. M. Fawzy, X. Zheng, S. Fei, and M. Heaven, *J. Chem. Phys.* **95,** 7086 (1991).

B. C. Chang, J. M. Williamson, D. W. Cullin, J. R. Dunlop, and T. A. Miller, *J. Chem. Phys.* **97,** 7999 (1992).

B. C. Chang, D. W. Cullin, J. M. Williamson, J. R. Dunlop, B. D. Rehfuss, and T. A. Miller, *J. Chem. Phys.* **96,** 3476 (1992).

B.-C. Chang, J. R. Dunlop, J. M. Williamson, T. A. Miller, and M. C. Heaven, *Chem. Phys. Lett.* **207,** 62 (1993).

B.-C. Chang, J. R. Dunlop, and T. A. Miller, *Chem. Phys. Lett.* **207,** 55 (1993).

B.-C. Chang, J. R. Dunlop, J. M. Williamson, and T. A. Miller, *J. Opt. Soc. Am. B* **11,** 198 (1994).

M. S. Child, in *Atom-Molecule Collision Theory*, edited by R. B. Bernstein (Plenum Press, New York, 1979).

M. S. Child and L. Halonen, *Adv. Chem. Phys.* **57,** 1 (1984).

M. S. Child, *Semiclassical Mechanics with Molecular Applications* (Clarendon Press, Oxford, 1991).

K. M. Christoffel and J. M. Bowman, *J. Chem. Phys.* **104,** 8348 (1996).

C.-C. Chuang, P. M. Andrews, and M. I. Lester, *J. Chem. Phys.* **103,** 3418 (1995).

C. Chuaqui, R. J. Le Roy, and A. R. W. McKellar, *J. Chem. Phys.* **101,** 39 (1994).

D. C. Clary, *Chem. Phys. Lett.* **192,** 34 (1992).

R. C. Cohen and R. J. Saykally, *J. Phys. Chem.* **94,** 7991 (1990).

R. C. Cohen and R. J. Saykally, *J. Chem. Phys.* **98,** 6007 (1993).

Y. Cohen, I. Bar, and S. Rosenwaks, *J. Chem. Phys.* **102,** 3612 (1995).

C. Cohen-Tannoudji, B. Diu, and F. Laloe, *Quantum Mechanics* (Hermann, Paris, 1977).

F. F. Crim, *J. Phys. Chem.* **100,** 12725 (1996).

F. C. De Lucia, R. L. Cook, P. Helminger, and W. Gordy, *J. Chem. Phys.* **55,** 5334 (1971).

H. G. Dehmelt and K. B. Jefferts, *Phys. Rev.* **125,** 1318 (1962).

M. S. deVries, G. W. Tyndall, C. L. Cobb, and R. M. Martin, *J. Chem. Phys.* **86,** 2653 (1987).

R. Dopheide and H. Zacharias, *J. Chem. Phys.* **99,** 4864 (1993).

R. A. Dressler, H. Meyer, and S. R. Leone, *J. Chem. Phys.* **87,** 6029 (1987).

O. Dulieu, R. Kosloff, F. Masnou-Seeuws, and G. Pichler, *J. Chem. Phys.* **107,** 10633 (1997).

J. Echave and D. C. Clary, *J. Chem. Phys.* **100,** 402 (1994).

R. C. Estler and R. N. Zare, *J. Am. Chem. Soc.* **100,** 1323 (1978).

J. R. Fair, O. Votava, and D. J. Nesbitt, *J. Chem. Phys.* **108,** 72 (1998).

W. M. Fawzy and M. C. Heaven, *J. Chem. Phys.* **89,** 7030 (1988).

W. M. Fawzy and M. C. Heaven, *J. Chem. Phys.* **92,** 909 (1990).

B. Follmeg, P. Rosmus, and H.-J. Werner, *J. Chem. Phys.* **93,** 4687 (1990).

B. Follmeg, H.-J. Werner, and P. Rosmus, *J. Chem. Phys.* **95,** 979 (1991).

B. Friedrich, D. P. Pullman, and D. R. Herschbach, *J. Phys. Chem.* **95,** 8118 (1991).

B. Friedrich and D. R. Herschbach, *Nature* **353,** 412 (1991).

B. Friedrich, H.-G. Rubahn, and N. Sathyamurthy, *Phys. Rev. Lett.* **69,** 2487 (1992).

B. Friedrich and D. R. Herschbach, *Z. Phys. D* **24,** 25 (1992).

B. Friedrich, A. Slenczka, and D. Herschbach, *Chem. Phys. Lett.* **221,** 333 (1994).

B. Friedrich, A. Slenczka, and D. Herschbach, *Can. J. Phys.* **72,** 897 (1994).

B. Friedrich and D. Herschbach, *Phys. Rev. Lett.* **74,** 4623 (1995).

B. Friedrich and D. Herschbach, *J. Phys. Chem.* **99,** 15686 (1995).

B. Friedrich and D. Herschbach, *Chem. Phys. Lett.* **262,** 41 (1996).

W. Gabriel, E.-A. Reinsch, P. Rosmus, S. Carter, and N. C. Handy, *J. Chem. Phys.* **99,** 897 (1993).

A. Garcia-Vela, *J. Chem. Phys.* **108,** 5755 (1998).

C. J. Gorter, *Z. Phys.* **26,** 140 (1938).

R. A. Gottscho, R. W. Field, R. Bacis, and S. J. Silvers, *J. Chem. Phys.* **73,** 599 (1980).

C. H. Greene and R. N. Zare, *Ann. Rev. Phys. Chem.* **33,** 119 (1982).

B. E. Grossmann and E. V. Browell, *J. Mol. Spec.* **138,** 562 (1989).

J. B. Halpern, R. Dopheide, and H. Zacharias, *J. Phys. Chem.* **99,** 13611 (1995).

S. Harich and A. M. Wodtke, *J. Chem. Phys.* **107,** 5983 (1997).

G. Hawthorne, P. Sharkey, and I. W. M. Smith, *J. Chem. Phys.* **108,** 4693 (1998).

U. Hefter, G. Ziegler, A. Mattheus, A. Fischer, and K. Bergmann, *J. Chem. Phys.* **85,** 286 (1986).

G. Herzberg, *Infrared and Raman Spectra of Polyatomic Molecules* (Krieger, Malabar, 1991).

T.-S. Ho, H. Rabitz, S. E. Choi, and M. I. Lester, *J. Chem. Phys.* **102,** 2282 (1995).

M. Hoffmeister, R. Schleysing, and H. J. Loesch, *J. Phys. Chem.* **91,** 5441 (1987).

J. P. Houdeau, M. Larvor, and C. Haeusler, *Can. J. Phys.* **58,** 318 (1980).

H. Hulsman and J. Korving, *J. Chem. Phys.* **95,** 5719 (1991).

C. Jacques, L. Valachovic, S. Ionov, E. Bohmer, Y. Wen, J. Segall, and C. Wittig, *J. Chem. Soc. Faraday Trans.* **89,** 1419 (1993).

J. C. Juanes-Marcos and A. Garcia-Vela, *J. Chem. Phys.* **111,** 2606 (1999).

Z. Karny, R. C. Estler, and R. N. Zare, *J. Chem. Phys.* **69,** 5199 (1978).

J. A. Kerr, *Chem. Rev.* **66,** 465 (1966).

V. Khare, D. J. Kouri, and D. K. Hoffman, *J. Chem. Phys.* **74,** 2275 (1981).

W. Kim and P. M. Felker, *J. Chem. Phys.* **104,** 1147 (1996).

W. Kim and P. M. Felker, *J. Chem. Phys.* **107,** 2193 (1997).

P. P. Korambath, X. T. Wu, E. F. Hayes, C. C. Carter, and T. A. Miller, *J. Chem. Phys.* **107,** 3460 (1997).

P. P. Korambath, X. T. Wu, and E. F. Hayes, *J. Chem. Phys.* **107,** 3460 (1997).

R. Kosloff and H. Tal-Ezer, *Chem. Phys. Lett.* **127,** 223 (1986).

R. Kosloff, *J. Phys. Chem.* **92,** 2087 (1988).

R. Kosloff, *Annu. Rev. Phys. Chem.* **45,** 145 (1994).

R. Kosloff, in *Dyn. Mol. Chem. React.*, edited by R. E. Wyatt (Dekker, New York, N, 1996), pp. 185.

K. H. Kramer and R. B. Bernstein, *J. Chem. Phys.* **40,** 200 (1964).

C. Kreher, R. Theinl, and K.-H. Gericke, *J. Chem. Phys.* **104,** 1996 (1996).

K. Kudla and G. C. Schatz, *Chem. Phys. Lett.* **193,** 507 (1992).

A. C. Kummel, G. O. Sitz, and R. N. Zare, *J. Chem. Phys.* **85,** 6874 (1986).

A. C. Kummel, G. O. Sitz, and R. N. Zare, *J. Chem. Phys.* **88,** 6707 (1988).

A. C. Kummel, G. O. Sitz, and R. N. Zare, *J. Chem. Phys.* **88,** 7357 (1988).

M. I. Lester, *NATO ASI Ser., Ser. B* **227,** 143 (1990).

M. I. Lester, R. W. Randall, L. C. Giancarlo, and S. E. Choi, *J. Chem. Phys.* **99,** 6211 (1993).

M. I. Lester, R. A. Loomis, L. C. Giancarlo, M. T. Berry, C. Chakravarty, and D. C. Clary, *J. Chem. Phys.* **98,** 9320 (1993).

M. I. Lester, S. E. Choi, L. C. Giancarlo, and R. W. Randall, *Faraday Discuss.* **97,** 365 (1994).

M. I. Lester, W. H. J. Green, C. Chakravarty, and D. C. Clary, *Adv. Ser. Phys. Chem.* **4,** 659 (1995).

M. I. Lester, C.-C. Chuang, P. M. Andrews, M. Yang, and M. H. Alexander, *Faraday Discuss.* **102,** 311 (1996).

M. I. Lester, R. A. Loomis, R. L. Schwartz, and S. P. Walch, *J. Phys. Chem. A* **101,** 9195 (1997).

A. F. Linskens, N. Dam, J. Reuss, and B. Sartakov, *J. Chem. Phys.* **101,** 9385 (1994).

H. J. Loesch and A. Remscheid, *J. Chem. Phys.* **93,** 4779 (1990).

H. J. Loesch and A. Remscheid, *J. Phys. Chem.* **95,** 8194 (1991).

H. J. Loesch and J. Moller, *J. Chem. Phys.* **97,** 9016 (1992).

H. J. Loesch, *Ann. Rev. Phys. Chem.* **46,** 555 (1995).

R. A. Loomis and M. I. Lester, *J. Chem. Phys.* **103,** 4371 (1995).

R. A. Loomis, R. L. Schwartz, and M. I. Lester, *J. Chem. Phys.* **104,** 6984 (1996).

R. A. Loomis and M. I. Lester, *Annu. Rev. Phys. Chem.* **48,** 643 (1997).

A. Lubbert, G. Rotzoll, and F. Gunther, *J. Chem. Phys.* **69,** 5174 (1978).

S. R. Mackenzie, O. Votava, J. R. Fair, and D. J. Nesbitt, *J. Chem. Phys.* **105,** 11360 (1996).

S. R. Mackenzie, O. Votava, J. R. Fair, and D. J. Nesbitt, *J. Chem. Phys.* **110,** 5149 (1999).

V. A. Mandelshtam and H. S. Taylor, *J. Chem. Phys.* **102,** 7390 (1995).

V. A. Mandelshtam and H. S. Taylor, *J. Chem. Phys.* **103,** 2903 (1995).

A. Mattheus, A. Fischer, G. Ziegler, E. Gottwald, and K. Bergmann, *Phys. Rev. Lett.* **56,** 712 (1986).

A. J. McCaffery, K. L. Reid, and B. L. Whitaker, *Phys. Rev. Lett.* **61,** 2085 (1988).

A. J. McCaffery and R. J. Wilson, *Phys. Rev. Lett.* **77,** 48 (1996).

R. B. Metz, J. D. Thoemke, J. M. Pfeiffer, and F. F. Crim, *J. Chem. Phys.* **99,** 1744 (1993).

R. B. Metz, J. M. Pfeiffer, J. D. Thoemke, and F. F. Crim, *Chem. Phys. Lett.* **221,** 347 (1994).

H. Meyer, *Chem. Phys. Lett.* **230,** 510 (1994).

J. Michl and E. W. Thulstrup, *Spectroscopy with polarized light: solute alignment by photoselection in liquid crystals, polymers, and membranes* (VCH, 1995).

D. T. Moore, L. Oudejans, and R. E. Miller, *J. Chem. Phys.* **110,** 197 (1999).

NAG Fortran Library (Oxford University: Oxford, 1997).

D. D. Nelson, Jr., A. Schiffman, D. J. Nesbitt, J. J. Orlando, and J. B. Burkholder, *J. Chem. Phys.* **93,** 7003 (1990).

D. J. Nesbitt and R. W. Field, *J. Phys. Chem.* **100,** 12735 (1996).

T. M. Niebauer, J. E. Faller, H. M. Godwin, J. L. Hall, and R. L. Barger, *Appl. Opt.* **27,** 1285 (1988).

J. B. Norman and R. W. Field, *J. Chem. Phys.* **92,** 76 (1990).

G. Nyman and D. C. Clary, *J. Chem. Phys.* **100,** 3556 (1994).

T. Oka and Y. Morino, *J. Mol. Spec.* **6,** 472 (1961).

A. J. Orr-Ewing, *J. Chem. Soc. Faraday Trans.* **92,** 881 (1996).

A. J. Orr-Ewing and R. N. Zare, *Annu. Rev. Phys. Chem.* **45**, 315 (1994).

D. H. Parker, H. Jalink, and S. Stolte, *J. Phys. Chem.* **91,** 5427 (1987).

D. H. Parker and R. B. Bernstein, *Ann. Rev. Phys. Chem.* **40,** 561 (1989).

A. Persky and A. Broida, *J. Chem. Phys.* **81,** 4352 (1984).

J. M. Pfeiffer, R. B. Metz, J. D. Thoemke, E. Woods, III, and F. F. Crim, *J. Chem. Phys.* **104,** 4490 (1996).

C. D. Pibel and C. B. Moore, *J. Chem. Phys.* **93,** 4805 (1990).

A. S. Pine, *J. Chem. Phys.* **91,** 2002 (1989).

D. F. Plusquellic, O. Votava, and D. J. Nesbitt, *Appl. Opt.* **35,** 1464 (1996).

D. F. Plusquellic, O. Votava, and D. J. Nesbitt, *J. Chem. Phys.* **109,** 6631 (1998).

E. Pollak, *J. Chem. Phys.* **86,** 1645 (1987).

O. L. Polyansky, P. Jensen, and J. Tennyson, *J. Chem. Phys.* **105,** 6490 (1996).

D. P. Pullman and D. R. Herschbach, *J. Chem. Phys.* **90,** 3881 (1988).

D. P. Pullman, B. Friedrich, and D. R. Herschbach, *J. Chem. Phys.* **93,** 3224 (1990).

D. P. Pullman, B. Friedrich, and D. R. Herschbach, *J. Phys. Chem.* **99,** 7407 (1995).

M. Quack, *Ann. Rev. Phys. Chem.* **41,** 839 (1990).

M. Quack and W. Kutzelnigg, *Ber. Bunsenges. Phys. Chem.* **99,** 231 (1995).

L. M. Raff and D. L. Thompson, in *Theory of Chemical Reaction Dynamics*, Vol. III, edited by M. Baer (CRC Press, Boca Raton, 1985), pp. 1.

D. A. Ramsay, *J. Chem. Phys.* **20,** 1920 (1952).

G. Ravindra Kumar, P. Gross, C. P. Safvan, F. A. Rajgara, and D. Mathur, *Phys. Rev. A* **53,** 3098 (1996).

See, for example, A. J. Orr-Ewing and R. N. Zare, Annu. Rev. Phys. Chem. **45**, 315 (1994); H. J. Loesch, Annu. Rev. Phys. Chem. **46**, 555 (1995); A. J. Orr-Ewing, J. Chem. Soc. Faraday Trans. **92**, 881 (1996).

E. Riedle, S. H. Ashworth, J. T. Farrell, Jr., and D. J. Nesbitt, *Rev. Sci. Instrum.* **65,** 42 (1994).

L. S. Rothman, R. R. Gamache, R. H. Tipping, C. P. Rinsland, M. A. H. Smith, D. C. Benner, V. M. Devi, J.-M. Flaud, C. Camy-Peret, A. Perrin, A. Goldman, S. T. Massie, L. R. Brown, and R. A. Toth, *J. Quant. Spectrosc. Radiat. Transfer* **48,** 469 (1992).

Rothman, L. S., HITRAN database (ONTAR, 1996)

N. Rougeau and C. Kubach, *Chem. Phys. Lett.* **299,** 120 (1999).

H.-G. Rubahn and J. P. Toennies, *J. Chem. Phys.* **89,** 287 (1988).

A. D. Rudert, J. Martin, H. Zacharias, and J. B. Halpern, *Chem. Phys. Lett.* **294,** 381 (1998).

M. L. Sage and J. Jortner, *Adv. Chem. Phys.* **47,** 293 (1981).

H. J. Saleh and A. J. McCaffery, *J. Chem. Soc. Faraday Trans.* **89,** 3217 (1993).

W. R. Sanders and J. B. Anderson, *Chem. Phys. Lett.* **47,** 283 (1977).

W. R. Sanders and J. B. Anderson, *J. Phys. Chem.* **88,** 4479 (1984).

W. Schade, J. Walewski, A. Offt, and A. Knaack, *Phys. Rev. A* **53,** 2921 (1996).

G. C. Schatz, *J. Chem. Phys.* **71,** 542 (1979).

G. C. Schatz, M. C. Colton, and J. L. Grant, *J. Phys. Chem.* **88,** 2971 (1984).

I. Schek, J. Jortner, and M. L. Sage, *Chem. Phys. Lett.* **64,** 209 (1979).

A. Schiffman and D. J. Nesbitt, *J. Chem. Phys.* **100,** 2677 (1994).

R. L. Shoemaker, S. Stenholm, and R. G. Brewer, *Phys. Rev. A* **10,** 2037 (1974).

E. L. Sibert, III, W. P. Reinhardt, and J. T. Hynes, *Chem. Phys. Lett.* **92,** 455 (1982).

E. L. Sibert, III, W. P. Reinhardt, and J. T. Hynes, *J. Chem. Phys.* **81,** 1115 (1984).

E. L. Sibert, III, W. P. Reinhardt, and J. T. Hynes, *1984* **81,** 1135 (1984).

S. J. Silvers, R. A. Gottscho, and R. W. Field, *J. Chem. Phys.* **74,** 6000 (1981).

W. R. Simpson, A. J. Orr-Ewing, and R. N. Zare, *Chem. Phys. Lett.* **212,** 163 (1993).

W. R. Simpson, T. P. Rakitzis, S. A. Kandel, A. J. Orr-Ewing, and R. N. Zare, *J. Chem. Phys.* **103,** 7313 (1995).

W. R. Simpson, A. J. Orr-Ewing, S. A. Kandel, T. P. Rakitzis, and R. N. Zare, *J. Chem. Phys.* **103,** 7299 (1995).

M. P. Sinha, C. D. Caldwell, and R. N. Zare, *J. Chem. Phys.* **61,** 491 (1974).

A. Sinha, M. C. Hsiao, and F. F. Crim, *J. Chem. Phys.* **92,** 6333 (1990).

A. Sinha, M. C. Hsiao, and F. F. Crim, *J. Chem. Phys.* **94,** 4928 (1991).

A. Sinha, J. D. Thoemke, and F. F. Crim, *J. Chem. Phys.* **96,** 372 (1992).

A. Slenczka, B. Friedrich, and D. Herschbach, *Phys. Rev. Lett.* **72,** 1806 (1994).

A. M. Smith, K. K. Lehmann, and W. Klemperer, *J. Chem. Phys.* **85,** 4958 (1986).

L. D. Snow, R. N. Compton, and J. C. Miller, *J. Chem. Phys.* **88,** 1652 (1988).

S. Stolte, *Ber. Bunsenges. Phys. Chem.* **86,** 413 (1982).

T. Suzuki, H. Katayanagi, and M. C. Heaven, *J. Phys. Chem. A* **101,** 6697 (1997).

T. Takayanagi and G. C. Schatz, *J. Chem. Phys.* **106,** 3227 (1997).

K. T. Tang and J. P. Toennies, *Chem. Phys.* **156,** 413 (1991).

J. Tennyson, J. R. Henderson, and N. G. Fulton, *Comput. Phys. Commun.* **86,** 175 (1995).

Tennyson, J., private communication

G. Theodorakopoulos and I. D. Petsalakis, *Chem. Phys. Lett.* **178,** 475 (1991).

G. Theodorakopoulos, I. D. Petsalakis, and C. A. Nicolaides, *Chem. Phys. Lett.* **207,** 321 (1993).

J. D. Thoemke, J. M. Pfeiffer, R. B. Metz, and F. F. Crim, *J. Phys. Chem.* **99,** 13748 (1995).

J. P. Toennies, *Z. Phys.* **182,** 257 (1965).

M. A. Treffers and J. Korving, *Chem. Phys. Lett.* **97,** 342 (1983).

M. A. Treffers and J. Korving, *J. Chem. Phys.* **85,** 5076 (1985).

M. A. Treffers and J. Korving, *J. Chem. Phys.* **85,** 5085 (1986).

I. Tuvi and Y. B. Band, *J. Chem. Phys.* **107,** 9079 (1997).

R. L. Vander Wal, J. L. Scott, F. F. Crim, K. Weide, and R. Schinke, *J. Chem. Phys.* **94,** 3548 (1991).

A. G. Visser, J. P. Bekooy, L. K. van der Meij, C. de Vreudg, and J. Korving, *Chem. Phys.* **20,** 391 (1977).

O. Votava, J. R. Fair, D. F. Plusquellic, E. Riedle, and D. J. Nesbitt, *J. Chem. Phys.* **107,** 8854 (1997).

Votava, O., Plusquellic, D. F., Mackenzie, S. R., Fair, J. R., Nesbitt, D. J. (in preparation).

D. Wang and J. M. Bowman, *J. Chem. Phys.* **98,** 6235 (1992).

J. K. G. Watson, *J. Chem. Phys.* **46,** 1935 (1967).

J. K. G. Watson, *J. Chem. Phys.* **98,** 5302 (1993).

M. J. Weida and D. J. Nesbitt, *J. Chem. Phys.* **100,** 6372 (1994).

M. J. Weida and C. S. Parmenter, *J. Phys. Chem. A* **101,** 9594 (1997).

M. J. Weida and C. S. Parmenter, *J. Chem. Phys.* **107,** 7138 (1997).

M. C. Yang, A. P. Salzberg, B. C. Chang, C. C. Carter, and T. A. Miller, *J. Chem. Phys.* **98,** 4301 (1993).

M. Yang, M. H. Alexander, C.-C. Chuang, R. W. Randall, and M. I. Lester, *J. Chem. Phys.* **103,** 905 (1995).

M.-C. Yang, C. C. Carter, and T. A. Miller, *J. Chem. Phys.* **107,** 3437 (1997).

M.-C. Yang, C. C. Carter, and T. A. Miller, *J. Chem. Phys.* **110,** 7305 (1999).

R. N. Zare, Z. Karny, and R. C. Estler, *J. Chem. Phys.* **69,** 5199 (1978).

R. N. Zare, *Ber. Bunsenges. Phys. Chem.* **86,** 422 (1982).

D. H. Zhang and J. C. Light, *J. Chem. Phys.* **104,** 4544 (1996).

D. H. Zhang and J. C. Light, *J. Chem. Soc., Faraday Trans.* **93,** 691 (1997).